Two-temperature Magnetohydrodynamic Simulations of Extra-Galactic Jets

大村, 匠

Thesis

Two-temperature Magnetohydrodynamic Simulations of
Extra-Galactic Jets

(系外ジェット伝搬の2温度磁気流体シミュレーション)

A Dissertation Submitted to Kyushu University
for the Degree of Doctor of Science

Takumi Ohmura

Theories of Particle Physics, Nuclear Physics and Astrophysics/Astronomy,
Department of Physics, Graduate School of Science, Kyushu University

March 2021

Abstract

Extragalactic jets launched from the supermassive black holes play a fundamental role in the evolution of galaxy clusters because the jet provides a large amount of energy to the intracluster (ICM) through shocks and turbulence. Because of weak Coulomb collisions under high-temperature and low-density plasma, the jets and surrounding ICM are expected to have different temperatures between protons and electrons, called 'two-temperature' plasma. In this thesis, we study the energy budgets of jets by a series of single fluid/two-temperature magnetohydrodynamics simulations that the jets interact with ICM.

In the first part, we presented the results for axisymmetric simulations of sub-relativistic jets that propagate and interact with the ICM. We examined the effect of the instantaneous electron heating on electron temperature distributions. The jet plasma crossing the shocks forms a hot, two-temperature plasma in which the proton temperature is higher than electron temperature. It was found that the protons stored in the cocoons maintain 10^{10-11} K longer than the normal active age, although 20 percents of the energy released by the shock wave are used to heat the electrons. Meanwhile, electrons are continuously heated by protons through Coulomb collisions.

Next, we simulated with three-dimensional models, including electron instantaneous heating at shock waves and turbulence. Strongly magnetized jet suffered from the development of non-axisymmetric, current-driven kink mode. Meanwhile, weakly magnetized jets were decelerated by the high-mixing ratio between the jet beam and cocoon gas, which were induced by Rayleigh-Taylor and Kelvin-Helmholtz instability. Also, jet magnetization affected the distribution of magnetic fields. The turbulent scale of the weakly magnetized jet was shorter than that of the strongly magnetized jets since the magnetic tension suppressed the turbulence motion. Through the three-dimensional studies, we found that there are two steps for the thermodynamics of electron and proton in the evolution of jet: First, most of the bulk kinetic energy of the jet is converted into thermal energy of proton through shocks, which are formed in the jet beam. Second, while magnetic fields are relatively strong, shocked-electrons stored in the cocoon evolve toward energy equipartition with magnetic energy through turbulent dissipation. As a result,

$U_{\rm p} \gg U_{\rm e} \sim U_{\rm mag}$ in the cocoon, where $U_{\rm p}$, $U_{\rm e}$, and $U_{\rm mag}$ are proton thermal energy, electron thermal energy, and magnetic energy, respectively.

In the final part, we calculated observational quarantines from our three-dimensional models. Radio power was obtained by solving liner-polarization synchrotron transport equations, and mechanical power was estimated in the same manner as X-ray observations. We compared our models and observations for the relationship between radio power and mechanical power. As a result, our models quantitatively explained the radiative inefficient jets, which are frequently observed at the cluster center, for the first time.

Acknowledgment

This work was generously supported by many people. I wish to express my gratitude, first, to my supervisor, Associate Prof. Mami Machida (NAOJ) for her continuous support and encouragement during this research. I thank her for her kind advises, useful discussion, and critical reading of this thesis. To my collaborators Prof. Kenji Nakamura (Kyusyu Sangyo Univ.), Dr. Yuki Kudoh (Kagoshima Univ.), Dr. Yuta Asahina (Tsukuba Univ.), Assistant Prof. Syuichi Matsukiyo (Kyushu Univ.), and Prof. Ryoji Matsumoto (Chiba Univ.), I would like to express my gratitude. Their advice and discussions enormously improved this research. I am grateful to Associate Prof. Yosuke Matsumoto (Chiba Univ.) who provided kindly support for the computational method. I would like to thank to the members of our research group, Prof. Kazuhiro Yamamoto, Prof. Emeritus Masaaki Hashimoto, Associate Prof. Sugumi Kanno, Dr. Akira Matsumura, Dr. Hiroki Matsui, Akira Dohi, Kazushige Ueda, Daisuke Miki, Koki Yamashita, and Tomoya Shichijo. In particular, special thanks to goes to Haruka Sakemi, Rikuto Omae, and Yuta Tashima. I would also like to Assistant Prof. Ken'ichiro Nakazato. I have learned many things from his inspired insight into physics. The numerical computations in this thesis have been carried out on Cray XC50 at Center for Computational Astrophysics, National Observatory of Japan, and the Fujitsu PRIMERGY CX600M1/CX1640M1 (Oakforest-PACS) at the Information Technology Center, The University of Tokyo, and Supercomputer System ITO at Research Institute for Information Technology, Kyushu University. Finally, I would like to express my deepest thanks to my parents and family for their continuous support and encouragement.

Contents

1 Introduction

Astrophysical jet, which is well-collimated supersonic flows, is a ubiquitous phenomenon observed in various layers of the universe. In particular, extra-galactic jet (hereafter 'jet') launched from the vicinity of a supermassive black hole ($M_{\rm SMBH} \sim 10^{6-10} M_{\odot}$; Kormendy & Richstone, 1995) emits over a wide range of energies from the radio to the γ-ray wavelength. The mechanical power of jets is estimated in the range of 10^{42-48} erg (Celotti & Fabian, 1993), and thus the jet heats intracluster and intragalactic medium (ICM/IGM) over the spatial scale of the host galaxy. Specifically, the jet interacts with the surrounding ICM, and the kinetic energy of the jet is transformed into thermal and turbulent energies of the ICM. A part of the jet kinetic energy is given to utilized for high energy non-thermal particles.

Jet plays a key role in the structure formation of the universe. Firstly, the jet is a promising candidate as ionization sources in the re-ionization epoch occurring at high redshift, $z \sim 6 - 8$ (Bosch-Ramon, 2018). Secondly, the jet-driven (kinetic) feedback process affects the evolution of galaxy clusters (Fabian, 2012). Because the radiation time scale without a heating source is much shorter than 10 Gyr in the central region of the cluster, the gas pressure in the central region rapidly decreases, and thus a cooling flow, which towards the cluster center, develops. Meanwhile, X-ray observations of many clusters show that the gas is not cooling to low temperatures, which was expected in the cooling flow model (Fabian, 1994). One of the plausible candidates for heating sources is jets from the host galaxy located in the cluster center. Therefore, the jet may prevent the cooling flow, fueling onto the central brightest cluster galaxy. This leads to suppress the growth of luminous galaxy. Finally, the astrophysical jet is an ideal particle acceleration site. The characteristic maximum energy of cosmic-ray particles with charge Ze is given by the Hillas energy (Hillas, 1984); $E = ZeuBR$, where u, B, and R are flow velocity, magnetic field strength, and source size, respectively. The affected area by the jet reaches $10 - 1000$ kpc, and the strong magnetic field is maintained at that region, Therefore,

the jet considered to be the leading candidate acceleration site for the ultra high energy cosmic-rays whose energy extends beyond 10^{20} eV (Matthews et al., 2020).

When the jet interacts with ICM, a low-density and high-temperature inflated bubble are formed. This bubble is called the 'radio lobe' because of seen in radio observation, which suggests that there are a large amount of magnetic and electron (and positron) energies. Meanwhile, X-ray images showing the gas emitting thermal bremsstrahlung radiation have represented the bubble as an X-ray cavity (e.g., Fabian et al., 2003; Bîrzan et al., 2020).

The combination between radio power and mechanical power provides us useful information of our understanding of the energetic and plasma composition in the lobes (Bîrzan et al., 2004, 2008). The energy of magnetic fields and relativistic electrons stored in the lobe can be estimated through synchrotron radio power $P_{\rm radio}$. X-ray cavity provides us a lower limit to the jet mechanical energy as cavity power $P_{\rm cavity}$ based on PdV works, i.e., the work done by the jets against the surrounding ICM. The ratio of radio power to cavity power, $P_{\rm radio}/P_{\rm cavity}$, (cavity-radio relation) is known as the radiative efficiency. The median ratio of $P_{\rm radio}$ to $P_{\rm cavity}$ for the radio lobes at the center of clusters is about 10^{-2}, i.e. most radio lobes are radiative inefficient. On the other hand, some sources such as Cygnus A are in radiative efficient lobes and hence there is a large scatter in this relationship. Therefore, measuring the energy budgets of jets has proven to be a very difficult problem.

To investigate the energy budgets of the jet-ICM system, several works based on magnetohydrodynamical (MHD) and hydrodynamical simulations have been conducted (e.g., Omma et al., 2004; Mendygral et al., 2012; Hardcastle & Krause, 2013, 2014; English et al., 2016; Bourne & Sijacki, 2017). Meanwhile, these works ignore the physics of 'two-temperature plasma'. Whenever the high-density and low-temperature plasma is efficiently Coulomb coupling, the electron and proton temperatures become equal instantly. Thus, the large-scale plasma dynamics can be treated as a single-temperature fluid. In contrary to this, when the plasma temperature is reached electron relativistic temperature ($kT_{\rm e} = m_{\rm e}c^2$) in high energy phenomena such as jets and hot accretion flow, this picture changes. The Coulomb coupling becomes inefficient, and the electrons and protons can have a different temperature, i.e. plasma has 'two-temperature' (Braginskii, 1965; Shapiro et al., 1976). Thus, we should solve the thermodynamics equations for both

electrons and protons to deal with two-temperature plasma. In particular, the fraction of heating into electrons should be treated as a realistic model, which is constructed from studies that investigate the microscopic properties of a collisionless plasma (Kawazura et al., 2019, 2020).

The physics of 'two-temperature plasma' would be important to investigate the energy budgets of the jet-ICM system. Actually, radio-emitting electrons are non-thermal components, which cannot be treated as fluids. Non-thermal electrons, however, are accelerated from thermal electrons via the micro-scale plasma process. Hence the non-thermal energy of electrons is naively proportional to the thermal one, the radio power depends on the electron temperature. Furthermore, treating two-temperature plasma could significantly affect the cavity-radio relation.

As we mentioned above, the nonequilibrium thermodynamics between electrons and protons is an interesting open question for the jet-ICM interaction. However, none of the numerical simulations have studied the thermal evolution of electrons in jets as a whole. We, therefore, investigate the energy budgets of jets by conducting a series of single fluid/two-temperature MHD simulations that the jets interact with ICM. In this thesis, we also need to mention that the words protons and ions are used interchangeably. The organization of this thesis as follows. Chapter 2 describes the observational feature and previous theoretical studies of the jet. In chapter 3, we review the two-temperature plasma from both theoretical and observational point of view. In chapter 4, we present the results of the axisymmetric simulations of sub-relativistic, inflated, magnetized jets that interact with homogeneous ICM. Chapter 5 present results of fully three-dimensional simulations including electron irreversible heating at shock waves and MHD turbulence. Also, we discuss radio signature and compare our models and observations for the relationship between radio power and mechanical power. A conclusion and future prospects are given in chapter 6. In Appendix A, we show the result of the one-dimensional test simulations, the shock-finding algorithm in our calculations, and the post-processing method for solving the synchrotron radiative transfer equations.

2 Review

In the 100 years since the first discovery of jets from active galactic nuclei (AGNs) (Curtis, 1918), various studies have been conducted to explore the physical properties of jets. Radio bright AGNs are currently understood that the energy released as electromagnetic radiation by the accretion process onto a supermassive black hole ($M_{\rm SMBH} \sim 10^{5-10} M_{\odot}$). A part of AGNs activities is the jet. It forms when the gravitational energy of supermassive black hole converts to the kinetic energy of jet by MHD process and/or Blandford-Znajeck process (Blandford & Znajek, 1977; Shibata & Uchida, 1986; Koide et al., 2002). Structures driven by AGN jets occur a very wide range in apparent source size (Hardcastle & Croston, 2020). For example, blazars are a compact and luminous time-variable source because a jet is oriented at a small angle to the line of site. On the other hand, kpc-scale radio structures are frequently observed in massive elliptical galaxies, called 'radio galaxies'. In this thesis, we focus on radio galaxies because the information of radio morphology provides us understandings of jet dynamics.

2.1 Radio galaxies and Fanaroff-Riley dichotomy

Typical radio structures as observed in radio galaxies are radio core, jet beam, lobe, and hotspot. Figure 2.1 shows the radio image of Cygnus A , which is one of the most popular and powerful radio galaxies (Carilli & Barthel, 1996). We can see typical radio structures in Fig. 2.1. The radio core spatially corresponds to the host galaxy observed at optical wavelengths, and usually radio component of the core is the flat spectrum (Kimball & Ivezić, 2008). The jet beam is a well-collimated flow from the radio core. Lobe is an extended diffuse radio structure, and it stores a large amount of energy transported along the beam. Hotspot (knot) is a compact and prominent spot formed at the jet terminate and/or in the beam flow. It is identified in-situ particle acceleration site i.e., shock or magnetic reconnection point.

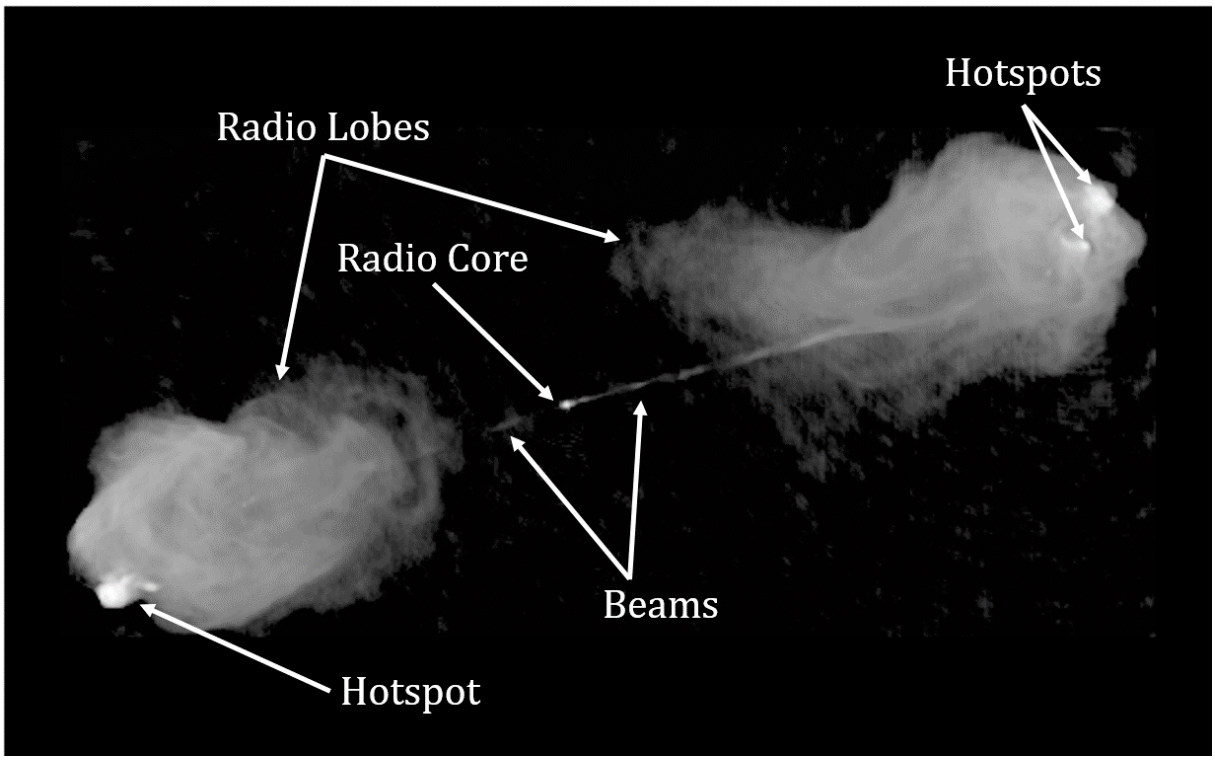

Fig. 2.1: The radio image of the image of Cygnus A (gray scale) at 5 GHz with 0.4" resolutions observed by the Very Large Array data (courtesy R.Perley).

X-ray images of radio galaxies have different features from those of radio images. Intracluster medium (ICM) radiates mainly by thermal free-free emission in the X-ray band. Surrounding ICM is, therefore, able to detect unlike the case of radio observation. Meanwhile, X-ray surface brightness where spatially corresponded to radio lobe is 20-40 percent bellow than that from its surrounding ICM. Thus, these regions call 'X-ray cavity'. We display the X-ray cavity system of MS 0735+7421 and schematic drawing of this system in Fig. 2.2. Supersonic jets drive shocks into the ICM, these shocks are sometimes called 'cocoon shock'. The compressed ICM by cocoon shock emit enhanced thermal X-ray emission, and therefore these emissions are detected in some radio galaxies. However, detailed analysis for Cygnus A, one of the most powerful jets, suggests a Mach number of cocoon shock is low, $\mathcal{M}$ = 1.18 - 1.66 (Snios et al., 2018). Other analyses done by Ineson et al. (2017) suggest a median value of Mach number for various cocoon shocks $\mathcal{M} \sim 2$. We can see that the hotspots and beams radiate in the X-ray band. These emissions are non-thermal component due to inverse Compton process (Harris & Grindlay, 1979; Hardcastle et al., 2004).

X-ray cavities have been qualitatively divided into two categories, namely radio-filled and radio-ghost cavities (Bîrzan et al., 2004). A radio-filled cavity is defined as the cavity is filled in 1400 MHz or higher frequency radio emission, and therefore it is stored in young electrons. In contrast, a radio-ghost cavity has lacks significant emission at 1400 MHz. Radio-ghost cavities are thought to have been formed by past AGN activities (McNamara et al., 2001).

Large-scale radio jets have exhibit different types of morphology. Fanaroff & Riley (1974) categorize radio galaxies based on their morphology into two class as follows:

- Fanaroff-Riley type I (FR I): Low brightness regions further from the galaxy than the high brightness regions.
- Fanaroff-Riley type II (FR II): High brightness regions further from the galaxy than the Low brightness regions.

FR I type jets have complex radio morphology. Some sources show large-scale plumes and wiggles like radio emissions (see Fig. 2.2), but other sources show bending feature. It is generally regarded that the jet is already subsonic flow during propagation, and it gradually dissipates its energy. On the other hand, FR II type jets show nearly straight

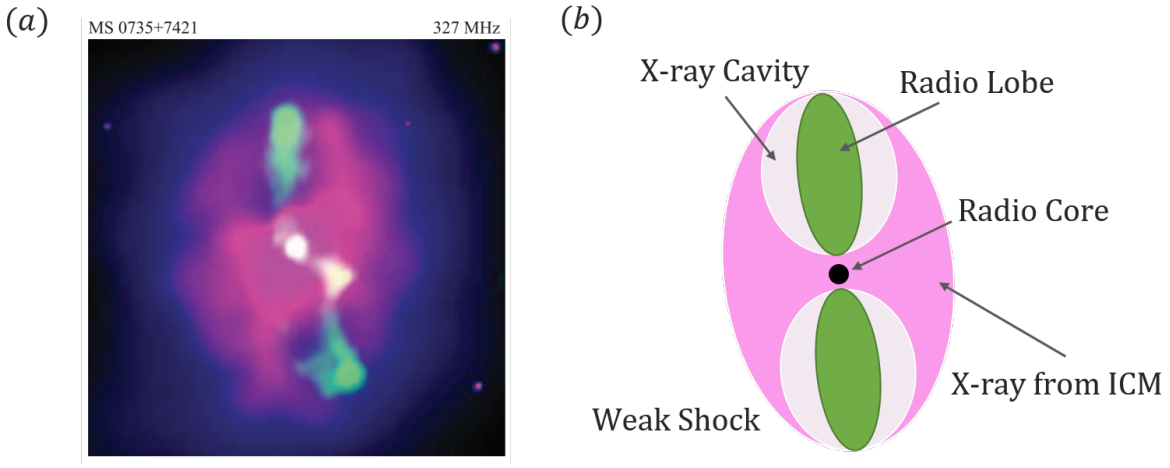

Fig. 2.2: (a) The radio at 327 MHz (green) overlays on the smoothed *Chandra* X-ray images of MS 0735+7421 (adopted from Laura Bîrzan's PhD thesis; Rafferty, 2007). (b) Schematic drawing of the X-ray cavity system.

beams and bright hotspots in radio lobes (see Fig. 2.1). FR II type jets are thought to have supersonic flows propagating to their termination.

FR distinction does not only link to jet dynamics but also link to radio luminosity. Fanaroff & Riley (1974) pointed out that most of radio luminosity for FR I type jets below 2×10^{32} erg s^{-1} Hz^{-1} Ω^{-1} at 178 MHz with a Hubble constant of 50 km Mpc^{-1} s^{-1}, and that FR II type jets were brighter than that. Recent radio survey of the Low-Frequency Array Two-Meter Sky Survey (LoTSS; Shimwell et al., 2017), however, indicated that there is a very large overlap in luminosity for FR I and FR II type jets (Mingo et al., 2019). Cross-matching method using LoTSS and the Sloan Digital Sky Survey (SDSS) cluster catalogs revealed that FR I type jets inhibit systematically richer environments than FR II type jets (Croston et al., 2019). Moreover, some sources showed that FR I type structure on one side of the source and FR II type structure on the other (e.g., Gopal-Krishna & Wiita, 2000). These results indicate that the origin of the FR dichotomy does not seem from properties of the central engine, but rather than the interplay of jet power and environment.

2.2 Radiation mechanism

2.2.1 Thermal and non-thermal particle distributions

In the context of astrophysics, radiations are divided into two types: a thermal one and a non-thermal one. Thermal and non-thermal radiation are deeply linked to electron distributions. Thus, we firstly describe commonly used functions for electron distributions.

The thermal and a power-law electron distributions are an important assumption for the radiation spectrum. In this section, the velocity and Lorentz factor denote $\boldsymbol{v}$ and $\Gamma = \{1 - (v/c)^2\}^{-1/2}$, respectively. The thermal distribution function of electrons is

$$N(v) = N_{\rm th} \left(\frac{m_{\rm e}}{2\pi k T_{\rm e}} \right)^{3/2} \exp\left(-\frac{m_{\rm e} v^2}{2 k T_{\rm e}} \right), \tag{2.1}$$

where $N_{\rm th}$, k, $T_{\rm e}$, and $m_{\rm e}$ are the electron number density of thermal component, the Boltzmann constant, electron temperature, and electron mass, respectively. When the electron temperature exceeds the rest mass energy ($kT_{\rm e} > m_{\rm e}c^2$), the thermal distribution is modified by the effects of special relativity. For a gas of relativistic electrons, the thermal distribution function is:

$$N(\Gamma) = N_{\rm th} \frac{\Gamma^2 \beta}{\theta_{\rm e} K_2(1/\theta_{\rm e})} \exp\left(-\frac{\Gamma}{\theta_{\rm e}} \right), \tag{2.2}$$

where the dimensionless electron temperature $\theta_{\rm e} \equiv kT_{\rm e}/m_{\rm e}c^2$, and $K_{\rm n}$ is the modified Bessel function of the n-th kind. The internal energy density of thermal electrons $u_{\rm th}$ is given by:

$$u_{\rm th} = a(\theta_{\rm e}) N_{\rm th} m_{\rm e} c^2 \theta_{\rm e} = \frac{p_{\rm e}}{\gamma_{\rm e} - 1} \tag{2.3}$$

where

$$a(\theta_{\rm e}) = \frac{1}{\theta_{\rm e}} \left[\frac{3K_3(1/\theta_{\rm e}) + K_1(1/\theta_{\rm e})}{4K_2(1/\theta_{\rm e})} \right], \tag{2.4}$$

and $p_{\rm e}$ is the pressure of electrons, and $\gamma_{\rm e}$ is the adiabatic index.

In contrast to the thermal distribution, the non-thermal one means that particles do not obey the thermal Maxwell distribution. A commonly non-thermal component is described as a power-law distribution function in energy space:

$$N(\Gamma) = \frac{N_{\rm NT}(p-1)}{{\Gamma_{\rm min}}^{1-p} - {\Gamma_{\rm max}}^{1-p}} \Gamma^{-p}, \quad \text{for} \ \ \Gamma_{\rm min} < \Gamma < \Gamma_{\rm max}, \tag{2.5}$$

and zero other wise. Here, $N_{\rm NT}$ is the number density of non-thermal component, $\Gamma_{\rm min,max}$ are the minimum and maximum Lorentz factor, and p is the spectral index, respectively. Therefore, the energy density of a non-thermal component is

$$u_{\rm NT} = \frac{N_{\rm NT}(p-1)}{{\Gamma_{\rm min}}^{1-p} - {\Gamma_{\rm max}}^{1-p}} m_{\rm e}c^2 \int_{\Gamma_{\rm min}}^{\Gamma_{\rm max}} \Gamma^{1-p} d\Gamma = N_{\rm NT} m_{\rm e}c^2 \frac{p-1}{p-2} \frac{\Gamma_{\rm max}^{2-p} - \Gamma_{\rm min}^{2-p}}{\Gamma_{\rm max}^{1-p} - \Gamma_{\rm min}^{1-p}}. \tag{2.6}$$

One of the motivations for adopting the power-law distributions is that observations directly imply the existence of power-law components. These power-law components are produced by particle acceleration in collisionless shocks and magnetic reconnections. To model for a more complex observational spectrum signature, several electron distributions, such as broken power-law distributions and kappa distributions, are proposed.

2.2.2 Synchrotron radiation

Charged particles moving through a magnetized plasma have a spiral motion. Since this motion is an accelerated motion, radiation is emitted as a consequence. In particular, in the case of relativistic particles, this radiation is so-called 'Synchrotron radiation' (for a detailed, see Rybicki & Lightman, 1986).

The synchrotron power P_ν from a single radiation electron is give by

$$P_\nu = \frac{\sqrt{3}e^3 B}{m_{\rm e}c^2} \sin\Psi F(x), \tag{2.7}$$

where Ψ is a pitch angle with respect to an ordered magnetic field, $x = \nu/\nu_c$ with the critical frequency of synchrotron radiation $\nu_c = \frac{3eB}{4\pi mc}\Gamma^2 \sin\Psi$, and $F(x) = x\int_x^\infty K_{5/3}(x')dx'$. Here, $K_{5/3}$ is the modified Bessel function of the second kind of order 5/3. The function of $F(x)$ has a peak value at $\nu = \nu_c$ and rapidly decreases when $\nu > \nu_c$. The energy loss rate for a electron due to synchrotron radiation is:

$$-\frac{du_{\rm e}}{dt} = \frac{3e}{4\pi {m^3}_{\rm e}c^5}(B\sin\Psi)^2 {u_{\rm e}}^2, \tag{2.8}$$

where $u_{\rm e}$ is the energy density of electron. The high-frequency synchrotron radiation is required for high-energy electrons. For example, the radio frequencies ($\sim$ GHz) in 10 μG magnetic field require $\Gamma \sim 10^4$ electrons.

Next, we consider the synchrotron radiation from non-thermal (power-law) distribution of electrons. Using the single-particle radiative power and an particle distribution

$N(\Gamma)$, we obtain the synchrotron emissivity j_ν as

$$j_\nu = \frac{1}{4\pi}\int_1^\infty N(\Gamma) P_\nu d\Gamma. \tag{2.9}$$

In the case of a power law model (Eq. (2.5)), this integration has been done and yields

$$j_\nu = N_{\rm NT}\left(\frac{e^2\nu_c}{c}\right)\frac{3^{p/2}(p-1)\sin\Psi}{2(p+1)(\Gamma^{1-p}{}_{\rm min}-\Gamma^{1-p}{}_{\rm max})}\Gamma_s\left(\frac{3p-1}{12}\right)\Gamma_s\left(\frac{3p+19}{12}\right)\left(\frac{\nu}{\nu_c\sin\Psi}\right)^{-(p-1)/2}, \tag{2.10}$$

where $\Gamma_s(x)$ is the gamma function of argument x. Note that this expression are obtained in the ultra-relativistic limits and are valid for $\nu \gg \nu_c$ Therefore, the emissivity have a power-law relation for frequency, i.e., $j_\nu \propto B^{1+\alpha}\nu^{-\nu}$, where $\alpha = (p-1)/2$ is the spectral index. Typical spectrum index for radio lobes is $\alpha \sim 0.5 - 0.8$, and thus power-law spectrum is corresponded to $p \sim 2 - 2.6$ (e.g., Hardcastle & Croston, 2020).

2.2.3 Bremsstrahlung radiation and line emission

The X-ray telescopes are sensitive to photons with energies spanning the range of 0.1-10 keV. In this range, the dominant radiation process is thermal Bremsstrahlung radiation and line emission. These emissions come from the ICM whose temperature and density are respectively around keV and 10^{-4} to 10^{-1} cm^{-3}.

Charged particles are accelerated by the Coulomb force and emit electromagnetic waves, which is called 'Bremsstrahlung' or 'free-free' radiation. Bremsstrahlung emissivity from the thermal electrons is given by

$$j_\nu^{ff} = 6.8\times10^{-38}Z^2 n_{\rm e} n_{\rm i}\sqrt{T_{\rm e}}\exp\left(-h\nu/kT_{\rm e}\right)g_{ff}(\nu, T_{\rm e}), \tag{2.11}$$

where g_{ff}, $n_{\rm e}$, $n_{\rm i}$ and Z are a velocity averaged Gaunt factor, the number density of electron and ion, and charge number, respectively. At a temperature higher than 3 keV, X-ray emission is dominant for thermal Bremsstrahlung radiation. On the other hand, at a temperature below 3 keV, the X-ray emission by recombination lines of iron, oxygen, silicon, and so on become dominant. In general, the total radiation power combining with Bremsstrahlung radiation and line emission per unit volume is described as $n^2\Lambda(T_{\rm e}, Z)$, where Λ is the cooling function depends on the electron temperature and gas composition Z.

The X-ray observation provides us two-important quantities of ICM; the volume integrating gas density and spectroscopic gas temperature. The emissivity of an optically thin intracluster gas almost depends on the number density in the *Chandra* broadband energy range. Thus, X-ray surface brightness is simply an integral of the number density squared along the line of sight, $S_{\rm X} \propto \int_{\rm LoS} n^2 dl$. On the other hand, the ICM temperature is measured by X-ray Spectroscopy. The most prominent spectral signature of temperature is the exponential cut-off of the spectrum at high energies (see Eq. (2.11)). For an optically thin plasma at temperatures around keV, this cut-off is seen in the X-ray range. Therefore, we can obtain the electron temperature to fit the X-ray spectrum, and it is a useful method for temperature measurement. Recent studies are conducting X-ray spectroscopic with a model fit that includes realistic physics, such as ionization equilibration (Gu et al., 2016).

2.3 Jets energetics

It is difficult to measure directly the physical quantities of the jet, namely density, temperature, magnetic field, plasma composition, and the outburst age. Thus, indirect measurements, based on some assumptions, have been done. In this section, we summarize the theory and observational result of indirect measurements using radio and X-ray observation.

2.3.1 Energy estimation from radio lobe

For optically thin emission, the total radio luminosity L are estimated as follows:

$$L = \int_{\nu_{\rm min}}^{\nu_{\rm max}} L_\nu d\nu = V \int_{u_{\rm e,min}}^{u_{\rm e,max}} \left(-\frac{du_{\rm e}}{dt} \right) N(u_{\rm e}) du_{\rm e}, \tag{2.12}$$

where L_ν and V are the radio luminosity at frequency ν and the volume of the source, respectively. In the case of synchrotron radiation, the emissivity is content in the information of the magnetic and electrons energy. However, these energies are not individual.

The usual way to estimate the magnetic field and the electrons energy is to minimize its total energy $U_{\rm tot}$ (Pacholczyk, 1970). The total energy of a synchrotron source is a sum of the magnetic energy ($U_{\rm B}$), the relativistic electron energy ($U_{\rm e}$), and non-radiating

proton energy ($U_{\rm p}$): $U_{\rm tot} = U_{\rm B} + U_{\rm e} + U_{\rm p}$. The idea of minimum energy estimation is based that non-thermal electrons and magnetic fields are strongly coupled and exchange energy until equilibrium is reached. Note that the minimum-energy and equipartition arguments give similar results and are often used without distinction in the context of radio astronomy. Here, equipartition argument is similar method to estimate the magnetic field that is to be equipartition with cosmic-ray particle energy ($U_{\rm e} + U_{\rm p} = U_{\rm mag}$).

To estimate the magnetic field using the minimum energy argument, we assume that the radio lobe filled radiating particles and magnetic fields homogeneously, and the completely random fields. The magnetic energy is calculated as:

$$U_{\rm mag} = \frac{B^2}{8\pi}\phi V, \tag{2.13}$$

where ϕ is the volume filling factor. The energy of synchrotron emitting electrons that obey the power-law distribution is calculated as Eq. (2.5). By eliminate $N_{\rm NT}$ and V to use Eq. (2.12), Eq. (2.8), Eq. (2.10) and Eq. (2.12), we obtain the electron energy as:

$$U_{\rm e} = B^{-3/2} L C_{12}(p, \nu_{\rm min}, \nu_{\rm max}). \tag{2.14}$$

Here, C_{12} is a function as defined by (Pacholczyk, 1970).

We assume that the proton energy $U_{\rm p}$ is proportional to the electron energy $U_{\rm e}$: $U_{\rm p} = kU_{\rm e}$. Thus, k is a parameter to determine the field strength. The total energy densities is obtained as a function of the magnetic field:

$$U_{\rm tot} = U_{\rm e} + U_{\rm p} + U_{\rm mag} = (1+k) L B^{-\frac{p+1}{2}} + \frac{B^2}{8\pi}\phi V, \tag{2.15}$$

From $dU_{\rm tot}/dB = 0$ we get minimum magnetic fields as follows:

$$B_{\rm min} = \left[\frac{6\pi C_{12}(1+k)L}{\phi V}\right]^{7/2}. \tag{2.16}$$

The minimum magnetic energy is 75% of the particles energy,

$$U_{\rm mag} = \frac{3}{4}\left(U_{\rm p} + U_{\rm e}\right) = \frac{3}{4}\left(1+k\right)U_{\rm e}. \tag{2.17}$$

Thus, minimum field strength is $\left\{1 - (3/4)^{2/7}\right\}$ times smaller than equipartition field strength.

Minimum energy conditions provide us individual magnetic fields, relativistic electron energy, and total energy interpreted as a lower limit. This method is easy to use because

only the radio intensity is required. It, therefore, is often used to estimate the strength of the magnetic field for a long time. Although the minimum energy condition is useful, we must assume the total energy of protons, i.e., determination of k. Because the protons do not radiate, it is difficult to determine the k value through observations. We usually used to assume $k \gg 1$ since k is determined by the particle acceleration mechanism, and protons usually have more energy than electrons (Beck & Krause, 2005). And of course, when the protons are absent in plasma (pair-plasma), k is zero.

In the context of radio jets, it was assumed that protons are absent ($k = 0$) or that protons and electrons are in the energy equipartition ($k = 1$). Under this assumptions, the equipartition magnetic field strength are several tens of μG in the radio lobes, and over a hundred μG in the hot spots (e.g., Carilli & Barthel, 1996; de Gasperin et al., 2012; Harwood et al., 2016). However, the plasma composition of jets is still under debate.

2.3.2 Energy estimation from X-ray cavity

One of the useful indirect methods for measurements of the jet mechanical power is using 'the PdV work' i.e., the work done by the jets against the surrounding ICM (e.g., Bîrzan et al., 2004; Cavagnolo et al., 2010; McNamara & Nulsen, 2007; Reynolds et al., 2001). Jets inflate the cavities (bubbles) observed in the thermal X-ray-emitting of their atmosphere. The total energy needed to form a cavity is the sum of the work pV and its thermal energy $U_{\rm th}$:

$$E = U_{\rm th} + pV = \frac{\gamma_{\rm gas}}{\gamma_{\rm gas} - 1} pV = \begin{cases} 2.5pV & (\gamma_{\rm gas} = 5/3) \\ 4pV & (\gamma_{\rm gas} = 4/3) \end{cases}, \tag{2.18}$$

where p, V, and $\gamma_{\rm gas}$ are the gas pressure, the size of X-ray cavity, and the specific heat ratio, respectively. Thanks to the characteristic of thermal X-ray, we are known the thermal electron density and temperature. Thus, the gas pressure is obtained by the ideal equation of state. Assuming the lobe and the atmosphere are in pressure equilibrium, the (lifetime-averaged) jet mechanical power estimated from the pdV-work is calculated by using the pressure of surrounding gas as follows: $P_{\rm cav} = E{t_{\rm age}}^{-1}$, where $t_{\rm age}$ it the time required to form the cavity. The estimation for $t_{\rm age}$ is detailed below. Note that the total energy E does not include energy transported into shocks, and therefore the cavity system provides only a lower limit to the total outburst energy.

Some assumptions are needed to estimate the ages of jets. Straight forward evaluation is a direct estimate using the current lobe expansion velocity. However, we need the assumption of constant velocity. It is, furthermore, difficult to measure the expansion velocity because this velocity of kpc-scale lobes already decelerates into non-relativistic velocity. Young (small) jets whose lobe size of $<$ kpc has sub-relativistic expansion velocity. The apparent expansion velocity, therefore, could be directly measured (e.g., Asada et al., 2009). In contrast to young (small) jets, the age of the cavity is estimated as a lobe traveling at approximately the sound speed of ICM. In other words, the age is estimated by the sound crossing time,

$$t_{\rm c} = R/c_{\rm s}, \tag{2.19}$$

where R is the projected distance from the center of the cavity to the radio core, $c_{\rm s} = \sqrt{\gamma kT/\mu m_{\rm p}}$ is the sound speed of ICM, where μ is the mean molecular weight. Also, Bîrzan et al. (2004) discussed the "buoyant rise" time $t_{\rm buoy}$, or the "refilling time" $t_{\rm r}$ to estimate the lobe age. The buoyant rise time and the refill time are taken for a lobe to rise buoyantly against with the cluster potential (see detailed in McNamara & Nulsen, 2007). These time scales appropriately are for the subsonic expansion. Generally, $t_{\rm c} < t_{\rm buoy} < t_{\rm r}$. Hardcastle & Croston (2020), meanwhile, pointed out that these three time scales are likely to be significant overestimates for typical powerful jets on the grounds of hydrodynamic simulations.

Alternative approach is to estimate ages from synchrotron radio spectrum $t_{\rm sync}$ (Myers & Spangler, 1985; Eilek & Arendt, 1996; Harwood et al., 2013). According to energy loss rates for synchrotron radiation in Eq. (2.8), electrons with higher energy lose their energy faster. If no particle acceleration event occurs in the lobe, the spectrum steepens at high frequencies i.e., spectrum shape becomes a broken power-law. Therefore, one can estimate the age of electrons stored in lobes by a spectrum fit. However, this estimation is also model-dependent. We have to consider the dynamical effect, such as particle acceleration in lobes and/or the mixing of old and young electrons populations. To overcome these problems, recently a more realistic model, which is combined with numerical hydrodynamic simulations, has been proposed by (Mahatma et al., 2020). Bîrzan et al. (2008) compared the two estimates of age, one is the synchrotron age and the other is the age estimated from sound speed. For the ghost cavities, two ages are roughly consistent,

$t_{\rm sync} \sim t_{\rm c}$. Meanwhile, the synchrotron age of radio-filled lobes is 5 to 10 times shorter than the age estimated by sound speed.

The projected cavity sizes are in the range 1 - 200 kpc, but typically within 40 kpc (Rafferty et al., 2006). Cavity ages estimated by sound speed are typically a several tens Myr, and also the work required to form the cavity is in $pV \sim 10^{55-61}$ erg. Thus, jet mechanical power, $P_{\rm cav} E t_{\rm age}^{-1}$, lie in the range 10^{41-46} erg s^{-1}.

2.3.3 Energy estimation from combination analysis with radio and X-ray data

Combined with radio and X-ray analysis, we can further enhance physical insight, such as plasma composition, for jets. A simple method with few assumptions is to examine the relationship between the mechanical power estimated from the X-ray cavity and radio luminosity. Bîrzan et al. (2008, 2004) found that the mechanical power estimated from X-ray cavity seem to have the correlation with the radio luminosity (sum of core an lobes), and that mechanical power increases with radio luminosity, $P_{\rm cav} \propto {P^{\beta}}_{\rm radio}$ where $0.35 \leq \beta \leq 0.70$. In Fig. 2.3, the median ratio of mechanical power to radio luminosity (radiative efficiency) is $P_{\rm cav}/P_{\rm Ladio} \sim 100$, but there is a large scatters in this plots. For example, Cygnus A is the most radiative efficient system, $P_{\rm cav}/P_{\rm Ladio} \sim 1$ in Fig. 2.3. There are several physical factors of these scatters such as electron cooling, estimation of ages, plasma composition, and variable activity of AGNs. However, the contribution of these factors to create this scatter is not understood.

Another way is that the lobe pressure compares with surrounding gas pressure. The particles in the lobe would support it against collapse, and therefore internal pressure should be equal to or greater than the gas pressure surrounding the lobe. We can estimate the equipartition (non-thermal) electron pressure, $p_{\rm eq}$, from radio observation (see details in Sect. 2.3.1). In the case of some powerful FR II jets, observations of non-thermal inverse-Compton X-ray emission and radio synchrotron emission from the lobes and hotspots measure individually the non-thermal electron pressure, $p_{\rm IC}$, without using minimum energy conditions (e.g., Harris & Grindlay, 1979; Hardcastle et al., 2004; Croston et al., 2005; Ineson et al., 2017). On the other hand, thermal X-ray emission measures the pressure surrounding lobe, $p_{\rm ICM}$.

Several studies have shown that the non-thermal equipartition electron pressures of lobes are an order of magnitude smaller than the pressure of surrounding gas , i.e., $p_{\rm eq}/p_{\rm ICM} \sim 0.1$ (Hardcastle & Worrall, 2000; De Young, 2006). Since the condition, $p_{\rm eq} > p_{\rm ICM}$, should be satisfied necessarily, these results indicate that contribution of gas pressure from non-radiating protons and thermal electrons dominate the total pressure. However, the pressures from inverse-Compton emission, $p_{\rm IC}$, are a factor 2.5 - 5 higher than the equipartition value (Ineson et al., 2017; Mahatma et al., 2020). Pressures of some lobes tend to be higher than the pressure of surrounding gas, $p_{\rm IC}/p_{\rm ICM} > 1$. Note that it does not rule out the existence of protons. In particular, a jet in a high-density cluster should have a large number of protons (Hardcastle & Croston, 2010). Finally, we mentioned that there is a trend that FR-I jets require the contribution of proton pressure to total pressure than FR-II jets to support their own lobes.

2.4 On the history of dynamical models

In this section, we summarize the findings of the theoretical studies about the dynamical models of the jet.

Analytical models

The standard picture of FR-II radio source has been proposed as 'the beam model' in the 1970s (Blandford & Rees, 1974; Scheuer, 1974). In this model, high-entropy gas is carried from a nucleus to the radio lobe by a relativistic beam, and the models qualitatively explain the lobe structure of typical FR-II, such as jet hotspot formed by shocks at beam termination and cocoons formed by the shocked jet plasma. Begelman & Cioffi (1989) constructed well-accepted models of FR-II type jets. They assumed that the kinetic-energy of jets is dominated and that the cocoon pressure is higher than that of the surrounding gas. Therefore, the cocoons expand with supersonic velocity. Firstly, the jet propagation velocity, $v_{\rm h}$, is determined by the momentum balance between the jet thrust, $\sim L_{\rm j}/v_{\rm j}$, and the ram pressure of surrounding medium, $\sim \rho_{\rm ICM} {v^2}_{\rm h} A_{\rm h}$:

$$v_{\rm h} = \left(\frac{L_{\rm j}}{\rho_{\rm ICM} {v_{\rm j}}^3 A_{\rm h}} \right)^{1/2} v_{\rm j}, \tag{2.20}$$

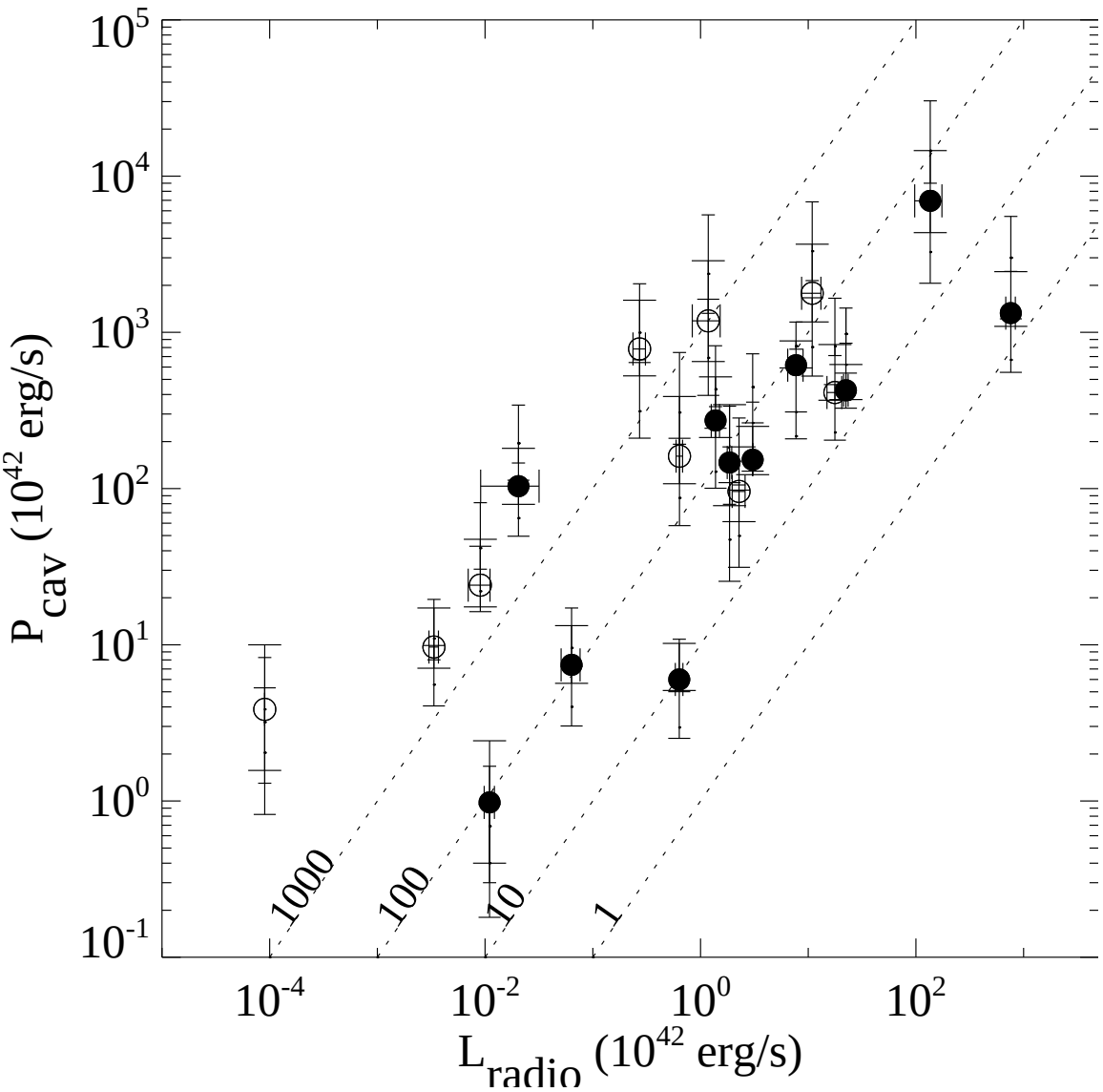

Fig. 2.3: Total radio luminosity $L_{\rm radio}$ (10 MHz-10 GHz) vs. jet power estimated from X-ray cavity system $P_{\rm cav} = 4pVt^{-1}{}_{\rm age}$ (adopted from Laura Bîrzan's PhD thesis Rafferty (2007) and McNamara & Nulsen (2007)). Open symbols show ghost cavities, and filled black symbols show radio-filled cavities (which including the intermediate cases). The symbols and wide error bars denote the values of the mechanical power calculated using the buoyancy timescale. The short and medium-width error bars denote upper and lower limits of the mechanical power calculated using the sound speed and refill timescales, respectively. The diagonal lines (dashed lines) represent ratios of constant mechanical power to radio luminosity.

where ρICM, $L_{\rm j}$, $v_{\rm j}$, and $\rho_{\rm ICM}$ are the density of ICM, the jet luminosity, the jet velocity, and the head area, respectively. For sideways expansion, the pressure inside the cocoon drives into surrounding medium at velocity $v_{\rm c}$. The equation of sideways expansion can be written by $p_{\rm c} \sim \rho_{\rm ICM} {v^2}_{\rm c}$, where $p_{\rm c}$ is the cocoon pressure. Assume that the jet kinetic energy is converted into thermal energy, and shocked plasma fills in the cocoon instantaneously. The order of cocoon pressure describe the total injected kinetic energy per the jet volume, $p_{\rm c} \sim 2 \int L_{\rm j} dt / V_{\rm c}$, where t and $V_{\rm c}$ are the source age and the volume of cocoon, respectively. Although both $L_{\rm j}$ and $v_{\rm h}$ are time dependent variables, this model approximate the constant values.These approximation leads to $V_{\rm c} \sim 2 A_{\rm c}(t) v_{\rm h} t \sim 2 {v^2}_{\rm c} v_{\rm h} t^3$, where $A_{\rm c}$ is the mean cross section of the cocoon (see Fig.1 in Begelman & Cioffi, 1989). Under this assumptions, we can obtain $v_{\rm c}$ as follows:

$$v_{\rm c} = \left(\frac{L_{\rm j}}{\rho_{\rm ICM} v_{\rm h}} \right)^{1/2} t^{-1/2}. \tag{2.21}$$

Thus, we can get the jet length and width from Eq. (2.20) and Eq. (2.21) when $\rho_{\rm ICM}$, $A_{\rm h}$, $v_{\rm j}$, $L_{\rm j}$, and t are known. $\rho_{\rm ICM}$ and $A_{\rm h}$ can be determined through observations, and commonly the jets assume relativistic, $v_{\rm j} = c$. Therefore, the model parameters are $v_{\rm j}$, $L_{\rm j}$, and t, Obeying the analytic models, we restrict the jet age and the jet kinetic energy from observed source size. By improving this model, recent analytical modeling tries to be more precise. For instance, the models implement the effect of the radial profile of ICM and time dependence of $v_{\rm h}$ and $A_{\rm h}$ (e.g., Kino & Kawakatu, 2005).

Meanwhile, there is no full agreement on the deceleration mechanism to model an FR-I type jet. But, some studies proposed ideas explaining the observed deceleration of FR-I type jets (Porth & Komissarov, 2015; Fujita et al., 2016; Massaglia et al., 2016; Perucho, 2020).

Hydrodynamical simulations

The hydrodynamic jet is Kelvin-Helmholtz (KH) unstable since they are typically supersonic and present a velocity shear. Therefore, many studies exist on numerical modeling of large-scale jet propagation to motivate a wide variety of purposes such as parameter studies for jets dynamics and investigate ICM heating by jet activity. Norman et al. (1982) performed a two-dimensional axisymmetric simulation of supersonic jets propagating into a homogeneous surrounding gas for the first time. They probed that powerful jets whose

density is lighter than surrounding gas formed the basic structure, which is suggested by the beam model. Furthermore, they found that internal shocks*) were present in the beam and that KH instabilities developed at the contact discontinuity between the cocoon gas and surrounding gas. While jets propagate at a large distance, back flow generates a large vortex at the head of the jet. These vortexes interact with beams and form the strong oblique shocks (Mizuta et al., 2004, 2010).

The large-scale morphology of jets depends on three parameters: The density ratio of jet to surrounding gas η, the beam internal Mach number $\mathcal{M}_{\rm jet}$, and the pressure ratio of jet to surrounding gas K. Since the jet becomes ballistic when $\eta > 1$, the extended cocoon is identified with the light jet ($\eta \ll 1$). The Mach number affect the development of HD instabilities, and high Mach number jets typically are stable (Bodo et al., 1994; Perucho et al., 2005). Conventionally, the condition that $K = 1$ is widely adopted.

A one-dimensional analysis provide us the propagation velocity $v_{\rm jet}$ for a high Mach number jet ($\mathcal{M}_{\rm jet} \sim 10$) as:

$$v_{\rm jet} = \frac{\sqrt{A\eta}}{\sqrt{A\eta}+1} v_{\rm beam}, \tag{2.22}$$

where A is the cross section ratio between beam and jet head, and $v_{\rm beam}$ is the injection velocity. When the jet propagates at a short distance, the velocity estimated of Eq. (2.22) is in good agreement with axisymmetric simulations. However, the propagation velocity is no longer constant, and the jet is decelerating gradually (e.g., Krause, 2003; Mizuta et al., 2004). One of the deceleration mechanism is increasing the jet head size due to the generation of a large vortex. Meanwhile, some three-dimensional simulations show that jet propagation can be faster than axisymmetric models because the tip of the jet becomes a drill-like shape i.e., the head size is decreasing (Massaglia et al., 2016; Perucho et al., 2019).

The supersonic beam flow undergoes expansion and recollimation. The radial force arising from these motion induce the development of Rayleight-Taylor (RT) instability (Matsumoto & Masada, 2013; Matsumoto et al., 2017; Toma et al., 2017; Matsumoto & Masada, 2019). Matsumoto & Masada (2013) introduce the onset condition of RT model as $\rho_{\rm jet} > \rho_{\rm cocoon}$ for the non-relativistic jet, where $\rho_{\rm jet}$ and $\rho_{\rm cocoon}$ are the gas density of jet and cocoon, respectively. It is expected that this onset condition is satisfied when

*)sometimes called 'oblique shocks', and 'recollimation shocks'.

the light supersonic jet propagates into the surrounding heavy ICM. A small-scale non-axisymmetric mode is a growth in RT instability and the gas mixing between the beam and the cocoon by RT mode cause jet deceleration.

Magnetohydrodynamical simulations

In the case of MHD jets, the flow dynamics become more complex than HD jets because of the Lorentz force. The outstanding effect for jet dynamics is the development of the current-driven kink mode, which leads to a displacement of the mass centre in the jet cross-section. Linear stability analysis has shown that cylindrical MHD jets are generically unstable for the kink mode (Appl et al., 2000), and therefore several works of 3D MHD simulations have been conducted to deal with the non-linear evolution of jets (e.g., Mignone et al., 2013; Tchekhovskoy & Bromberg, 2016; Mukherjee et al., 2020). The kink mode evolves on a time-scale at that Alfvén waves travel around the unstable region, called the Alfvén crossing time. The Alfvén crossing time for a cylindrical jet is given by (Moll et al., 2008)

$$\tau_{\rm kink} = \frac{2\pi R}{v_{{\rm A},\phi} - 2\pi v_r}, \tag{2.23}$$

where, $v_{{\rm A},\phi}$ is the azimuthal Alfvén speed, $v_{\rm R}$ is the expansion velocity, and R is the jet radius, respectively. The magnetic field, in some cases, plays a significant role for jet stabilization and collimation since the magnetic tension suppresses the development of RT and KH instability (Mukherjee et al., 2020; Komissarov et al., 2019). Finally, We mention that the magnetic pinching sometimes disrupts the jet (Massaglia et al., 2019). Therefore, the magnetic field cannot ignore for the dynamical modeling of jets.

3 Two-temperature plasma

In this chapter, we summarize the two-temperature plasma from both an observational and theoretical point of view. We then derive the single-fluid/two-temperature MHD equations and discuss the applicability of the two-temperature approximation for the jet.

3.1 Fundamental physics

Astrophysical plasma such as jets, galaxy clusters, and supernova remnants (SNRs) are almost collisionless; i.e., the collisional mean free path is longer than their size. In the absence of collisions that would enforce thermal equilibrium, electrons and ions do not always have the same temperature. Therefore, the time scale of the Coulomb coupling is the most important indicator for discussing two-temperature plasma.

3.1.1 Coulomb coupling

The rate of energy transfer, $q^{\rm ie}$, from ions to electrons per unit volume through Coulomb collisions is determined as follows (Stepney & Guilbert, 1983; Dermer et al., 1991);

$$q^{\rm ie} = \begin{cases} \frac{3}{2}\frac{m_{\rm e}}{m_{\rm i}} n^2 \sigma_{\rm T} c \frac{\ln\Lambda (kT_{\rm i} - kT_{\rm e})}{K_2(1/\theta_{\rm e}) K_2(1/\theta_{\rm i})} \left[\frac{2(\theta_{\rm e}+\theta_{\rm i})^2+1}{\theta_{\rm i}+\theta_{\rm e}} K_1\left(\frac{1}{\theta_{\rm m}}\right) + 2K_0\left(\frac{1}{\theta_{\rm m}}\right)\right] & (\theta_{\rm i} > 0.2) \\ \frac{3}{2}\frac{m_{\rm e}}{m_{\rm i}} n^2 \sigma_{\rm T} c \ln\Lambda (kT_{\rm i} - kT_{\rm e}) \frac{\sqrt{\frac{2}{\pi}}+\sqrt{\theta_{\rm i}+\theta_{\rm e}}}{(\theta_{\rm i}+\theta_{\rm e})^{3/2}} & (\theta_{\rm i} < 0.2), \end{cases} \tag{3.1}$$

where $\theta_{\rm m} = \theta_{\rm i}\theta_{\rm e}/(\theta_{\rm i}+\theta_{\rm e})$. The quantities

$$\theta_{\rm i} \equiv \frac{k_{\rm B}T_{\rm i}}{m_{\rm i}c^2} \quad \text{and} \quad \theta_{\rm e} \equiv \frac{k_{\rm B}T_{\rm e}}{m_{\rm e}c^2} \tag{3.2}$$

are the dimensionless ion and electron temperatures, respectively. The parameters $\sigma_{\rm T}$, and c are the Thomson scattering cross section, and the speed of light, respectively. $\ln\Lambda$

is the Coulomb logarithm and approximated to be

$$\ln \Lambda \approx 37.8 + \ln\left(\frac{T_{\rm gas}}{10^8\ {\rm K}}\right) - 0.5 \ln\left(\frac{n}{10^{-3}\ {\rm cm}^{-3}}\right) \tag{3.3}$$

for $T > 4 \times 10^5$ K (Spitzer, 1962). Functions K_0, K_1, and K_2 are respectively modified Bessel functions of the second kind of order 0, 1, and 2.

3.1.2 Time scales

There are three important time scales to consider in two-temperature plasma: The time required to reach a Maxwell distribution of electron temperature, $t_{\rm ee}$, and ion temperature, $t_{\rm ii}$. The relaxation tame scales for electron and ion are given by Spitzer (1962) as follows:

$$t_{\rm ii} = \frac{\sqrt{2\pi}}{n_{\rm i}\sigma_{\rm T} c \ln\Lambda}\left(\frac{m_{\rm i}}{m_{\rm e}}\right)^2 \theta_{\rm i}^{3/2}, \tag{3.4}$$

$$t_{\rm ee} = \frac{\sqrt{2\pi}}{2n_{\rm e}\sigma_{\rm T} c \ln\Lambda}{\theta_{\rm e}}^{3/2}. \tag{3.5}$$

The time required to electrons and ions to reach thermal equilibrium, $t_{\rm ei}$, is :

$$t_{\rm ei} = \frac{\sqrt{2\pi}}{2n_{\rm e}\sigma_{\rm T} c \ln\Lambda}\frac{m_{\rm i}}{m_{\rm e}}\left(\theta_{\rm e} + \theta_{\rm i}\right)^{3/2}. \tag{3.6}$$

These time scales indicate that the electrons are thermalized by self-collisions first, then the ions, and finally electrons and ions reach thermal equilibrium, i.e., $t_{\rm ee} < t_{\rm ii} \ll t_{\rm ei}$. Also, the tenuous and hot plasma takes longer to reach thermal equilibrium for electrons and ions.

3.2 Observational evidence of two-temperature plasma

It is difficult to clue evidence of two-temperature plasma in astrophysical phenomena because ions do not emit radiation enough to observe. Thus, observational evidences of two-temperature plasma have been obtained for only a few objects, such as the bow shocks of the Earth and Saturn (Schwartz et al., 1988; Masters et al., 2011), the forward shock of SNRs (Ghavamian et al., 2013), and galaxy cluster shocks (Russell et al., 2012).

Note that the three shocks listed above are formed under different plasma conditions (see Tab. 3.1). Therefore, these observational results cannot be simply compared.

Figure 3.1 shows that the temperature ratio between electrons and ions at post-shock gas is plotted versus magneto-sonic Mach number measured at the bowshocks of the Earth and the Saturn and the forward shocks of SNRs. In the case of celestial bowshocks, the ISEE spacecraft observation could directly measure ion and electron temperature at the post-shock plasma. Electrons were heated much less than protons, but electron temperatures were slightly higher than adiabatic compression temperature. The results indicated that the ratio of the electron temperature to ion temperature $T_{\rm e}/T_{\rm i}$ is unity when $\mathcal{M} < 2$, where $\mathcal{M}$ is the magneto-sonic Mach number, and $T_{\rm e}/T_{\rm i} \propto \mathcal{M}^{-2}$ otherwise. On the other hand, electron and ion temperatures were measured at the post-shock gas of SNR shocks by optical spectroscopy. The spectroscopic analysis of 5 SNRs sample by Ghavamian et al. (2007) has shown that $T_{\rm e}/T_{\rm i}$ is close to unity when the shock velocity below 400 km s^{-1}, and $T_{\rm e}/T_{\rm i}$ declines sharply proportional to the inverse square of the shock velocity above 400 km s^{-1}. Thus, two different shocks of celestial objects and SNRs have a similar relation, $T_{\rm e}/T_{\rm i} \propto \mathcal{M}^{-2} (\propto v_{\rm shock}^2)$, where $v_{\rm shock}$ is the shock velocity.

There is indirect evidence of two-temperature plasma in X-ray observation of the bow shock of merging galaxy clusters. Russell et al. (2012) showed that for the galaxy cluster Abell 2146, the post-shock electron temperature is lower than the ion temperature, as predicted from Rankine–Hugoniot jump conditions. Meanwhile, Markevitch (2006) has shown that post-shock electrons are in electron-proton equilibration at the shock in cluster 1E 0657-56, but it still remains some uncertainties. This measurement suggests that we have to consider some efficient ways to energy exchange between electrons and ions.

Finally, we mention the shock in the system of jet-ICM. As we mentioned in Chap. 2, we cannot measure the temperature of jets. Meanwhile, the cocoon shock propagating into the ICM is observed by X-ray observation, and we can measure the electron temperature of the shock. Measured Mach number of the cocoon shock of Cygnus A from 20 Msec of *Chandra* observations is a range of 1.18-1.66 (Snios et al., 2018). The post-shock electron temperature should be higher than the pre-shock electron temperature. However, the projected temperature in the pre-shock region is lower than that in the post-shock region. This result implies that electrons are cooler than protons in the post-shock region, i.e., 'two-temperature plasma', but further verification is needed to make this clear.

Table 3.1: Typical properties of various astrophysical shocks

Objects	Celestial objects	SNR*	Cluster shock	Cocoon shock
Density [cm^{-3}]	~ 10	1	$10^{-2} - 10^{-4}$	$10^{-2} - 10^{-3}$
Temperature [K]	$10^4 - 10^5$	10^4	$10^7 - 10^8$	$10^7 - 10^8$
Plasma-β	1 - 5	1 - 5	> 100	> 100
Shock velocity [km s^{-1}]	300 - 900	400 - 4000	~ 2000	$\sim$2000
Mach number	≤ 10	$\gg 100$	1.5 - 5	~ 2
Shock length	$\sim$ AU	$\sim$ pc	$\sim$ 500 - 1000 kpc	$\sim$ 10-100 kpc

* Assuming a $B = 3$ μG for interstellar medium.

3.3 Theory of two-temperature plasma from kinetic to MHD scales

The plasma heating and its energy partition mechanism in collisionless plasma have been investigated by numerical simulations such as the particle-in-cell (PIC) method and gyrokinetic model. These simulations are interested in the physical range of plasma kinetic-scale, and therefore it is difficult to connect their result to observations directly. Overcome this problem, several studies apply the two-temperature model to (M)HD scales. In this section, we first report the electron and proton heating mechanism in various dissipation processes, and then summarize results of the context of two-temperature (M)HD simulation.

3.3.1 Dissipation process in collisionless plasma

In this subsection, we focus on the dissipative processes that are considered to be dominant in jets: shock waves, MHD turbulence, and magnetic reconnection. Although there are various theoretical studies, little is know about the exact mechanism of plasma heating in each dissipation process.

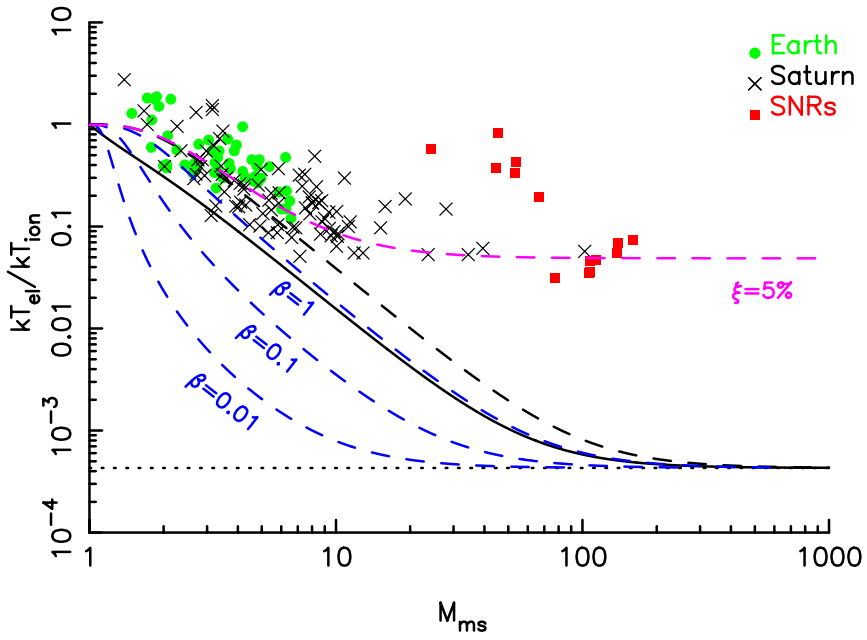

Fig. 3.1: The temperature ratio between electrons and ions at post-shock gas is plotted versus magneto-sonic Mach number. The data points show data measured behind the Earth bowshock (Green cicle Schwartz et al., 1988), Saturn's bowshock (X-shaped symbols , Masters et al., 2011) and SNRs (red squares, van Adelsberg et al., 2008). Here, van Adelsberg et al. (2008) assumed that Alfvén velocity is 9 km s^{-1}, and that the sound speed is 11 km s^{-1}. Electron-proton temperature ratio calculated for minimum electron temperature (solid black line), for the case of electron adiabatic heating (dashed black line), and for magnetized plasma with plasma $\beta =$ 0.01, 0.1, 1 (blue dashed line). Magenta dashed line shows that ion–electron temperature ratio assuming adiabatic heating of electrons and heat exchange between electrons and ions using the exchange factor $\zeta = 5$ %, which is defined as the fraction of the enthalpy-flux difference between ions and electrons.

Astrophysical shock

Plasma bulk kinetic energy is converted to heating energy at a shock. Since plasma momentum represent by ions, the Rankine-Hugoniot conditions for a strong shock imply that postshock temperature ratio between electron and ion is calculated as $(T_{\rm e}/T_{\rm i}) = (m_{\rm e}/m_{\rm i})$. And then, electrons and ions exchange energy towards the same temperature via Coulomb collisions. This physical picture, however, does not apply to the collisionless shocks. Energy partition between electrons and ions are wholly dependent on the development of plasma instability occurring at the shock transition layer.

Vink et al. (2015) investigated electron heating at shock by phenomenological approach. They derived the equation for the post-shock ion-electron temperature ratio assuming adiabatic heating of electrons and heat exchange between electrons and ions using the exchange factor ζ, which is defined as the fraction of the enthalpy-flux difference between ions and electrons whereas $\zeta = 50$ % corresponds to equal ion and electron temperature. To explains the observational results, ζ should be at least higher than 5 % (see magenta line in Fig. 3.1). More details about electron heating at astrophysical shocks will be given in Sect. 4.5.1.

MHD turbulence

Supersonic turbulence is developed by hydrodynamic instabilities in the jet. Turbulence is often described as a process in which large-scale eddies cascade to smaller-scale eddies, and then finally the kinetic and magnetic energy of eddies is converted into thermal energy of electrons and ions via microscale dissipation process.

This plasma heating process is well studied in the context of the hot accretion flow. Sharma et al. (2007) have been investigated electron heating in hot accretion flows by local sharing box simulations of the non-linear evolution of the turbulence driven by magnetorotational instability (Balbus & Hawley, 1998), incorporating the pressure anisotropy. They found that the dissipation energy heats the electrons as $Q_{\rm i}/Q_{\rm e} \propto \sqrt{T_{\rm i}/T_{\rm e}}$, where $Q_{\rm i,e}$ are the dissipation energy that heats electrons and ions, respectively. Note that this calculation is in the range that the thermal pressure is larger than the magnetic pressure.

Recently, energy partition between electrons and ions in collisionless turbulence is investigated by non-linear hybrid gyrokinetic simulations (Howes, 2010; Kawazura et al.,

2019, 2020). We display their results in the case of purely Alfvénic turbulence in Fig. 3.2. Their simulations covered in wide parameter range for ion plasma $\beta_{\rm i}(\equiv 8\pi nkT_{\rm i}/B^2)$ and temperature ratio between electron and ion. They propose a simple fitting formula to apply two-temperature MHD simulation for $Q_{\rm i}/Q_{\rm e}$:

$$\frac{Q_{\rm i}}{Q_{\rm e}} = \frac{35}{1+(\beta_{\rm i}/15)^{-1.4}{\rm e}^{-0.1T_{\rm e}/T_{\rm i}}} + \frac{P_{\rm compr}}{P_{\rm AW}}, \tag{3.7}$$

where $P_{\rm compr}$ and $P_{\rm AW}$ are the compressive and the Alfvénic energy injection. The compressive driving power is converted into ion thermal energy. Therfore, $Q_{\rm i}/Q_{\rm e}$ is an increasing function of $P_{\rm compr}/P_{\rm AW}$. In particular, $Q_{\rm i}/Q_{\rm e} \sim P_{\rm compr}/P_{\rm AW}$ for $P_{\rm compr} > P_{\rm AW}$. Meanwhile, in the purely Alfvénic turbulence ($P_{\rm compr}/P_{\rm AW} \to 0$), electrons are heated more than ions at $\beta_{\rm i} < 1$ (see the left panel of Fig. 3.2). The ion thermal velocity is much smaller than the Alfvén velocity, and ions cannot interact with Alfvénic waves. Thus, injection energy is not diverted into ions thermal energy.

Other approach to investigate electron heating in collisionless turbulence is PIC simulations (Zhdankin et al., 2019, 2020). Their results also support that electrons and ions evolve toward the two-temperature state in which ions are hotter than electrons. This result is consistent with the previous gyrokinetic model. However, we caution that their simulations are difficult to deal with low-beta plasma.

Magnetic reconnection

In high-energy astrophysical phenomena, magnetic reconnection can be the important energy conversion process. During the magnetic reconnection, the magnetic energy is converted into the heating energy and the bulk kinetic energy. Electron heating via magnetic reconnection are investigated by using PIC simulations (e.g., Rowan et al., 2017; Hoshino, 2018; Rowan et al., 2019). Hoshino (2018) found that there are two stages for plasma heating during two-dimensional antiparallel magnetic reconnection in the non-relativistic plasma regime: one is an adiabatic heating stage in which the plasma entropy along the plasma flow is conserved. Another is a non-adiabatic heating stage in which the energy gain process of electrons and ions is likely ohmic diffusion. They also found that the increment of ion and electron temperature ratio is proportional to $(m_{\rm i}/m_{\rm e})^{1/4}$, i.e, ions are more heated than electrons during reconnection. Meanwhile, electrons receive heating energy more than ions for a strong guide field, which is perpendicular to the reversing

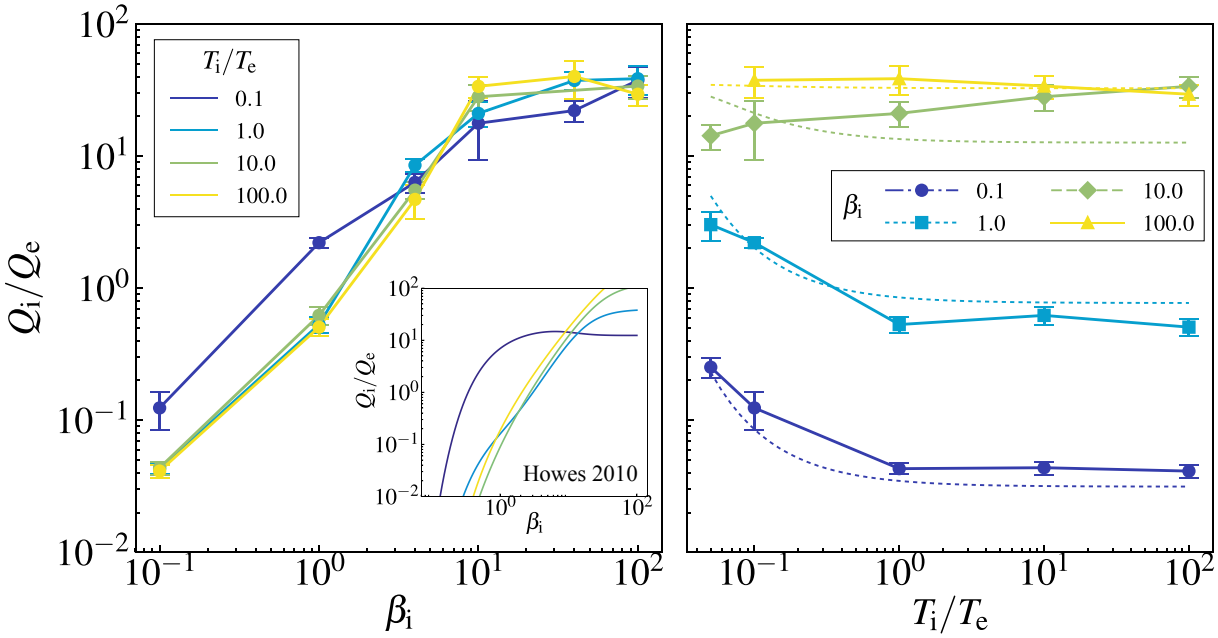

Fig. 3.2: The heating ratio of ion to electron Q_i/Q_e is plotted versus ion plasma-β_i (left) and temperature ratio of ion to electron T_i/T_e from nonlinear hybrid gyrokinetic simulations in the case of $P_{\rm compr}/P_{\rm AW} = 0$. The dotted lines in the right panel show the fitting formula Eq. (3.7) at $P_{\rm compr}/P_{\rm AW} = 0$. The inset figure in the left panel is same plot of the left panel, but the model proposed in Howes (2010). (credit: Kawazura et al., 2019)

field in the trans-relativistic plasma regime (Rowan et al., 2019).

3.3.2 Application for two-temperature MHD model

Two-temperature MHD simulations have been carried out for the context of galaxy clusters and hot accretion flow around compact objects. Therefore, we summarize these works in this subsection. Also, we report the result of our previous work that two-temperature MHD simulations for the jet from the stellar black hole.

Galaxy cluster

The outskirts of galaxy cluster may have a two-temperature structure because the ions are expected to be heated by shocks (e.g., Takizawa, 1998). Then, the thermal equilibration in merging clusters has been studied by hydrodynamic N-body/smoothed particle hydrodynamics(SPH) simulations (e.g., Takizawa, 1999; Akahori & Yoshikawa, 2008, 2010, 2012). Since the Coulomb coupling is inefficient, the electron temperature is significantly lower than that the mean temperature of ICM at shock layers. In addition, Yoshida et al. (2005) have investigated the two-temperature structure of the intergalactic medium using a large cosmological N-body/SPH simulation. They also found that the electron temperature in post-shock regions remains smaller than the ion temperature. Komarov et al. (2020) have been performed two-temperature MHD simulations including thermal conduction for a weak shock observed in the core of a galaxy cluster. They found that electrons and ions have a different temperature at post-shock regions, but that the electron temperature of the two-temperature model behaves the same as the gas temperature in the one-temperature model including thermal conduction. However, these numerical simulations did not implement the effect of instantaneous electron heating at shocks.

Hot accretion flow

Jets of low-luminosity AGNs are launched from radiatively inefficient accretion flows. In such hot accretion flows, the collision time scale is much longer than the accretion time scale, and the electron temperature is thus lower than the ion temperature (e.g., Shapiro et al., 1976; Narayan & Yi, 1995; Nakamura et al., 1996). Manmoto et al. (1997)

calculated the global structure of an advection-dominated accretion flow constituting two-temperature plasma and obtained a model that explains the spectrum of Sagittarius A*, where the temperature profile of the electron is the vital factor. Ressler et al. (2015) reported the results of simulations of a two-temperature accretion disk carried out by combining the electron energy equation with ideal general-relativistic MHD equations. The two-temperature MHD approach has been applied in recent simulations of the jet formation in M87 (Ryan et al., 2018; Chael et al., 2019).

A key factor of the two-temperature MHD is the fraction of the electron heating to the dissipative energy. The ratio of electron heating to ion heating depends on the microscopic properties of the collisionless plasma on a scale much smaller than the cell size in the MHD simulation. Previous studies assumed two different physical mechanisms in estimating the fraction of electron heating (Chael et al., 2018, 2019). The first mechanism is MHD turbulent heating in collisionless plasma while the second is heating by magnetic reconnection. Results of gyrokinetic simulations for turbulent heating indicate that the heating rate strongly depends on the ratio of the ion pressure to the magnetic pressure $\beta_{\rm i}$ (Howes, 2010). Recall that electrons are heated more than ions at $\beta_{\rm i} < 1$ in this model. In the disk region for the hot accretion flow, the averaged plasma $\beta_{\rm i}$ is higher than unity, and hence the ion temperature exceeds electron temperature. Meanwhile, the electron temperature becomes one order of magnitude higher than the ion temperature in the funnel region of the jets where $\beta_{\rm i} < 1$.

When the electron is heated by fast magnetic reconnection, the fraction of the electron heating does not exceed 0.5. This means that the electron always obtains less dissipated energy than the ion. This tendency has been observed in PIC simulations of fast magnetic reconnection (Rowan et al., 2017). The electron temperature is therefore equal to or less than the ion temperature in the funnel region of the jets. These simulation results indicate the existence of a two-temperature plasma in jets. However, it is not obvious whether electrons and ions have different temperatures during the propagation of large-scale jets.

Jets from X-ray binary

In our previous work (Ohmura et al., 2019), we investigated the propagation of sub-relativistic jets in X-ray binaries by conducting two-temperature MHD simulations. Figure 3.3 shows the distribution of the electron temperature and ion temperature. We

showed that the ion temperature downstream of the jet terminal shock (hot spot) becomes 10 times the electron temperature because ions are heated by energy dissipation at shocks. Meanwhile, electrons are not heated at the shock front because the instantaneous electron heating at shock fronts was ignored. In the cocoon, electrons are heated by Coulomb collisions with ions. Around the interface between the cocoon and the ambient medium, the electron temperature decreases owing to gas mixing between the hot cocoon plasma and the low-temperature ambient plasma via Kelvin–Helmholtz (KH) instability.

3.4 Single-fluid/two-temperature equations

Considering large-scale fluid dynamics, it is reasonable to assume that the ions represent fluid-momentum because electrons inertia can be neglected. However, it is necessary to follow the energy content of both electrons and ions. We also assume fully ionized hydrogen plasma and charge neutrality $n = n_{\rm i} = n_{\rm e}$, where $n_{\rm i}$ and $n_{\rm e}$ are respectively the ion number density and electron number density. Under this assumption, the single-fluid two-temperature MHD equations are written by (e.g., Braginskii, 1965; Oda et al., 2010)

$$\frac{\partial n}{\partial t} + \nabla \cdot (n\boldsymbol{v}) = 0, \tag{3.8}$$

$$m_{\rm i} n \left[\frac{\partial \boldsymbol{v}}{\partial t} + (\boldsymbol{v}\cdot\nabla)\boldsymbol{v}\right] = -\nabla p_{\rm gas} - \nabla\left(\frac{B^2}{8\pi}\right) + \frac{1}{4\pi}(\boldsymbol{B}\cdot\nabla)\boldsymbol{B}, \tag{3.9}$$

$$\frac{\partial \boldsymbol{B}}{\partial t} = \nabla \times (\boldsymbol{v}\times\boldsymbol{B}), \tag{3.10}$$

$$\frac{\partial \epsilon_{\rm i}}{\partial t} + \nabla\cdot[(\epsilon_{\rm i}+p_{\rm i})\boldsymbol{v}] - (\boldsymbol{v}\cdot\nabla)p_{\rm i} = -q^{\rm ie} + (1-f_{\rm e})q^{\rm heat}, \tag{3.11}$$

$$\frac{\partial \epsilon_{\rm e}}{\partial t} + \nabla\cdot[(\epsilon_{\rm e}+p_{\rm e})\boldsymbol{v}] - (\boldsymbol{v}\cdot\nabla)p_{\rm e} = +q^{\rm ie} + f_{\rm e}q^{\rm heat} - q^{\rm rad}, \tag{3.12}$$

where $\boldsymbol{v}$ is the velocity, $\boldsymbol{B}$ is the magnetic field, $m_{\rm i}$ is the ion mass, $p_{\rm gas} = p_{\rm i} + p_{\rm e}$ is the gas pressure, and $p_{\rm i}$ and $p_{\rm e}$ are respectively the ion and electron gas pressures. We assume

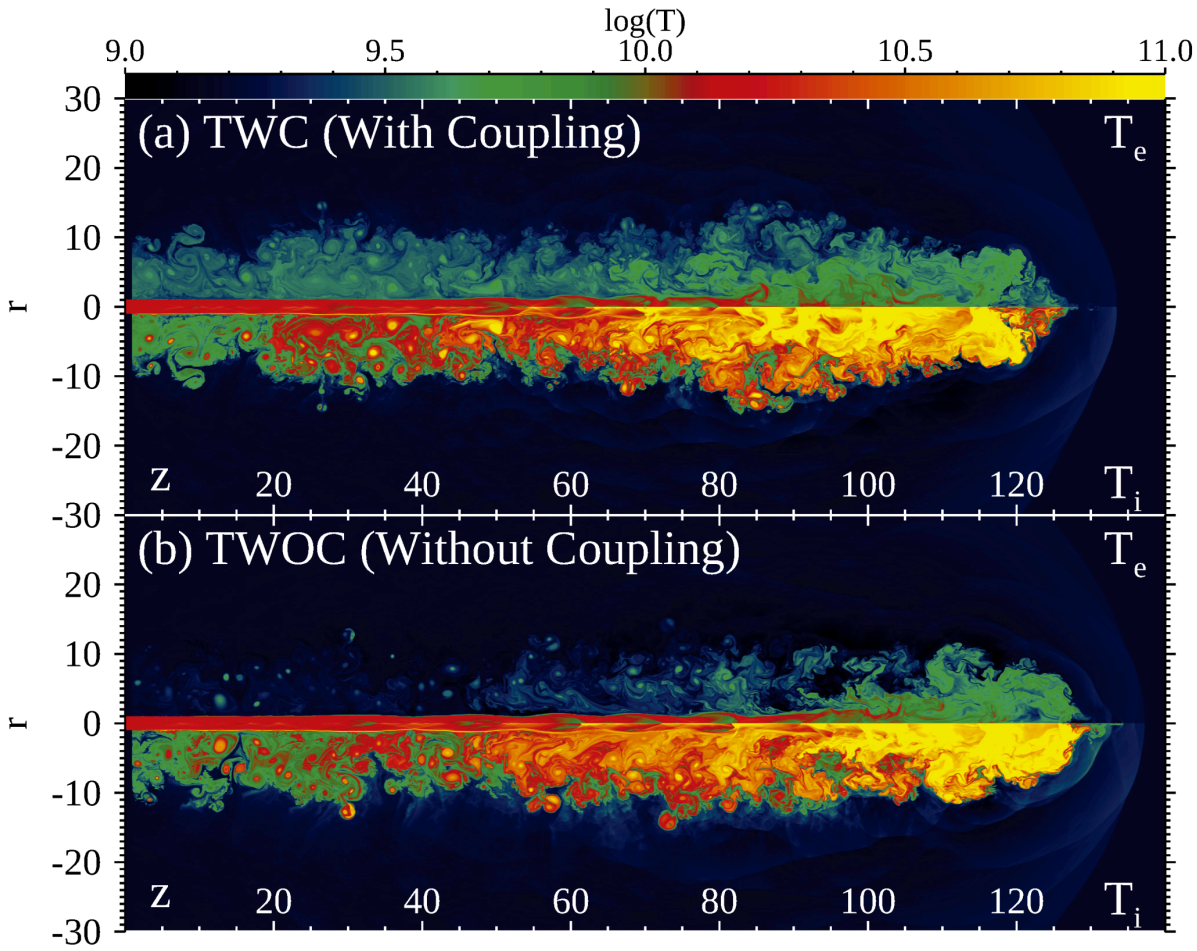

Fig. 3.3: (a): The distribution of the electron temperature (top) and ion temperature (bottom) for model TWC, including Coulomb coupling. (b): Same as (a), but for model TWOC, not including Coulomb coupling. (credit: Ohmura et al., 2019)

an ideal gas, and the internal energies of ions and electrons are thus

$$\epsilon_{\rm i} = \frac{p_{\rm i}}{\gamma_{\rm i} - 1}, \quad \epsilon_{\rm e} = \frac{p_{\rm e}}{\gamma_{\rm e} - 1}, \tag{3.13}$$

where $\gamma_{\rm i}$ and $\gamma_{\rm e}$ are respectively the specific-heat ratios for ions and electrons. We consider two types of heating source in the energy equation of the electron. One is $q^{\rm ie}$, which is the rate of energy transfer from ions to electrons through Coulomb coupling. $q^{\rm heat}$ is a dissipative heating rate. Here $f_{\rm e}$ is the fraction of electron heating, and depends on the microscopic properties of a collsionless plasma in various dissipation process. $q^{\rm rad}$ is energy loss rate via radiation.

The pressure and internal energy of each species are thus given by the ideal equation of state (Chandrasekhar, 1939),

$$p_{\rm s} = n k_{\rm s} T_{\rm s}, \tag{3.14}$$

$$\epsilon_{\rm s} = \rho_{\rm s} c^2 \left(\frac{[3K_3(1/\theta_{\rm s}) + K_1(1/\theta_{\rm s})]}{4K_2(1/\theta_{\rm s})} - 1 \right) \equiv \frac{p_{\rm s}}{\gamma_{\rm s}(\theta_{\rm s}) - 1}, \tag{3.15}$$

where subscripts $s \in \{{\rm i}, {\rm e}\}$ denote electrons and ions, respectively. $\gamma_{\rm s} = 5/3$ in the non-relativistic limit ($\theta_{\rm s} \to 0$), and $\gamma_{\rm s} = 4/3$ in the ultra-relativistic limit ($\theta_{\rm s} \to \infty$). The effective temperature of the electron and ion mixed gas is

$$p_{\rm gas} = p_{\rm i} + p_{\rm e} = (\gamma_{\rm gas} - 1)\epsilon_{\rm gas} = 2 n k_{\rm B} T_{\rm gas}, \tag{3.16}$$

where $\epsilon_{\rm gas}$ is the gas internal energy.

3.4.1 Numerical code

We modified the MHD code CANS+ (Matsumoto et al., 2019) to include the energy equation for electrons. CANS+ solves the Newtonian–MHD equations in conservation form as follows:

1. Reconstruction adopts a fifth-order monotonicity-preserving interpolation scheme (Suresh & Huynh, 1997).

2. The time integral is performed with third-order total-variation-diminishing preserving Runge–Kutta methods.

3. The numerical flux across cell interfaces is computed using the HLLD Riemann solver (Miyoshi & Kusano, 2005).

4. The hyperbolic divergence cleaning method is adopted for a magnetic field (Dedner et al., 2002).

3.5 Application of astrophysical jets

This work is completely based on the assumption that the plasma dynamics are described by the theory of magnetohydrodynamics. This assumption is verified when the characteristic scale length of jet propagation ($\sim$ kpc) is large compared to the mean free path. The hydrodynamic mean free path is significantly larger than the characteristic scale because the jet and ICM plasma are collisionless. Meanwhile, the magnetic field interacts with the particles and hence MHD mean free path regard as typically gyro-radius:

$$r_{\rm g} = \frac{m_{\rm i} v c}{eB} \sim 10^{10} \times \left(\frac{T_{\rm i}}{10^8\ {\rm K}}\right)^{1/2} \left(\frac{B}{\mu{\rm G}}\right)^{-1} \ {\rm cm} \ll {\rm kpc}. \tag{3.17}$$

Therefore, MHD approximation is valid.

Typical value of density and temperature of ICM are $n \sim 10^{-2} - 10^{-4}$ g cm$^{-3}, T \sim 10^7 - 10^8$ K, respectively. Therefore, the relaxation time-scale via Coulomb coupling is estimated by Eq. (3.6) as

$$t_{\rm ie} = 2.0 \times 10^2\ {\rm Myr} \left(\frac{\ln\Lambda}{40}\right)^{-1} \left(\frac{n}{10^{-3}\ {\rm cm}^{-3}}\right) \left(\frac{T_{\rm e}}{10^8\ {\rm K}}\right)^{3/2}. \tag{3.18}$$

Note that this value is a lower limit because the jets have higher temperature and lower density than that of ICM. The typical outburst age of jets are within 100 Myr (McNamara & Nulsen, 2007). In particular, the outburst age for Cygnus A, which is the most typical FR-II type radio source, is estimated at 20 Myr (Snios et al., 2018). Therefore, shocked-ICM and jets are expected to be in two-temperature states.

4 The effect on the fraction of electron heating in two-temperature jets

4.1 Short introduction

As we discussed in Sect. 3.5, electrons and ions should be decoupled in extragalactic jet. Although our previous work in Ohmura et al. (2019) have been conducted two-temperature simulations for X-ray binary jets, they ignored the effect of instantaneous heating at shock fronts. However, this effect are supported by theoretical and observational studies (see Sect. 3.3). Moreover, previous work assumed that the jet temperature of ions and electrons are equal, but it is not certain. Therefore, we should examine the effect of instantaneous heating on the electron temperature distribution and the dependence of electron and ion temperatures on injection conditions.

In this chapter, we report the results of two-temperature MHD simulations of a sub-relativistic AGN jet that propagates and interacts with the ICM, including Coulomb coupling and instantaneous electron heating at shocks for the first time. The remainder of the chapter is organized as follows. Section 4.2 describes basic equations for the two-temperature and single-fluid MHD simulation and the numerical setup for two-dimensional simulations. Sections 4.4 and Sect. 4.5 respectively present and discuss our results. Section 4.6 presents conclusions.

4.2 Numerical method

4.2.1 Basic equation

Our numerical code solves the equations in conservation form. We therefore arrange the two-temperature MHD equations in conservation form:

$$\frac{\partial \boldsymbol{U}}{\partial t} + \nabla \cdot \boldsymbol{F} = \boldsymbol{S}, \tag{4.1}$$

$$\boldsymbol{U} = \begin{pmatrix} n \\ m_{\rm i} n \boldsymbol{v} \\ \boldsymbol{B} \\ e \\ n\kappa_{\rm e} \end{pmatrix}, \tag{4.2}$$

$$\boldsymbol{F} = \begin{pmatrix} n\boldsymbol{v} \\ m_{\rm i} n \boldsymbol{v}\boldsymbol{v} + p_{\rm T}\boldsymbol{I} - \frac{1}{4\pi}\boldsymbol{B}\boldsymbol{B} \\ \boldsymbol{v}\boldsymbol{B} - \boldsymbol{B}\boldsymbol{v} \\ (e + p_{\rm T})\boldsymbol{v} - \frac{1}{4\pi}\boldsymbol{B}(\boldsymbol{v}\cdot\boldsymbol{B}) \\ n\kappa_{\rm e}\boldsymbol{v} \end{pmatrix}, \tag{4.3}$$

$$\boldsymbol{S} = \begin{pmatrix} 0 \\ 0 \\ 0 \\ 0 \\ (\gamma_{\rm e} - 1) n^{1-\gamma_{\rm e}} (q^{\rm ie} + f_{\rm e} q^{\rm heat}) \end{pmatrix}, \tag{4.4}$$

where $\boldsymbol{U}$ and $\boldsymbol{F}$ respectively denote the conserved quantities and flux vectors, $\boldsymbol{I}$ is a unit matrix, $\boldsymbol{S}$ is the source term, and the total energy, e, is given by

$$e = \epsilon_{\rm i} + \epsilon_{\rm e} + \frac{1}{2}\rho\boldsymbol{v}^2 + \frac{1}{8\pi}\boldsymbol{B}^2. \tag{4.5}$$

$p_{\rm T} = p_{\rm i} + p_{\rm e} + p_{\rm mag}$ is total pressure. We have here used the electron pseudo-entropy $\kappa_{\rm e} \equiv p_{\rm e} n^{-\gamma_{\rm e}}$. The electron gas entropy per particle is given by

$$s_{\rm e} = k_{\rm B}(\gamma_{\rm e} - 1)^{-1} \log\left(p_{\rm e} n^{-\gamma_{\rm e}}\right) = k_{\rm B}(\gamma_{\rm e} - 1)^{-1} \log \kappa_{\rm e}. \tag{4.6}$$

The source term is updated implicitly by adopting the Newton–Raphson iteration.

4.2.2 Calculation of dissipation heating

To calculate the dissipation heating rate [*)] $q^{\rm heat}$, we adopt an approach similar to that followed by Ressler et al. (2015) and Sadowski et al. (2017). We adopt the following to evaluate the dissipated energy at each time step.

1. We solve the conserved equations (Eq. (5.1)), and obtain the gas specific internal energy $\epsilon_{\rm gas}$ at time step $n+1$:

$$\epsilon_{\rm gas}^{n+1} = \frac{p_{\rm gas}^{n+1}}{\gamma_{\rm gas} - 1}. \tag{4.7}$$

2. To compute the purely adiabatic evolution, we use the gas entropy conservation equation:

$$\frac{\partial}{\partial t}\left(n\kappa_{\rm gas}\right) + \nabla \cdot \left(n\kappa_{\rm gas}\boldsymbol{v}\right) = 0, \tag{4.8}$$

where $\kappa_{\rm gas}$ is the gas pseudo-entropy. To solve the above equation, we solve the finite difference equation between the n-th and $(n+1)$-th time step for each cell and adopt the fifth-order monotonicity-preserving method. The gas specific thermal energy that evolves under the adiabatic process is then calculated as

$$\epsilon_{\rm gas,ad}^{n+1} = \frac{\left(\kappa_{\rm gas} n^{\gamma_{\rm e}}\right)^{n+1}}{\gamma_{\rm e} - 1}. \tag{4.9}$$

3. The dissipation heating rate is therefore estimated as

$$q^{\rm heat} = \frac{\epsilon_{\rm gas}^{n+1} - \epsilon_{\rm gas,ad}^{n+1}}{\Delta t}. \tag{4.10}$$

[*)] In our simulations, we solve ideal MHD equations, and numerical viscosity is the origin of dissipation.

4.3 Numerical setup

We present the results of 10 models used to investigate the effect of electron heating on the electron temperature distribution and the dependence of electron and ion temperatures on the initial conditions. We perform axisymmetric simulations of the large-scale jet evolution when the jet is injected into a medium having constant density.

Parameters common to all models are summarized in Tab. 4.1. The computational domain is $0 < r/r_{\rm jet} < 40$, $0 < z/r_{\rm jet} < 80$ and the number of numerical cells is $(N_{\rm r}, N_{\rm z}) = (1024, 2048)$. The initial radius of the jet is 1 kpc, resolved by 24 numerical cells. The initial Mach number of jets $\mathcal{M}_{\rm jet}$ is 14, and the ratio of the thermal pressure of the jet to the ICM is 10. The speed of the injected jet is 0.2c. The components of the injected magnetic field are

$$\begin{aligned} B_\phi &= \begin{cases} B_{\rm in} \sin^4 (2\pi r/r_{\rm jet}) & (r < r_{\rm jet}) \\ 0 & (\text{otherwise}) \end{cases} \\ B_{\rm r} &= B_{\rm z} = 0, \end{aligned} \tag{4.11}$$

where $B_{\rm in}$ is given by the plasma beta as $B_{\rm in} = (8\pi p_{\rm gas}/\beta)^{1/2}$, with $\beta = p_{\rm gas}/p_{\rm mag}$. The temperature of the injected gas is $T_{\rm gas} = 0.5(T_{\rm e} + T_{\rm i}) = 1.0 \times 10^9$ K. The initial ICM is unmagnetized, and the density ratio of the jet beam to the ICM ($\eta \equiv \rho_{\rm jet}/\rho_{\rm ICM}$) is 10^{-2}.

Table 4.2 presents our numerical models. We adopt three values of the fraction of electron heating, $f_{\rm e} = 0.0, 0.05, 0.2$, in studying the effect of electron heating. The ratio of injected electron and ion temperatures is set at $m \equiv T_{\rm e,inj}/T_{\rm gas,inj} = 1.9, 1.0, 0.1$ to examine the dependence on the injection temperatures. Moreover, we switch on and off Coulomb coupling.

4.4 Results

In Appendix A.1, we show the result of the one-dimensional Riemann problem for our jet model to examine the electron temperature dependence on the fraction of the electron heating $f_{\rm e}$ at shock fronts. We find that the post-shock temperature ratio of the electron to ion is simply described by Eq. (A.3). In this section, we investigate the multidimensional effects and the dependence on the temperatures of the injected electrons and ions. In

Table 4.1: Common simulation setup parameters

Jet speed	$v_{\rm jet}$	0.2c
Jet gas temperature	$T_{\rm g,jet}$	1.0×10^9 K
Jet plasma β	β	10
Jet Mach Number	$\mathcal{M}_{\rm jet}$	14
Ambient gas density	$\rho_{\rm ICM}$	$0.835 \times 10^{-24}\alpha$
Ambient gas temperature	$T_{\rm ICM}$	1.0×10^6 K
Density ratio	$\rho_{\rm jet}/\rho_{\rm ICM})$	10^{-2}
Gas pressure ratio	$p_{\rm jet}/p_{\rm ICM}$	10

Table 4.2: Simulation models. The columns give the model name, ratio of the injection electron temperature to the gas temperature, the fraction of the electron heating, Coulomb coupling, and normalized density parameter.

Model	$m \equiv T_{\rm e,inj}/T_{\rm gas,inj}$	$f_{\rm e}$	Coulomb coupling	α
f00m1	1	0.0	-	1
f00m1C	1	0.0	ON	1
f005m1	1	0.05	-	1
f005m1C	1	0.05	ON	1
f02m1	1	0.2	-	1
f02m1C	1	0.2	ON	1
f02m0.1C	0.1	0.2	ON	1
f02m1.9C	1.9	0.2	ON	1
f005m1Cα-1	1	0.05	ON	10^{-1}
f005m1Cα-2	1	0.05	ON	10^{-2}

addition, we present the time evolution to clarify when and where Coulomb coupling is effective.

4.4.1 Morphology and temperature distribution

This subsection presents the results of a fiducial model of jet propagation. The fiducial model is the model f005m1C. Figure 4.1 shows snapshots of (a) the number density, (b) the gas pressure, (c) the toroidal magnetic field component, (d) the vorticity squared, and (e) the absolute velocity at $t = 20.0$ Myr. When the jet propagates into the ICM, several types of shock front form; e.g., internal shocks (i.e., recollimation shocks), the terminal shock (i.e., reverse shock), and the bow shock (i.e., forward shock). In addition, the shocked matter of the terminal shock forms a backflow called a cocoon. The bow shock compresses the ICM and forms a high-density shell called the shocked-ICM between the contact discontinuity and bow shock. The kinetic energy dissipates and convert to thermal energy at shocks, and the pressure of the post-shock gas thus becomes 10 to a 100 times that of the pre-shocked gas.

In our jet model, the magnetic energy is much less than the kinetic and thermal energy. Therefore, the Lorentz force does not have a practical effect on the dynamics and morphology. When the plasma reaches the terminal shock, the kinetic energy is converted into magnetic energy and gas internal energy. The backflow generates the vortex motion in the cocoon, and the intensity of the magnetic field increases to about twice that of the injection field. The toroidal component is not converted into a poloidal component because of axisymmetry and the absence of jet angular motion. However, Gaibler et al. (2009) showed that toroidal fields are dominant in a cocoon under an axisymmetric condition when the jet has angular momentum. Note that the poloidal and toroidal fields might easily convert into one another in three-dimensional simulations.

The beam structure depends on the ratio of the jet pressure to the ICM pressure (Norman et al., 1982). Because we choose the pressure ratio to be greater than unity (i.e., the jet beam is under-expanded), the beam has shock diamonds and a sequential structure of compression and expansion. The beam accelerates to 0.22c, which is 110% of the injection velocity, through the expanding motion. The beam velocity decelerates through the terminal shock, and the bulk velocity of backflowing plasma is about 0.1c.

KH instabilities develop and form the vortex motion by interaction with the backflowing plasma and shocked-ICM in the cocoon. The vortex motions drive pressure waves that convert the kinetic energy into the thermal energy in the shocked-ICM through dissipation (Bambic & Reynolds, 2019). Furthermore, the vortices create high-temperature and low-density spots.

The remaining panels of Fig. 4.1 show snapshots of (f) the energy transfer ratio from ions to electrons through Coulomb coupling, (g) the ion temperature, (h) the electron temperature, and (i) the temperature ratio of electrons to ions at $t = 20.0$ Myr. The electron temperature and ion temperature are decoupled due to the heating at the bow shock. In the shocked ICM, however, ions and electrons are in thermal equilibrium because the relaxation time of Coulomb coupling, which is proportional to the square of the number density, is shorter than the hydrodynamical time scale. Meanwhile, ion and electron temperatures are separated through internal shocks in the beam. The post-shock ion and electron temperatures at the terminal shock are about 10^{11} and 10^{10} K, respectively. These values are in good agreement with values obtained in the one-dimensional simulation (see Fig. A.2). The collision time scale is longer than the dynamical time scale in the low-density cocoon, and the electron temperature thus remains lower than the ion temperature. Around the interface between the cocoon and the shocked ICM, the ion and electron temperatures decrease to 10^8 K owing to turbulent mixing.

4.4.2 Dependence on the fraction of electron heating

We studied the dependence on the fraction of electron heating f_e by carrying out simulations for $f_e = 0$ (model f00m1C), 0.05 (model f005m1C), and 0.2 (model f02m1C). Other parameters are the same in these three models. Figure 4.2 shows snapshots of the temperature ratio of electrons to ions for models f00m1C (left), f005m1C (center), and f02m1C (right). Figure 4.3 shows the ratio of the electron temperature to the ion temperature along the jet beam ($r = 0.25$ kpc) for models f00m1C (blue), f005m1C (black), and f02m1C (red). The red dashed line and black dashed line respectively show the temperature ratio of the electron to ion for $f_e = 0.2$ and 0.05 predicted using Eq. (A.3). The blue dashed line shows the post–shock temperature ratio when $f_e = 0$ obtained using Eq. (A.2). The ion and electron temperatures separate at the first oblique shock for all mod-

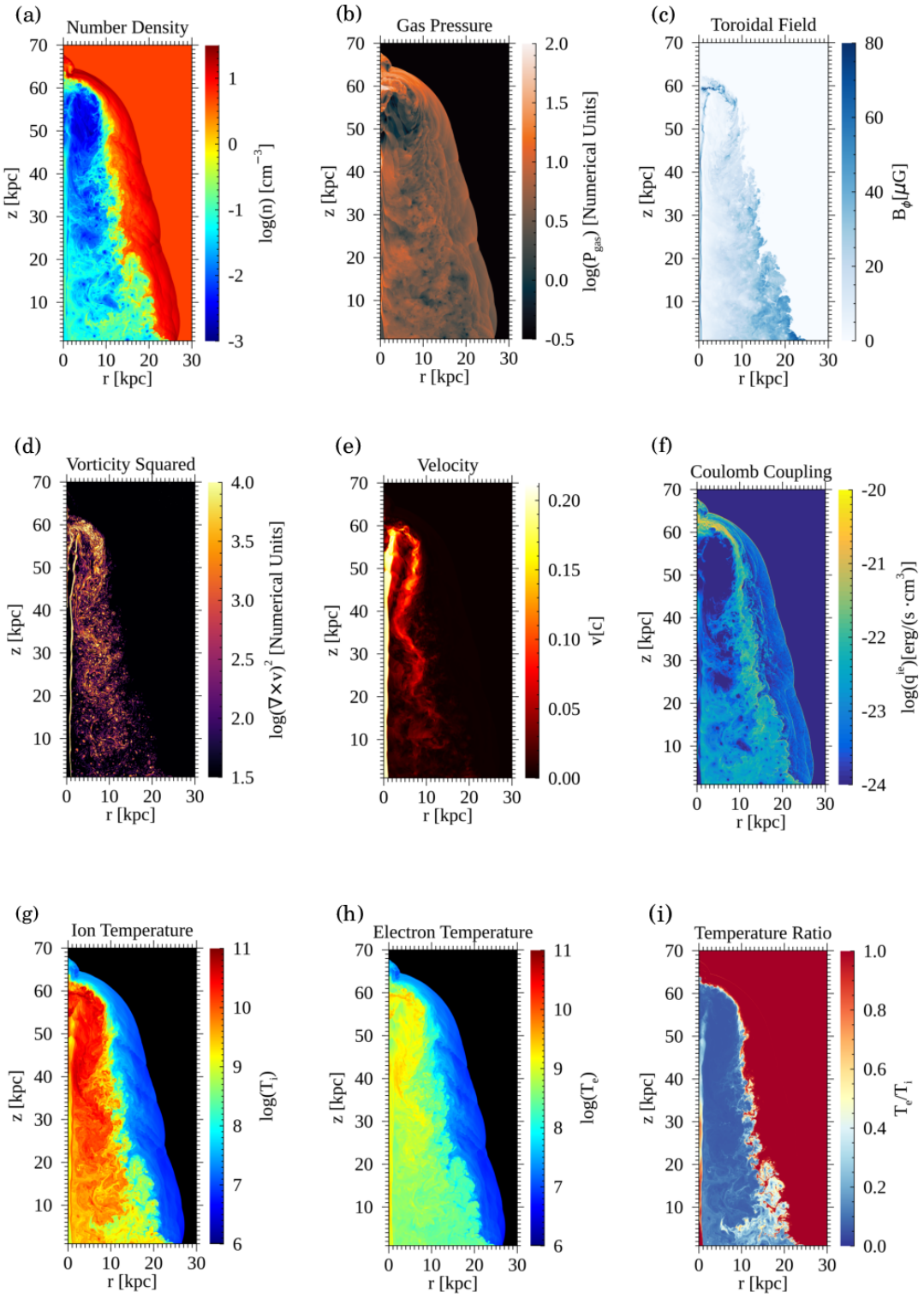

Fig. 4.1: Snapshots of (a) the number density, (b) the gas pressure, (c) the toroidal magnetic field, (d) the vorticity squared $(\nabla \times \boldsymbol{v})^2$, (e) the flow absolute velocity, (f) the energy transfer rate from ions to electrons through Coulomb coupling, (g) the ion temperature, (h) the electron temperature, and (i) the temperature ratio of electrons to ions for model f005m1C ($f_e = 0.05$) at $t = 20.0$ Myr.

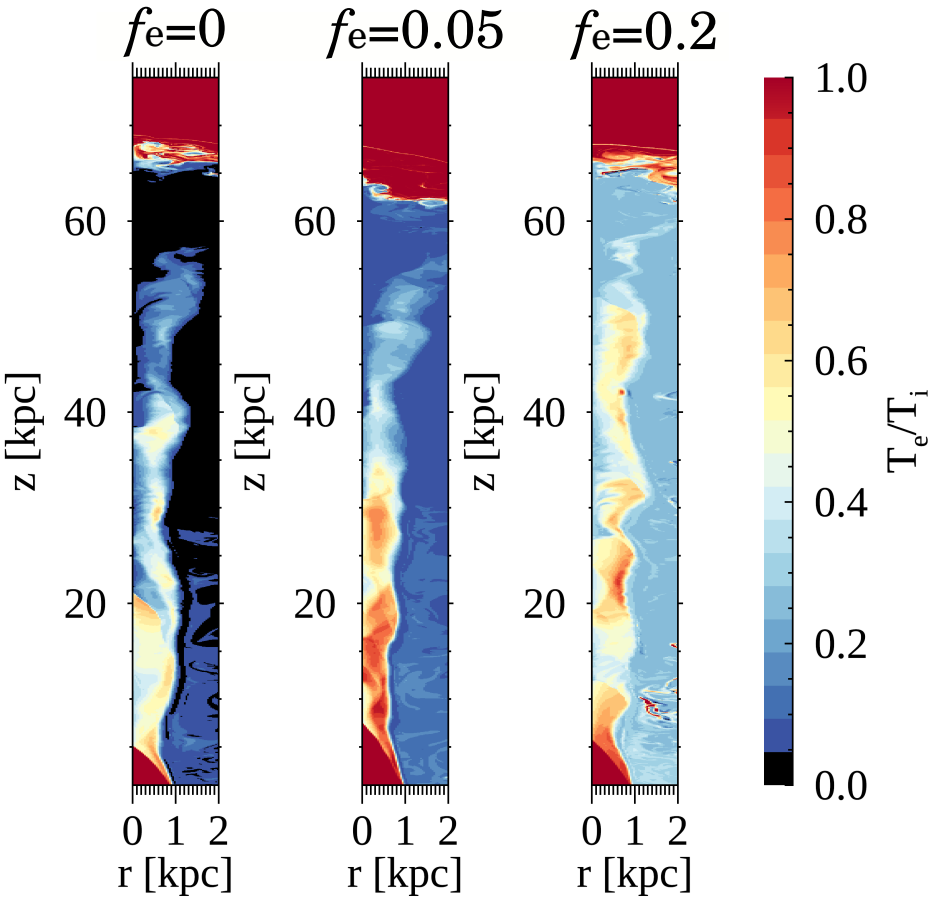

Fig. 4.2: Snapshots of the temperature ratio of electrons to ions in the beam for models f00m1C (left), f005m1C (center), and f02m1C (right).

els. The post-shock temperature ratios of electrons and ions at the first oblique shocks are about 0.5 because there remains the effect of electron adiabatic heating. The temperature ratio approaches the temperature ratio predicted using Eq. (A.3) when $f_e \neq 0$ for each shock (see Sect. A.1). The post-shock temperature ratios are close to the predicted values at the terminal shock in the cases that $f_e = 0.05$ and 0.2 as gas flows through the beams. In contrast, the post-shock temperature ratio at the terminal shock is lower than 0.01 for the model f00mC. This value is smaller than that of the one-dimensional Riemann problem because the electron temperature is reduced by the gas expansion at the hotspot (Fig. 4.3 (blue)). This result indicates that multidimensional effects become important when f_e is small.

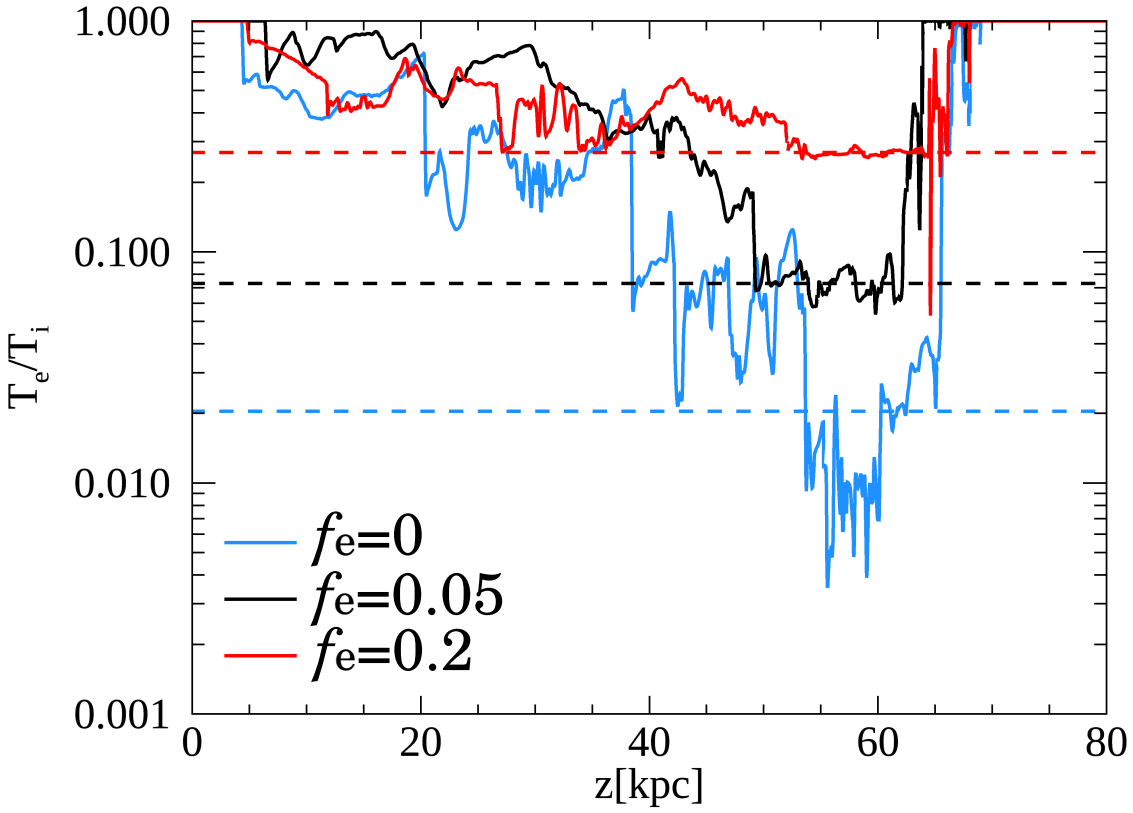

Fig. 4.3: Profiles of the temperature ratio of electrons to ions along the jet beam (r = 0.25 kpc) for models f00m1C (blue), f005m1C (black), and f02m1C (red). The red dashed line and black dashed line respectively show temperature ratios of electrons to ions for $f_e = 0.2$ and 0.05 predicted using eq. (A.3). The blue dashed line shows the post-shock temperature ratio when $f_e = 0$ obtained from eq. (A.2).

4.4.3 Dependence on temperatures of injected ions and electrons

This section compares results for models f02m1C, f02m0.1C, and f02m1.9C to examine the dependence on the temperatures of injected electrons and ions. These models are the same in that they have $f_e = 0.2$ with Coulomb coupling but they differ in terms of the temperatures of injected electrons and ions. Note that the Mach numbers for the plasma are the same in the three models. Figure 4.4 shows the temperature profiles of electron (left) and ion (right) along the jet beam at $r = 0.25$ kpc for models f02m1C (black), f02m1.9C (red), and f02m0.1C (blue). Both electron and ion temperatures increase through the internal shocks. The electron temperatures of three models are almost the same in the post-shock region of the terminal shock, even though the injection temperatures are different. This is because the energy dissipated at the terminal shock is much greater than the initial thermal energy. Therefore, if we know the Mach number of internal jet, we can easily estimate the electron temperature at the hotspot using eq. (Fig. A.3). Note that the fraction of electron heating f_e could be a function of the temperature ratio. Meanwhile, when the temperature jump is smaller than the difference between the electron and ion temperatures at a shock (i.e., the Mach number is low or f_e is small), the effect of injection must be considered. The electron temperature at the hotspot and in the cocoon thus depends strongly on the temperature ratio of injected plasma when $f_e = 0$.

4.4.4 Temperature time evolution and the effect of Coulomb coupling

This section presents the temperature evolution. We investigate the time evolution of the energy of electrons and ions. We divide the whole system of the jet–ICM interaction into four areas that correspond to different physical conditions, namely the beam, the cocoon, the shocked ICM, and the unperturbed ICM. Figure 4.5 presents an example of such division at $t = 20.0$ Myr for model f005m1C. The beam region is identified by a high bulk flow speed. We define the threshold $v_z > 0.9 v_{z,inj}$ to distinguish the beam from the cocoon. The growth of instabilities makes it difficult to distinguish between the

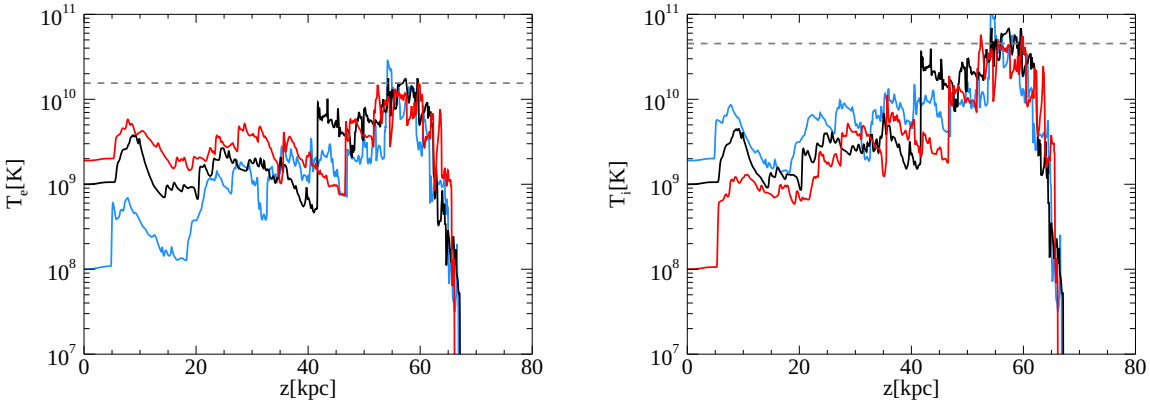

Fig. 4.4: Temperature profiles of the electron (left) and ion (right) along the jet beam at $r = 0.25$ kpc for models f02m1C (black), f02m1.9C (red), and f02m0.1C (blue). The dashed gray lines show the post-shock electron (left) and ion (right) temperatures predicted using eq. Eq. (A.3).

cocoon and the shocked ICM. However, we assume that the initial ICM is not magnetized. Therefore, the toroidal field can be used to trace the cocoon, i.e., $|B_\phi| > 0$ for the cocoon. Finally, the shocked-ICM and unperturbed-ICM regions are distinguished according to whether the gas pressure is higher than its initial value. Figure 4.6 shows the evolution of the volume-weighted density,

$$\bar{\rho} = \frac{\iint 2\pi r \rho dr dz}{\iint 2\pi r dr dz}, \tag{4.12}$$

in the cocoon (dashed), the shocked ISM (dotted), and the beam (solid) for the model f005m1C. Initially (< 0.3 Myr), the backflowing gas directly interacts with the boundary at $z = 0$. However, we only consider the period after 0.5 Myr. The volume-weighted density of the shocked ICM is twice that of the initial ICM density, $20\rho_0$, owing to the shock compression and does not change with time. Additionally, the volume-weighted density of the beam mostly remains at its initial level, $0.1\rho_0$. Meanwhile, the volume-weighted density decreases in the cocoon because of the volume expansion. A low-density ($\rho \sim 10^{-3}\rho_0$) cavity forms around the hotspots (see Fig. 4.1 (a)). However, the volume of the cavity is small compared with the volume of the cocoon. The mixing region beside the contact discontinuity has a high density and large radius. In the mixing region beside the contact discontinuity, the density is low and radius of that is large. The volume-weighted density of the cocoon thus remains higher than that of the beam gas.

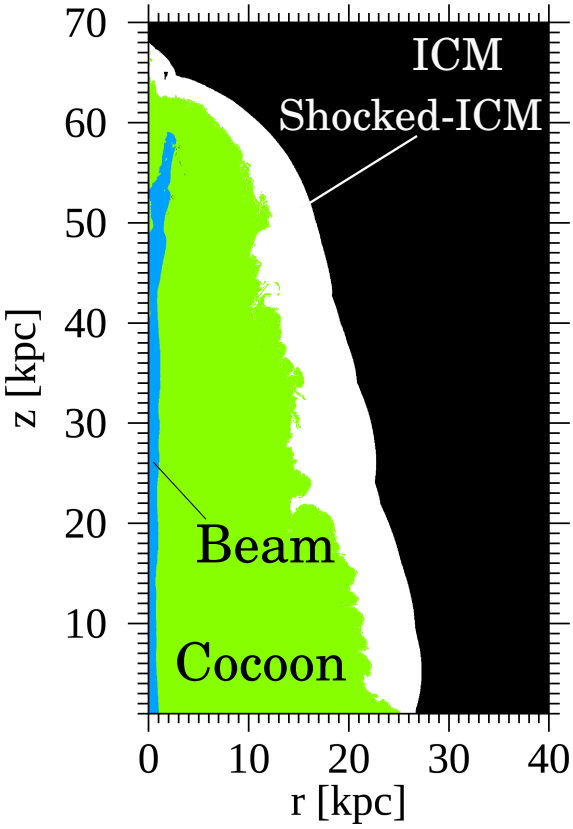

Fig. 4.5: Example of divided areas at $t = 20.0$ Myr for model f005m1C. We define that the beam (blue) is the region where $v_{\rm z} > 0.9 v_{\rm z,inj}$ and the cocoon (green) is the region where there is a toroidal magnetic field except for the beam region. The shocked ICM (white) has gas pressure higher than its initial value.

Figure 4.7 and Fig. 4.8 show the evolution of the volume-weighted average electron and ion temperatures,

$$\bar{T_{\rm i}} = \frac{\iint 2\pi r T_{\rm i} dr dz}{\iint 2\pi r dr dz}, \quad \bar{T_{\rm e}} = \frac{\iint 2\pi r T_{\rm e} dr dz}{\iint 2\pi r dr dz}, \tag{4.13}$$

in the cocoon and the shocked ICM as a function of time for f002m1C, f005m1C, f00m1C, and f00m1. The electron temperature of the cocoon strongly depends on $f_{\rm e}$ because the shocked gas heated at the terminal shock forms the cocoon. Meanwhile, the ion temperature is not sensitive to $f_{\rm e}$ in the range $f_{\rm e} < 0.2$. The heating time scale of electrons, $t_{\rm heat} \equiv n k_{\rm B} T_{\rm e}/q^{\rm ie}$, is about 10^{2-3} Myr in the cocoon. Thus, electrons and ions are not in thermal equilibrium in the cocoon. The volume-weighted temperature in the cocoon decreases because the gas in the mixing region, where r is large, makes a large contribution to the volume-weighted temperature. Coulomb coupling does not make a large contribution to electron heating in the case of the models with $f_{\rm e} = 0.05$ and simulation time of 0.2 Myr. If we carry out longer simulations, we expect that the temperatures become low and Coulomb coupling becomes dominant. In contrast, electrons warm appreciably through Coulomb coupling in the case that $f_{\rm e} = 0$ (f00m1 and f00m1C in Fig. 4.7). For all models, ions are hardly affected by Coulomb coupling and, the ion temperature remains high. Coulomb coupling dominates in the gas mixing region, and the electron temperature remains high even in the case that $f_{\rm e} > 0$ after $t > 10$ Myr.

In the shocked ICM, the three models with Coulomb coupling reach thermal equilibrium between ions and electrons within 1–2 Myr. Coulomb coupling affects electrons and ions regardless of $f_{\rm e}$ because the shocked ICM is denser than the cocoon gas. We thus see that the heating time scale in the shocked ICM is shorter than 1 Myr. The model f00m1, which does not have Coulomb coupling, is still in a two-temperature state at the end of the simulation. The electron temperature decreases but does not fall below the temperature of the initial ICM.

Figure 4.9 is the same as Fig. 4.8 but for models f005m1C (black), f005m1Cα-1 (pink), f00m1Cα-2 (gray), and f005m1 (cyan) in the shocked-ICM. Here, f005m1Cα-1 and f005m1Cα-2 are respectively the models for which the density parameters are set 10^{-1} and 10^{-2} times lower than the density for the model f005m1C. Coulomb coupling weakens as we reduce the normalized density. Note that the dynamics do not depend on the normalized density because the dynamics of non-relativistic jets are determined

by the density ratio of the jet beam to the ICM and the magnetosonic Mach number. Moreover, Coulomb coupling does not affect the total thermal energy. We clearly see that the relaxation time between electrons and ions is longer when the density parameter α is small. We expect that the relaxation times for the models f005m1Cα-1 and f005m1Cα-2 are respectively 10^2 and 100^2 times the relaxation time for the model f005m1C because Coulomb coupling is proportional to the normalized density. However, electrons and ions reach an equilibrium within 10 Myr for the model f00m1Cα-2. This is because the heating time scale of electrons strongly depends on the electron temperature[†)] , and the heating time scale is shortened by decreasing both temperatures in the shocked ICM.

In the beam area, the electron and ion temperatures are decoupled by internal shocks. The volume-weighted ion temperature is about 5 times that of electrons for the model f02m1C. We estimate that the heating time scale of electrons is about 10 Myr. This value is within our simulation time. In practice, it is difficult to reach thermal equilibrium between electrons and ions because the gas flows into the cocoon continuously within a short time. Furthermore, ions are primarily heated by the internal shocks.

4.5 Discussion

4.5.1 Electron heating at shocks

This section discusses an appropriate $f_{\rm e}$ value for AGN jets, focusing on the bow shock and the terminal shock. The Mach number of the bow shock is greater than 5 because the temperature of the shocked ICM is 10 times the initial temperature, and the Mach number of the terminal shock is about 14.

Observations of bow shocks of the Earth and Saturn and a supernova remnant indicate that the post-shock temperature ratio of ions to electrons is proportional to the magnetosonic Mach number. Vink et al. (2015) derived the equation for the post-shock ion–electron temperature ratio assuming adiabatic heating of electrons and heat exchange

[†)] The ratio of energy transfer through Coulomb coupling is written as $q^{\rm ie} \propto (T_{\rm i} - T_{\rm e})(\sqrt{\pi/2} + \sqrt{\theta_{\rm i} + \theta_{\rm e}})(\theta_{\rm i} + \theta_{\rm e})^{-3/2}$. We here assume $T_{\rm e} = 10^8$K and $T_{\rm i} = 10^9$K and hence $\theta_{\rm e} \sim 10^{-2}$ and $\theta_{\rm i} \sim 10^{-4}$ for the shocked ICM. The equation can be approximated as $q^{\rm ie} \propto (T_{\rm i} - T_{\rm e})\theta_{\rm e}^{-3/2}$. Thus, the heating time scale of electrons is easily estimated as $t^{\rm ie}_{\rm heat} = nk_{\rm B}T_{\rm e}/q^{\rm ie} \propto T_{\rm e}\theta_{\rm e}^{3/2}(T_{\rm i} - T_{\rm e})^{-1}$.

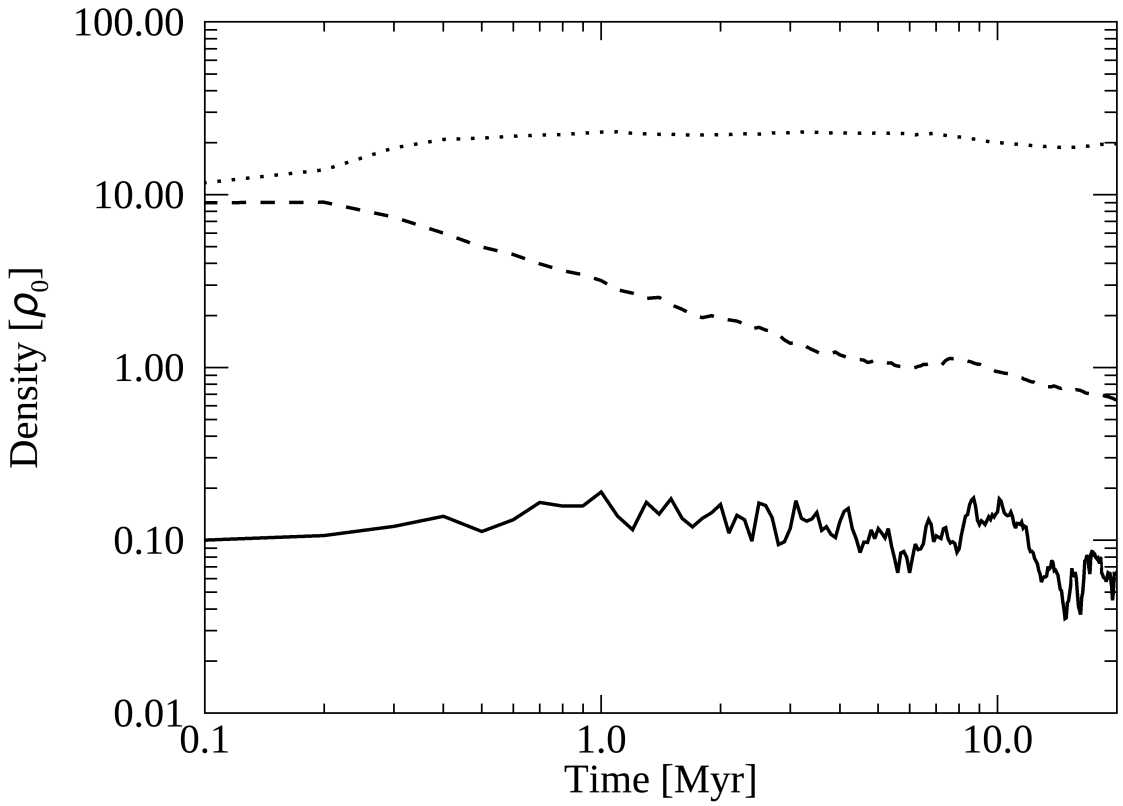

Fig. 4.6: Time evolution of the volume-weighted density in the cocoon (dashed), shocked ISM (dotted), and beam (solid) for model f005m1C.

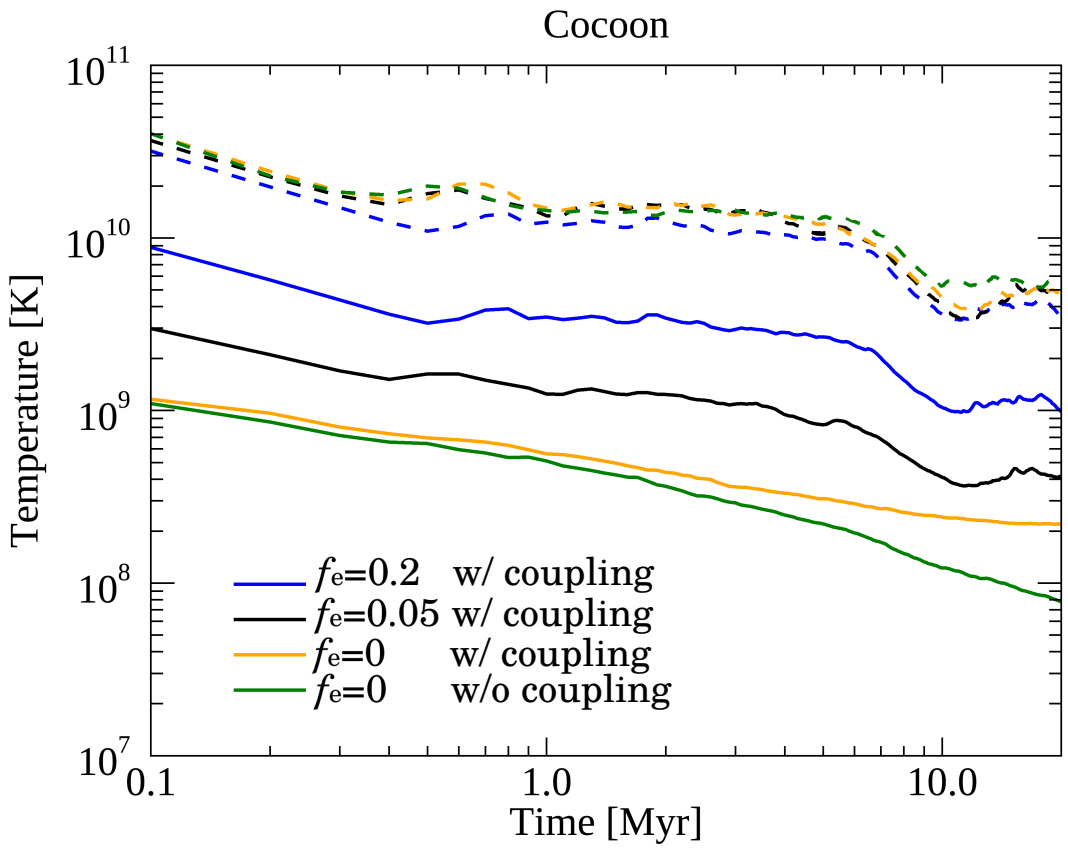

Fig. 4.7: Time evolution of the volume-weighted electron (solid) and ion (dashed) temperatures in the cocoon for models f02m1C (blue), f005m1C (black), f00m1C (yellow), and f00m1 (green).

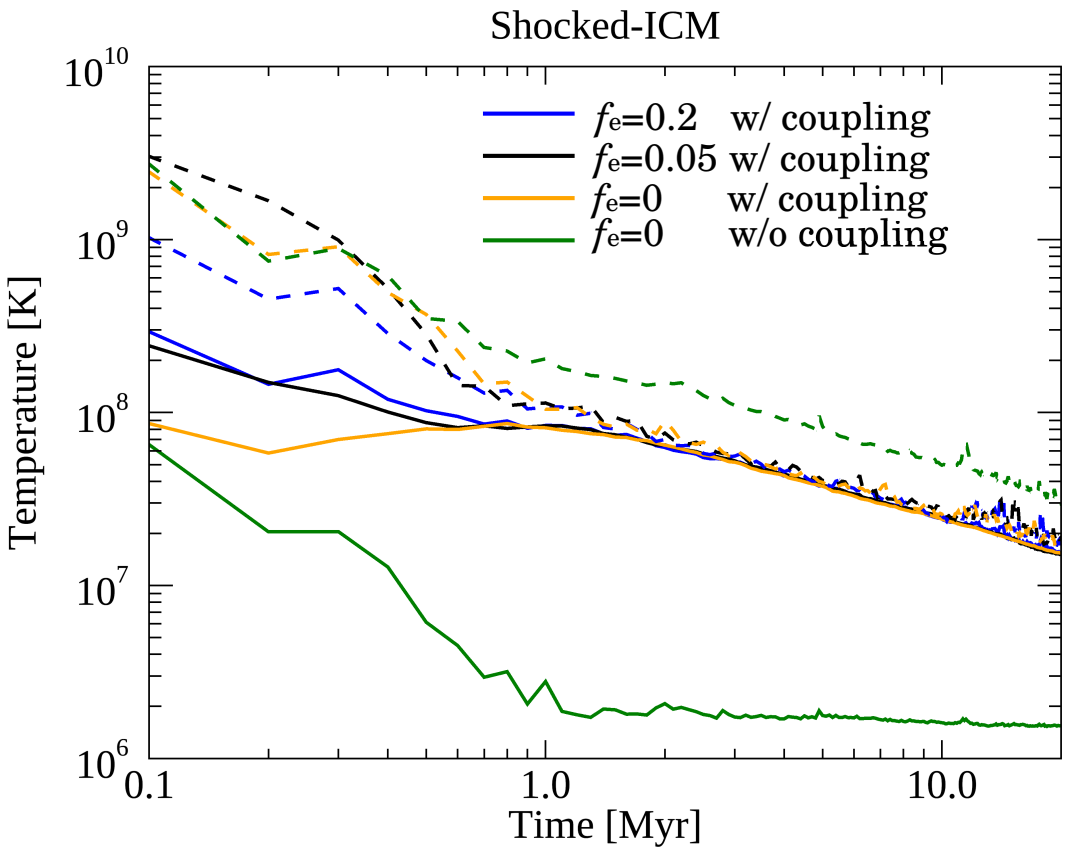

Fig. 4.8: Same as Fig. (4.7) but in the shocked ICM.

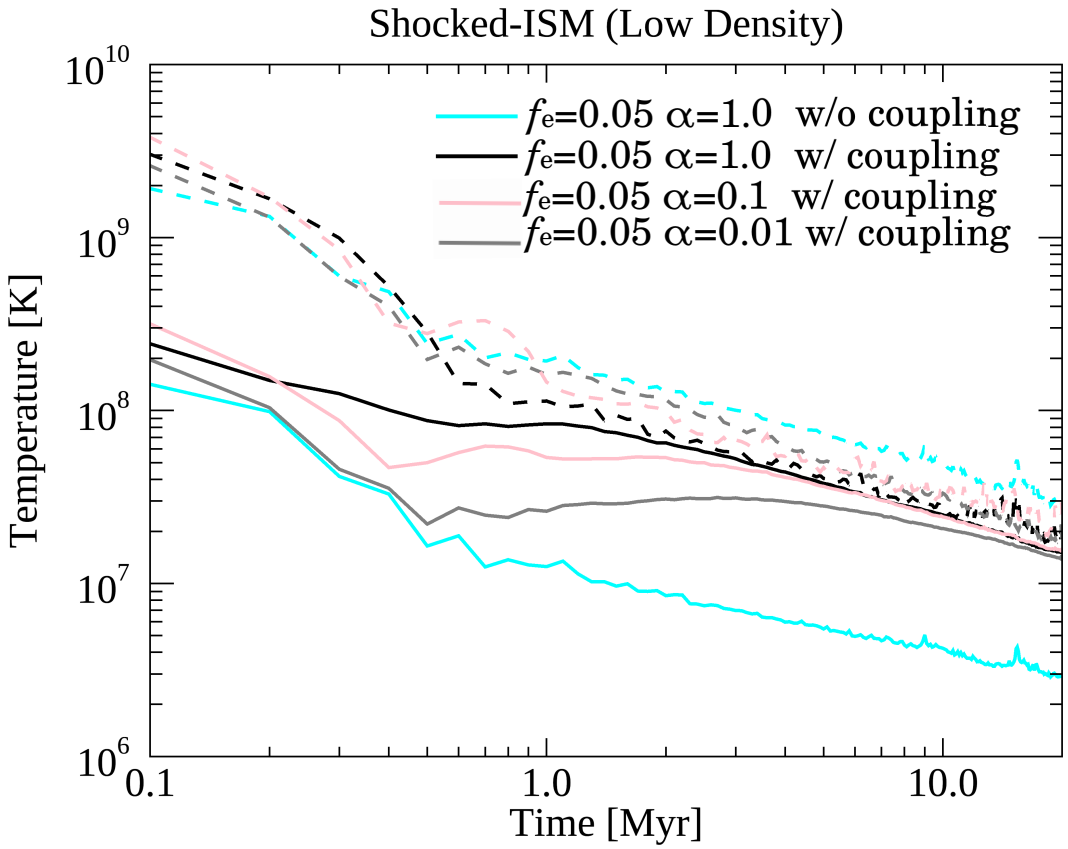

Fig. 4.9: Same as Fig. (4.8) but in the shocked ICM for models f005m1C (black), f005m1Cα-1 (pink), f005m1Cα-2 (gray), and f005m1 (cyan).

between electrons and ions using the exchange factor ζ, which is defined as the fraction of the enthalpy-flux difference between ions and electrons. An appropriate value that explains the observational results is $\zeta = 5\%$. The parameter ζ corresponds to the fraction of the electron heating $f_{\rm e}$ in our work, assuming thermal equilibrium between electrons and ions in the pre-shock region.

The energy exchange ratio in collisionless shocks strongly depends on the development of microscale instabilities, which is affected by the Mach number, the plasma β, the pre-shock temperature ratio, the shock angle, and other factors. Therefore, the theoretical derivation of the fraction of electron heating in collisionless shocks still has large uncertainties. However, some theoretical studies of collisionless shocks showed that shocks primarily heat ions (Crumley et al., 2019; Tran & Sironi, 2020,?). Guo et al. (2018) carried out two-dimensional kinetic particle-in-cell simulations of low-Mach-number shocks, assuming galactic shocks, and showed $T_{\rm e}/T_{\rm i} \sim 0.24$ at $\mathcal{M} = 5$, independent of the plasma beta ranging $4 < \beta < 32$. In addition, Matsukiyo (2010) found that the post-shock temperature ratio is proportional to the magnetosonic Mach number and $T_{\rm e}/T_{\rm i} = 0.01$ when the shock parameters are $\beta = 10$ and $\mathcal{M} = 14$.

The above results indicate that the models for which $f_{\rm e} = 0.2$ overestimate the post-shock electron temperature. Meanwhile, the model for which $f_{\rm e} = 0$ (i.e., electrons are heated only by shock compression) is reasonable for low-Mach-number shocks. However, this model is not appropriate for high-Mach-number shocks because some instantaneous electron heating mechanism is needed. It is noted that instantaneous heating occurs on a time scale shorter than the time scale of Coulomb collision. We therefore argue that the value 0.05 for $f_{\rm e}$ is slightly high but most reasonable in this work.

4.5.2 Cooling and heating time scale

The distribution of radiative intensity and the cooling time scale for two-temperature plasma are different from those for one-temperature plasma. In this subsection, we consider bremsstrahlung radiation for a thermal distribution of electrons as radiative cooling (Rybicki & Lightman, 1986):

$$q^{\rm ff} \sim T_{\rm e}^{1/2} n^2 (1 + 4.4 \times 10^{-10} T_{\rm e}). \tag{4.14}$$

In this work, we assumed that the electron temperature does not exceed the ion temperature anywhere except model f03m1.9C in which the injection temperature of electron is higher than that of ion. Thus, the cooling time scale for two-temperature plasma is much longer than that for one-temperature plasma. The results also indicate that the bremsstrahlung cooling for one-temperature plasma is much stronger than that for two-temperature plasma. It is difficult to observe thermal radiation from a cocoon of an AGN jet because the density is low there. However, Kino et al. (2007, 2009) showed the possibility of a young radio-loud AGN emitting thermal MeV–GeV γ-ray bremsstrahlung radiation. The detection limit is sensitive to the thermalization of electrons and ions in the cocoon.

We next estimate the cooling and heating time scale for plasma, ions, and electrons:

$$t^{\rm ff}_{\rm cool,gas} = nk_{\rm B}T_{\rm gas}/q^{\rm ff}(n^2, T_{\rm e}), \tag{4.15}$$

$$t^{\rm ie}_{\rm cool,i} = nk_{\rm B}T_{\rm i}/q^{\rm ie}(n^2, T_{\rm e}, T_{\rm i}), \tag{4.16}$$

$$t^{\rm ff/ie}_{\rm cool/heat,e} = nk_{\rm B}T_{\rm e}/(q^{\rm ff}(n^2, T_{\rm e}) - q^{\rm ie}(n^2, T_{\rm e}, T_{\rm i})). \tag{4.17}$$

Note that the ratio of the cooling and heating time scale does not depend on density because both bremsstrahlung radiation and Coulomb coupling are proportional to the square of density. In addition, electrons are heated by Coulomb coupling if $q^{\rm ie} > q^{\rm ff}$. If the ion temperature is much higher than the electron temperature and electrons are in a transrelativistic regime, the energy transfer rate via Coulomb coupling is proportional to the ion temperature, $q^{\rm ie} \propto T_{\rm i} - T_{\rm e} \sim T_{\rm i}$ (see Eq. (3.1)). The cooling time scale for ion gas therefore depends on only the gas density, $t^{\rm ie}_{\rm cool,i} \sim 28 n^{-1}$ Myr.

When the ion temperature is higher than the electron temperature, $T_{\rm i} \sim 10T_{\rm e}$, the energy transfer rate $q^{\rm ie}$ for Coulomb coupling is larger than the bremsstrahlung-energy loss rate $q^{\rm ff}$. This means that the electrons continue to be heated by ions. The heating time scale of electrons decreases in proportion to the temperature difference between electrons and ions ($\sim$ plasma). At this time, ions act as a heat bath for electrons because the cooling time scale for ions is much longer than the heating time for electrons. In particular, when

$T_{\rm gas} = 10^{10}$ K and $T_{\rm i} > 0.3T_{\rm e}$, the cooling time scale of ions is 10 times the heating time for electrons.

In this section, we considered only bremsstrahlung radiation and Coulomb coupling. However, viscous heating may affect the temperature evolution in the cocoon where KH instability is developing. (We discuss viscous heating in the next section.) Moreover, other cooling processes, namely thermal synchrotron cooling and Compton cooling, may become dominant. These emission processes are more complicated than the process of bremsstrahlung emission. Simulations including these processes and viscous heating are therefore the next step of our study.

4.5.3 Viscous heating due to turbulence in the cocoon

Vortex motions develop around the surface between the cocoon and the shocked ICM. Our simulations, however, have no explicit means of dissipating sound waves because we use ideal MHD equations. Viscosity induces effective energy diffusion because kinematic viscosity becomes remarkably high in high-temperature plasma, such as the ICM and jets (Braginskii, 1965). The exact value of the heating rate in MHD wave damping is still under debate. Previous two-temperature MHD works on accreting flow used a simple fitting formula based on theoretical models of the dissipation of MHD turbulence in weakly collisionless plasmas developed by Howes (2010). Kawazura et al. (2019) carried out numerical simulations using a hybrid fluid–gyrokinetic model and updated the results of Howes (2010). The fitting formula of Kawazura et al. (2019) (hereafter K19) is

$$\frac{Q_{\rm i}}{Q_{\rm e}} = \frac{35}{1 + (\beta_{\rm i}/15)^{-1.4} \exp\left(-0.1 T_{\rm e}/T_{\rm i}\right)}, \tag{4.18}$$

$$f_{\rm e,turb} = \frac{1}{1 + Q_{\rm i}/Q_{\rm e}}, \tag{4.19}$$

where $Q_{\rm i}, Q_{\rm e}$, and $\beta_{\rm i} \equiv n k_{\rm B} T_{\rm i}/8\pi B^2$ are respectively the heating rates of ions and electrons and the ratio of ion thermal energy to magnetic energy. $f_{\rm e,turb}$ is almost insensitive to $T_{\rm i}/T_{\rm e}$ but depends on $\beta_{\rm i}$ strongly. When thermal energy is dominant ($\beta_{\rm i} > 1$), the turbulence heats primarily ions; i.e., $Q_{\rm i}/Q_{\rm e} > 1$. In contrast, electrons receive most of the heat at low $\beta_{\rm i}$.

To estimate the effect of turbulence heating, we calculate $f_{\rm e,turb}$ from Eq. (4.18) and Eq. (4.19) for model f005m1C at $t = 20$ Myr (Fig. 4.10). Note that K19 is not a suitable model for shocks because the electron heating in shocks is more complicated, which depends on pre-shock physical quantities. Figure 4.10 shows that most of the dissipated energy goes to ions. While magnetic energy accumulates along the contact discontinuity, the pressure of ions still dominates. Therefore, $f_{\rm e,turb}$ is lower than 0.2; i.e., turbulent heating is inefficient for electrons. Of course, if we consider Poynting-flux-dominated jets, electrons could be heated more efficiently than ions. However, it is expected that most magnetic energy is converted to the kinetic energy of bulk motion at sub–parsec scales. Moreover, a three-dimensional magnetic kink instability develops, and the magnetic energy of the jet is converted to internal energy rapidly (Porth & Komissarov, 2015).

Guo (2015) carried out hydrodynamical simulations of the formation and evolution of X-ray cavities in the ICM formed by jets taking into account the kinetic viscosity. They showed that viscosity affects the shape of cavity and suppresses KH instability between the cocoon and the shocked ICM. Therefore, the viscosity provides an efficient energy dissipation mechanism. However, the anisotropic Braginskii viscosity, which transports momentum along the orientation of the magnetic field, cannot suppress KH instability because the toroidal magnetic field is dominated in the cocoon and the effect of viscosity on the velocity shear across the magnetic field lines is inefficient (Suzuki et al., 2013).

4.5.4 Equation of state

Our simulations use the non-relativistic ideal equation of state for both electrons and ions. However, the specific heat ratio changes from 5/3 for a non–relativistic (cold) plasma to 4/3 for a relativistic (hot) plasma. In particular, the relativistic temperature of electrons is about 3.0×10^9 K. Electrons in the jet have therefore reached their relativistic temperature, and the specific heat ratio of electrons becomes 4/3. Meanwhile, ions are non-relativistic in our simulation because the relativistic temperature of ions is about 10^{13} K. The effective adiabatic index for the gas can be calculated as (Ressler et al., 2015)

$$\gamma_{\rm gas} - 1 = \frac{p_{\rm i} + p_{\rm e}}{\epsilon_{\rm i} + \epsilon_{\rm e}} = (\gamma_{\rm e} - 1)(\gamma_{\rm i} - 1)\frac{1 + T_{\rm i}/T_{\rm e}}{(\gamma_{\rm i} - 1) + (\gamma_{\rm e} - 1)T_{\rm i}/T_{\rm e}}. \tag{4.20}$$

Thus, $\gamma_{\rm gas}$ becomes 13/9 if electrons are relativistic.

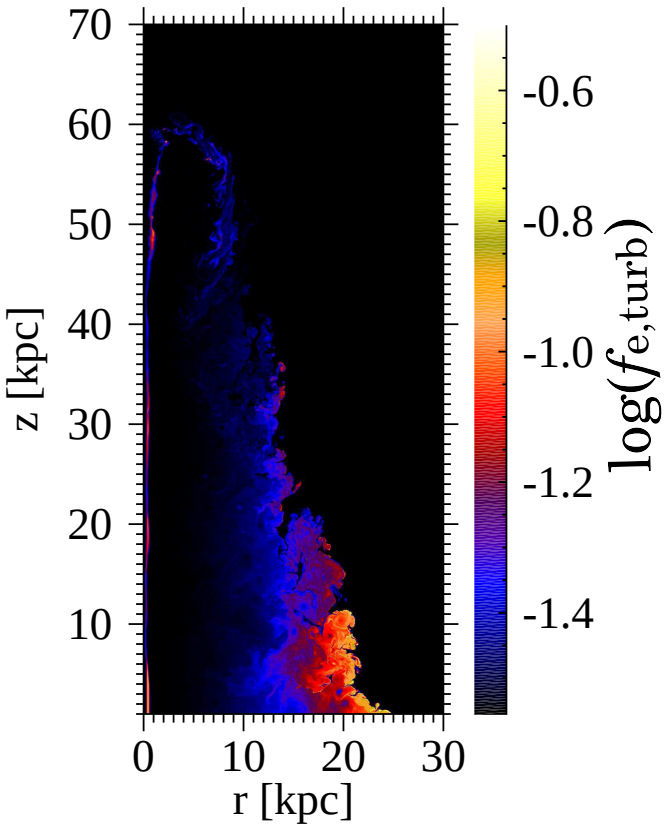

Fig. 4.10: Snapshot of the fraction of electron heating $f_{\mathrm{e,turb}}$ estimated for model f005m1C at $t = 20$ Myr using Eq. (4.18) and Eq. (4.19).

A small value of the specific heat ratio leads to large internal energy. Therefore, a high value of internal energy accelerates the propagation to increase momentum flux in the relativistic regime, $p_{\rm gas} \sim \rho c^2$ (Mignone & McKinney, 2007). In the non-relativistic regime, however, the momentum flux is almost unaffected by an increase in internal energy. The variation in the specific heat ratio is therefore negligible in terms of jet dynamics in our simulations. Of course, we note that a softer equation of state leads to a lower sound speed and increases the interval of internal shocks. If the knots of AGN jets correspond to internal shocks, then the positions of the knots depend on the specific heat ratio.

A variation in the specific heat ratio is negligible in terms of dynamics, but the low specific heat ratio may decrease the electron temperature. The first reason is that the temperature jump condition depends on the specific heat ratio (see Eq. (A.1). The second reason is that more energy is required to heat electrons through Coulomb coupling when the specific heat ratio is small. Therefore, electrons and ions will more readily have different temperatures when we adopt the relativistic equation of state for electrons.

4.5.5 Observational implications

In radio galaxies such as Cygnus A, X-ray cavities are observed in the radio lobe around the jet (Wilson et al., 2006). These cavities can be explained by the low density, hot plasma in the cocoon (see Fig. 1(a)). Meanwhile, X-ray emission is enhanced in the shocked ICM surrounding the cocoon (see Fig. 4.1(h) and Fig. 4.5). Diffuse soft X-rays observed around the core of the AGN can be emitted from the cocoon plasma mixed with the ICM through Kelvin-Helmholtz instability. Our numerical results (Fig. 4.1(h)) indicate that the electron temperature in this region is around $T_{\rm e} = 10^8 - 10^9$K. This region can therefore enhance X-ray emission.

Observations of radio lobes indicate that the cocoon expands as the cocoon plasma flows back toward the galactic center. Therefore, the cocoon pressure should be higher than the ICM pressure. In a single temperature plasma, it is not consistent with the observations of both FRI/II jets which show that the electron pressure in the lobe is lower than the external pressure, i.e., the lobe is under-pressured (e.g., Belsole et al., 2007). Our numerical results resolve this problem because the ion pressure much exceeds the electron pressure in sub-relativistic AGN jets.

Electrons are in a relativistic regime in our simulations. Non-thermal particle acceleration for electrons is therefore efficient in both Fermi/diffusive shock acceleration and turbulent dissipation (Zhdankin et al., 2019; Sironi & Spitkovsky, 2011). The lobes are most prominently observed by the synchrotron emission of non-thermal electrons. It is thus not possible to directly obtain the thermal temperatures of both electrons and ions in radio observations. However, the efficiency of particle acceleration theoretically depends on the thermal energy of electrons and ions. Therefore, the population of non-thermal electrons depends on that of the thermal electrons. Groups have developed post-processing code for calculating non-thermal electron spectra from the results of MHD simulations (Vaidya et al., 2018; Winner et al., 2019). In order to obtain the realistic non-thermal electron spectra of AGN jets, it is necessary it use the thermal electron temperature obtained from two-temperature MHD simulations.

Diffuse thermal X-ray emissions have been detected in the radio lobes of a few sources, such as Fornax A and Centaurus A (Seta et al., 2013; Stawarz et al., 2013). The thermal emission comes from the mixing region between the radio lobe and the shocked ICM. In our work, two temperature plasma still exists in the mixing region (see Fig. 4.1(i) $z < 20$ kpc, $10 < r < 20$ kpc). Since the thermal Doppler broadening of spectral lines gives information about each the ions thermal velocity, future X-ray observations with high-resolution spectroscopy(e.g., the X-ray Imaging and Spectroscopy Mission, XRISM) will reveal the presence of the two-temperature plasma in cocoons of AGN jets.

4.6 Summary and conclusions

We performed two-dimensional and axisymmetric simulations of AGN jet propagation into a constant-density ICM to study the fraction of electron heating, which affects the electron temperature distribution.

- In axisymmetric jets, the energies of electrons and ions are decoupled at internal shocks. In particular, ions have about twice the internal energy of electrons in the downstream of the first internal shock. As in the one-dimensional case, the temperature ratio is described by Eq. (A.3) in the downstream of the terminal shock. However, post-shock electrons lose energy through adiabatic expansion in the multidimensional case and the temperature ratio may therefore fall below the

value predicted using Eq. (A.3) at low values of f_e. Furthermore, we found that the temperature of the injected jet does not affect the temperature in terminal regions when f_e is constant.

- The volume-weighted temperature of the cocoon decreases as the region expands. Coulomb coupling is weak in the cocoon because the electrons have reached relativistic temperatures, and the density is low. The time scale of energy transfer due to Coulomb collision is therefore about 10^{2-3} Myr at the end of simulations, and the electrons continue to be heated by ions in the cocoon. These results indicate the existence of two-temperature plasma in the X-ray cavity. In the shocked ICM, the ion thermal energy is converted to electron thermal energy efficiently, and ions and electrons achieve thermal equilibrium in 1 Myr. Moreover, mixing of the jet plasma and shocked ICM through KH instability at the interface could enhance soft X-ray emissions around the contact discontinuity between the cocoon and shocked ICM.

- We investigated the density dependence of the volume-weighted temperature evolution in the shocked ICM. The time scale of relaxation between electrons and ions is certainly extended for a lower-density model. However, the electron heating time scale strongly depends on the electron temperature, with a lower electron temperature resulting in a shorter heating time scale. Therefore, the lowest-density model, which has a density 100 times lower than that of the fiducial model, achieves thermal equilibrium by 10 Myr.

Our work indicates that two-temperature plasma exists in the X-ray cavity, and electrons and ions probably reach thermal equilibrium in the shocked ICM. However, the determination of the ion temperature is a challenge. XRISM observations could provide useful information on ion thermal energies from a line profile.

5 Three-dimensional structure of the two-temperature jets

5.1 Short introduction

We discussed the results of axisymmetric simulations with a constant fraction model for electron and proton heating in Chap. 4. These results proved us physical insight into the two-temperature jets. Meanwhile shocked-intracluster medium (ICM) reaches thermal equilibrium within a few Myr, the thermal protons, whose temperature is higher several ten times than electron temperature, support the expansion of cocoon. However, we have to deal with two key-physics to conduct realistic simulations.

Firstly, it is necessary to carry out three-dimensional simulations. As we summarized in Sect. 2.4, major magnetohydrodynamical (MHD) instabilities develop non-axisymmetric modes, namely Kelvin-Helmholtz modes, Rayleigh-Taylor modes, and current-driven kink modes. Thus, the non-linear evolution of these instabilities plays a significant role in the jet dynamics and large-scale morphology (e.g., Tchekhovskoy & Bromberg, 2016). In particular, the development of instabilities, cause the jet deceleration and/or the jet disruption, could directly link to the physical reasons of the Fanaroff-Riley (FR) distinction (see Sect. 2.1).

Secondly, we should implement the variable model for electron heating, instead of the constant model. The supersonic nature of jets triggers shocks and turbulence. However, our previous simulation in Chap. 4, we did not focus on the electron heating in turbulence. As we reported in Sect. 3.3, recent theoretical studies clarified the physical picture of electron heating in the collisonless turbulence (Kawazura et al., 2019, 2020). They provide us the variable model that describes the partition of heating energy between protons and electrons for the dissipation at the plasma kinetic scale. The heating fraction between

electron and proton in this model is not constant and is an increasing function of proton plasma-β, $\beta_{\rm p} \equiv 8\pi nkT_{\rm p}/B^2$. Our previous results indicated that the magnetic fields are accumulated, and the proton plasma-β decreased in the cocoon. In addition to this, the magnetic field can be amplified locally by non-axisymmetric motions. Therefore, the turbulence would be the dominant heating source for thermal electrons, compared with shock heating.

Jet magnetization parameters, namely jet Alfvén Mach number $\mathcal{M}_{\rm A}$ and plasma-β $\beta_{\rm gas}$, are important for both electron heating and dynamical evolution. However, none of the studies have considered two-temperature plasma, and explore the effect of different jet magnetization on the electron heating with the development of MHD instabilities. Thus, the purpose of this chapter is to examine the effect of the variable model for electron heating in turbulence on the distribution of electron temperature in a varying range of the jet magnetization parameters. Also, we clarify whether shocks or turbulence are the dominant heating source for electrons. Finally, the aim of our simulations is to explore that the jet magnetization parameters impart the development of various MHD instabilities. To achieve these purposes, we perform a series of three-dimensional two-temperature MHD simulations of the propagation of a sub-relativistic jet.

5.2 Numerical Method

5.2.1 Numerical integration

In Chap. 4, we assume that electron entropy obey a non-relativistic entropy formula, $s = k \ln p^{\gamma} \rho^{-1}$, for simplicity. However, when the plasma temperature beyond a relativistic temperature ($kT \gg mc^2$), this simplification is incorrect. In the context of jet, electrons are widely distributed from non-relativistic to relativistic temperature. However, we find that some numerical noise are contaminated in the previous integration method. Thus, we modify the numerical integration method to implement a relativistic thermodynamics phenomena.

We follow the energy evolution for electrons in addition the total energy in the previous integration method. In the modified method, following Sadowski et al. (2017), we follow the energy evolution for electrons and protons independently. The total gas (summed

electrons and protons) are evolved by the MHD equations in conservation form:

$$\frac{\partial \boldsymbol{U}}{\partial t} + \nabla \cdot \boldsymbol{F} = \boldsymbol{S}, \tag{5.1}$$

$$\boldsymbol{U} = \begin{pmatrix} n \\ m_{\rm p} n \boldsymbol{v} \\ \boldsymbol{B} \\ E \end{pmatrix}, \tag{5.2}$$

$$\boldsymbol{F} = \begin{pmatrix} n\boldsymbol{v} \\ m_{\rm i} n \boldsymbol{v}\boldsymbol{v} + p_{\rm T}\boldsymbol{I} - \frac{1}{4\pi}\boldsymbol{B}\boldsymbol{B} \\ \boldsymbol{v}\boldsymbol{B} - \boldsymbol{B}\boldsymbol{v} \\ (E + p_{\rm T})\boldsymbol{v} - \frac{1}{4\pi}\boldsymbol{B}(\boldsymbol{v}\cdot\boldsymbol{B}) \end{pmatrix}, \tag{5.3}$$

$$\boldsymbol{S} = \begin{pmatrix} 0 \\ 0 \\ 0 \\ -q_{\rm rad} \end{pmatrix}, \tag{5.4}$$

where $q_{\rm rad}$ is the radiative energy loss rate. In this work, we assume the radiation process as bremsstrahlung emission. The total energy E and total pressure $p_{\rm T}$ are respectively

$$E = \frac{p_{\rm p}}{\gamma_{\rm p} - 1} + \frac{p_{\rm e}}{\gamma_{\rm e} - 1} + \frac{\rho v^2}{2} + \frac{B^2}{2} = \frac{p_{\rm gas}}{\gamma_{\rm gas}(T_{\rm e}, T_{\rm i}) - 1} + \frac{\rho v^2}{2} + \frac{B^2}{2}, \tag{5.5}$$

$$p_{\rm T} = p_{\rm p} + p_{\rm e} + \frac{B^2}{2} = p_{\rm gas} + \frac{B^2}{2}, \tag{5.6}$$

where $p_{\rm gas} = p_{\rm p} + p_{\rm e}$ is the gas pressure, which is summed the proton pressure $p_{\rm p}$ and electron pressure $p_{\rm e}$. Note that a adiabatic index of gas $\gamma_{\rm gas}$ and the radiative energy loss rate $q_{\rm rad}$ are functions of electron and proton temperature. In addition to solving MHD equations, we solve the entropy equations of the two species to obtain each temperatures.

The entropy equations of electrons and protons can be written by:

$$T_{\rm e}\frac{d(n_{\rm e}s_{\rm e})}{dt} = f_{\rm e}q_{\rm heat} + q_{\rm ie} - q_{\rm rad}, \tag{5.7}$$

$$T_{\rm p}\frac{d(n_{\rm p}s_{\rm p})}{dt} = (1-f_{\rm e})q_{\rm heat} - q_{\rm ie},, \tag{5.8}$$

where $q_{\rm ie}$, $f_{\rm e}$, and $q_{\rm heat}$ are the energy transfer ratio via the Coulomb coupling, the fraction of the electron heating, and the dissipation heating rate, respectively.

We concern trans-relativistic regime for electrons, and use the following approximate entropy formula derived by Sadowski et al. (2017) in Appendix A:

$$s_{\rm e} = k\ln\left[\frac{{\theta_{\rm e}}^{3/2}(\theta_{\rm e}+\frac{2}{5})^{3/2}}{\rho_{\rm e}}\right], \tag{5.9}$$

where $\theta_{\rm e}$ is the dimensionless temperature. The adiabatic index for electrons is calculated as follows:

$$\gamma_{\rm e}(\theta_{\rm e}) = \frac{10+20\theta_{\rm e}}{6+15\theta_{\rm e}}. \tag{5.10}$$

On the other hand, protons are non-relativistic in this simulation. Thus, we use the non-relativistic entropy formula for protons:

$$s_{\rm p} = k\ln {p_{\rm p}{\rho_{\rm p}}^{-\gamma_{\rm p}}}, \tag{5.11}$$

where $\gamma_{\rm p} = 5/3$. The thermal energy of protons, electron, and gas are as follows:

$$u_{\rm p} = \frac{p_{\rm p}}{\gamma_{\rm p}-1}, \quad u_{\rm e} = \frac{p_{\rm e}}{\gamma_{\rm e}(T_{\rm e})-1}, \quad u_{\rm gas} = u_{\rm p}+u_{\rm e} = \frac{p_{\rm gas}}{\gamma_{\rm gas}(T_{\rm p},T_{\rm e})-1}. \tag{5.12}$$

From the relationship between gas pressure and gas thermal energy, the effective adiabatic index for the gas can be calculated as (Ressler et al., 2015)

$$\gamma_{\rm gas}(T_{\rm p},T_{\rm e}) = 1+(\gamma_{\rm e}-1)(\gamma_{\rm p}-1)\frac{1+T_{\rm p}/T_{\rm e}}{(\gamma_{\rm p}-1)+(\gamma_{\rm e}-1)T_{\rm p}/T_{\rm e}}. \tag{5.13}$$

In this simulation, we numerically solve Eq. (5.1). Steps of numerical interaction are as follows:

1. Calculate conservation variables from principle variables at the end of the previous time step, and the effective adiabatic index $\gamma_{\rm gas}$ is calculated by Eq. (5.13).

2. Adopt an operator split method ($\boldsymbol{S} = 0$ in Eq. (5.1)), and solve the conservative equation (see Matsumoto et al. (2019) for details).

3. Recalculate conservation variables, except for the gas thermal energy $u_{\rm gas}$, from principle variables. Note that updated electron and proton temperature are unknown, and thus we cannot calculate $u_{\rm gas}$ and $\gamma_{\rm gas}$ at this step.

4. Solve the entropy equations for electrons and protons (Eq. (5.7) and Eq. (5.8)). The detail procedure is described in the following section. Then, we calculate $u_{\rm gas}$ and $\gamma_{\rm gas}$ using updated electron and proton temperature.

5.2.2 Solve entropy equations

We describe the procedure of numerical integration for the entropy formula of electrons and protons. For simplicity, we describe method for the one-dimensional coordinate x. Firstly, to compute adiabatically evolution, we set the right-hand side of Eq. (5.7) and Eq. (5.8). Solve these equations by the finite-difference method. Let x_i be the cell center of a uniform grid, Δx is the cell width. Also, time describes $t^n = n\Delta t$, where Δt is the time step. We adopt 3rd order TVD-Runge–kutta schemes, and then the finite-difference equations are as follows:

$$(\rho s)_i^{(1)} = (\rho s)_i^n - \frac{\Delta t}{\Delta x}[(\rho s v_x)_{i+1/2}^n - (\rho s v_x)_{i-1/2}^n], \tag{5.14}$$

$$(\rho s)_i^{(2)} = \frac{3}{4}(\rho s)_i^n + \frac{1}{4}\left[(\rho s)_i^{(1)} - \frac{\Delta t}{\Delta x}[(\rho s v_x)_{i+1/2}^{(1)} - (\rho s v_x)_{i-1/2}^{(1)}]\right], \tag{5.15}$$

$$(\rho s)_i^{n+1} = \frac{1}{3}(\rho s)_i^n + \frac{2}{3}\left[(\rho s)_i^{(2)} - \frac{\Delta t}{\Delta x}[(\rho s v_x)_{i+1/2}^{(2)} - (\rho s v_x)_{i-1/2}^{(2)}]\right], \tag{5.16}$$

where (1) and (2) denote each number of sub-time steps of TVD-Runge–kutta scheme. Note that the entropy formulas for electrons and protons are the same form, and we do not distinguish between them.

Following Sadowski et al. (2017), we arrange Eq. (5.14) - Eq. (5.16) as follows:

$$s_i^{(1)} = \frac{\rho_i^n}{\rho_i^{(1)}} s_i^n - \frac{\frac{\Delta t}{\Delta x}(\rho v_x)_{i+1/2}^n}{\rho_i^{(1)}} s_{i+1/2}^n + \frac{\frac{\Delta t}{\Delta x}(\rho v_x)_{i-1/2}^n}{\rho_i^{(1)}} s_{i-1/2}^n \tag{5.17}$$

$$= f_i^{(1)} s_i^n + f_{i+1/2}^{(1)} s_{i+1/2}^n + f_{i-1/2}^{(1)} s_{i-1/2}^n. \tag{5.18}$$

$$s_i^{(2)} = \frac{3}{4}\frac{\rho_i^n}{\rho_i^{(2)}} s_i^n + \frac{1}{4}\frac{\rho_i^{(1)}}{\rho_i^{(2)}} s_i^{(1)} - \frac{\frac{1}{4}\frac{\Delta t}{\Delta x}(\rho v_x)_{i+1/2}^{(1)}}{\rho_i^{(2)}} s_{i+1/2}^{(1)} + \frac{\frac{1}{4}\frac{\Delta t}{\Delta x}(\rho v_x)_{i-1/2}^{(1)}}{\rho_i^{(2)}} s_{i-1/2}^{(1)} \tag{5.19}$$

$$= f_i'^{(2)} s_i^n + f_i^{(2)} s_i^{(1)} + f_{i+1/2}^{(2)} s_{i+1/2}^{(1)} + f_{i-1/2}^{(2)} s_{i-1/2}^{(1)}. \tag{5.20}$$

$$s_i^{(n+1)} = \frac{1}{3}\frac{\rho_i^n}{\rho_i^{n+1}}s_i^n + \frac{2}{3}\frac{\rho_i^{(2)}}{\rho_i^{n+1}}s_i^{(2)} - \frac{\frac{2}{3}\frac{\Delta t}{\Delta x}(\rho v_x)_{i+1/2}^{(2)}}{\rho_i^{n+1}}s_{i+1/2}^{(2)} + \frac{\frac{2}{3}\frac{\Delta t}{\Delta x}(\rho v_x)_{i-1/2}^{(2)}}{\rho_i^{n+1}}s_{i-1/2}^{(2)} \quad (5.21)$$

$$= f_i'^{n+1}s_i^n + f_i^{n+1}s_i^{(2)} + f_{i+1/2}^{n+1}s_{i+1/2}^{(2)} + f_{i-1/2}^{n+1}s_{i-1/2}^{(2)}, \quad (5.22)$$

where f and f' are the fractions of the final state represented by the three contributing grids of gas. When two individual gases are mixed a constant volume, the total energy to be the sum of the initial energies of the gases. In contrast, the total entropy is not to be that. In other words, the finite-volume methods in Eq. (5.17) - Eq. (5.21) are incorrect. But, to overcome this problem, we must treat the dynamics of each gas individually. In this work, following Sadowski et al. (2017), we solve Eq. (5.17) - Eq. (5.21) by replace the entropy with the thermal energy. The relationship between entropy and internal energy are known in Eq. (5.17), Eq. (5.21), Eq. (5.10), and Eq. (5.12). Thus, the thermal energy is a function of density and entropy:

$$u_{i,i\pm1/2}^n = u(s_{i,i\pm1/2}^n, \rho_i^{(1)}), \quad u_{i,i\pm1/2}^{(1)} = u(s_{i,i\pm1/2}^{(1)}, \quad \rho_i^{(2)}), \quad u_{i,i\pm1/2}^{(2)} = u(s_{i,i\pm1/2}^{(2)}, \rho_i^{n+1}). \quad (5.23)$$

Here, to safe, we use upwind values of the entropy, $s_{i+1/2}^n = \text{Upwindow}\left(s^n{}_{\text{i}}, s_{i+1}^n\right)$ and $s_{i-1/2}^n = \text{Upwindow}\,(s^n{}_{\text{i}-1}, s_i^n)$. From the above calculation, we can obtain the thermal energy of electron and proton that evolve under the adiabatic process, $u_{\text{e,ad}}$ and $u_{\text{p,ad}}$. Then, we calculate the dissipation heating at each grids as:

$$Q_{\text{heat}}^{(1),(2),n+1} = u_{\text{gas}}^{(1),(2),n+1} - (u_{\text{e,ad}}^{(1),(2),n+1} + u_{\text{i,ad}}^{(1),(2),n+1}), \quad (5.24)$$

where $dQ_{\text{heat}}/dt = q_{\text{heat}}$. Also, if necessary, the fraction of the electron heating, f_{e}, is calculated by using MHD quantities. Finally, dividing the dissipation heating into electrons and protons, the thermal energies of electron and proton are updated as follows:

$$u_{\text{e}}^{(1),(2),n+1} = u_{\text{e,ad}}^{(1),(2),n+1} + f_{\text{e}}^{(1),(2),n+1}Q_{\text{heat}}^{(1),(2),n+1}, \quad (5.25)$$

$$u_{\text{p}}^{(1),(2),n+1} = u_{\text{p,ad}}^{(1),(2),n+1} + (1 - f_{\text{e}})Q_{\text{heat}}^{(1),(2),n+1}. \quad (5.26)$$

The source term, namely energy transfer via Coulomb coupling and radiative cooling, is updated implicitly by adopting the Newton–Raphson iteration at last sub-step of the TVD-Runge–kutta scheme.

5.2.3 Electron heating model

We consider two sub-grids models for the fraction of electron heating f_{e}. One model represents the turbulence heating $f_{\text{e,turb}}$, and another model represents the shock heating

$f_{\rm e,shock}$. Therefore, $f_{\rm e}$ is determined by plasma properties at each simulation grid. First of all, we identify a shock zone by shock-finding method which is based on Ryu et al. (2003) and Schaal & Springel (2015) (see detail in Sect. A.2). The fraction of shock heating are adopted only in shock zone, and other region is adopted by the fraction of turbulence heating ,i.e.,

$$f_{\rm e}(x,y,z) = \begin{cases} f_{\rm e,shock} & \text{(for shock zone)} \\ f_{\rm e,turb} & \text{(for otherwise)} \end{cases} \tag{5.27}$$

Note that an amount of dissipation energy is small in the region of laminar flow and hence the heating fraction of turbulence heating spontaneously works in turbulence zone.

Shock heating

We use a constant model of electron heating fraction for shock zone, $f_{\rm e,shock} = 0.05$. This parameter value is well described the observation data in the solar system and supernova remnants shocks (Vink et al., 2015). Furthermore, some theoretical simulations, based on PIC simulation, indicate that electrons irreversible heat up but proton are primarily heated at collisionless shocks.

Turbulence heating

We use the fitting function for electron-to-proton heating rates of MHD turbulence (Kawazura et al., 2020):

$$\frac{Q_{\rm p}}{Q_{\rm e}} = \frac{35}{1+(\beta_{\rm i}/15)^{-1.4}{\rm e}^{-0.1T_{\rm e}/T_{\rm i}}} + \frac{P_{\rm compr}}{P_{\rm AW}}, \tag{5.28}$$

where $P_{\rm compr}$ and $P_{\rm AW}$ are the compressive energy injection and the Alfvénic energy injection, respectively. Therefore, the fraction of electron heating $f_{\rm e}$ is defined by:

$$f_{\rm e,turb} = \frac{Q_{\rm e}}{Q_{\rm p}+Q_{\rm e}}. \tag{5.29}$$

We assume purely Alfvénic turbulence (i.e., $P_{\rm compr}/P_{\rm AW} \to 0$). Note that this assumption overestimates the amount of electron heating. This heating model is a weak dependence of the temperature ratio $T_{\rm e}/T_{\rm p}$ but a strong dependence of proton plasma beta $\beta_{\rm p}$. In the case of $\beta_{\rm p} < 1$, the turbulent heating goes to electrons, and vice versa.

5.2.4 Bremsstrahlung radiation cooling

Bremsstrahlung cooling rate per unit volume for relativistic plasma is (Svensson, 1982)

$$q_{\rm brems}(\theta_{\rm e}, n) = n^2 \sigma_{\rm T} c \alpha_{\rm f} m_{\rm e} c^2 [F_{\rm ei}(\theta_{\rm e}) + F_{\rm ee}(\theta_{\rm e})], \tag{5.30}$$

where $\alpha_{\rm f}$ and $\sigma_{\rm T}$ are fine-structure constant, Thomson cross section, respectively. In above equation, $F_{\rm ei}$, and $F_{\rm ee}$ are the dimensionless radiation rate due to proton-electron collisions and electron-electron collisions, respectively. The approximation formula of $F_{\rm ei}$, and $F_{\rm ee}$ are respectively

$$F_{\rm ei}(\theta_{\rm e}) = \begin{cases} 4.0 \left(\frac{2}{\pi^3}\right)^{1/2} {\theta_{\rm e}}^{1/2} (1 + 1.78 {\theta_{\rm e}}^{1.34}) & \text{for } (\theta_{\rm e} < 1) \\ \frac{9.0\theta_{\rm e}}{2\pi} \left[\ln\left(2\eta_{\rm E}\theta_{\rm e} + 0.42\right) + \frac{3}{2}\right] & \text{for } (\theta_{\rm e} > 1) \end{cases}, \tag{5.31}$$

$$F_{\rm ee}(\theta_{\rm e}) = \begin{cases} \frac{20}{9\pi^{1/2}}(44 - 3\pi^2){\theta_{\rm e}}^2 \left(1 + 1.1\theta_{\rm e} + {\theta_{\rm e}}^2 - 1.25{\theta_{\rm e}}^{2.5}\right) & \text{for } (\theta_{\rm e} < 1) \\ 24\theta_{\rm e}\left[\ln 2\eta_{\rm E}\theta_{\rm e} + \frac{5}{4}\right] & \text{for } (\theta_{\rm e} < 1) \end{cases}. \tag{5.32}$$

Here, $\eta_{\rm E} = \exp(-\gamma_{\rm E})$ and $\gamma_{\rm E} \approx 0.5772$ is Euler's number.

5.3 Simulation setup

We carried out the two-temperature 3D MHD simulations on Cartesian coordinate with the z-axis pointing along the jet direction. The computational domain is $x \in (-L_x/2, L_x/2)$, $y \in (-L_y/2, L_y/2)$, and $z \in (0, L_z)$, where L_x, L_y, and L_z are the length of computational domain. The computational domain is covered by $N_x \times N_y \times N_z$ uniform mesh grids whose size is $\Delta x = \Delta y = \Delta z = 0.1$ kpc. Grids number and the length of computational domain are given in Tab. 5.1. We permit the backflow to escape from the boundary at $z = 0$. Thus, the absorbing boundary condition is applied at $xy-$plane of $z = 0$. Other boundaries are imposed on the free-boundary condition.

5.3.1 Initial condition

To study the interaction between jets and the ICM, we set up initial surrounding ICM in the form of β profile (King, 1962). Our cluster model is roughly consistent with the

environment of Cygnus A from *Chandra* X-ray data (Wilson et al., 2006). The density profile of ICM is

$$n(r) = \frac{n_0}{[1 + (r/r_{\rm c})^2]^{3\beta'/2}}, \tag{5.33}$$

where $r = \sqrt{x^2 + y^2 + z^2}$, n_0, $r_{\rm c}$ and β' are the radius, the core density, the core radius, and the parameter for the ratio of the specific energy in the galaxies to the specific thermal energy in the ICM, respectively. We set $\beta' = 0.5$, $r_{\rm c} = 20$ kpc, and $n_0 = 0.05$ cm^{-3}. We also assume our atmosphere is initially isothermal with temperature $kT_{\rm p} = kT_{\rm e} = 5$ keV. We employ the uniform magnetic field $B_{\rm ICM}$ that is parallel to the z-axis and $B_{\rm ICM} = 0.44$ μG. The blue lines of Fig. 5.1 show the initial density (the top panel) and pressure (the bottom panel), respectively.

5.3.2 Jet model

Focusing on the effect of jet magnetization on electron heating and jet stability, we carried out simulations with different magnetic field strength. We model magnetized supersonic sub-relativistic flows to consistent with the outburst energy of Cygnus A jets, $0.6 - 0.8 \times 10^{46}$ erg s^{-1} (Bîrzan et al., 2004; Snios et al., 2018). The injected jet power can be written as follows:

$$L_{\rm jet} = L_{\rm kin} + L_{\rm th} + L_{\rm mag} = \pi {r_{\rm jet}}^2 v_{\rm jet} \left(\frac{1}{2} m_{\rm p} n_{\rm jet} v_{\rm jet} + \frac{n_{\rm jet} k T_{\rm p,jet}}{\gamma_{\rm p} - 1} + \frac{n_{\rm jet} k T_{\rm e,jet}}{\gamma_{\rm e} - 1} + \frac{{B^2}_{\rm jet}}{8\pi} \right). \tag{5.34}$$

We set the kinetic power $L_{\rm kin} = 5.5 \times 10^{45}$ erg s^{-1} and the thermal power $L_{\rm th} = 4.4 \times 10^{44}$ erg s^{-1}, respectively.

To generate the jet beams, we injected supersonic and magnetized flows inside a constant cylindrical nozzle at the origin. The radius and length of the nozzle are 1 kpc and 1.2 kpc, respectively. Although it is hard to determine the real flow radius of jets by observations, radio observation indicates that the radio full width at half maximum radius of Cygnus A is 0.1 to 1.0 kpc at 1 kpc from the central engine (Nakahara et al., 2019). We assume that the jet temperature and the velocity are $T_{\rm p} = T_{\rm e} = 10^{10}$ K and $v_{\rm jet} = 0.3c$, respectively. Thus, the internal sonic Mach number is $\mathcal{M} = 6.2$. Our jet models satisfy a condition that the thermal pressure ratio between the jet and the ICM in

Table 5.1: Numerical Models

Model	$\beta_{\rm gas,jet}$	$\mathcal{M}_{\rm A}$	$B_{\rm jet}$ [μG]	$L_x \times L_y \times L_z$ [kpc]	$N_x \times N_y \times N_z$
A	1	4.9	138	$64 \times 65 \times 96$	$640 \times 650 \times 960$
B	5	11	62	$64 \times 64 \times 96$	$640 \times 640 \times 960$
C	100	49	14	$64 \times 65 \times 96$	$640 \times 650 \times 960$

Table 5.2: Jets and ICM common setup parameters

Jet speed	$v_{\rm jet}$	$0.3c$
Jet gas temperature	$T_{\rm g,jet}$	10^{10} [K]
Jet Kinetic energy	$L_{\rm kin}$	5.0×10^{45} [erg s^{-1}]
Jet thermal energy	$L_{\rm th}$	4.4×10^{44} [erg s^{-1}]
Jet radius	$r_{\rm jet}$	1 [kpc]
Jet Sonic Mach Number	$\mathcal{M}_{\rm jet}$	6.2
ICM temperature	$T_{\rm ICM}$	5 [KeV]
Core density	n_0	5×10^{-2} cm^{-3}
Core radius	$r_{\rm c}$	20 [kpc]
Core parameter	β'	0.5
ICM magnetic field	$B_{\rm z,ICM}$	0.44 [μG]

the launching region is unity. In Fig. 5.1, the blue dots denote the density and pressure in the jet injection region, respectively. A small-amplitude (1 percent) random pressure perturbation for the injection flow is adapted to model non-axisymmetric features. We list common parameters for ICM and jets in Tab. 5.2.

The jets have a purely toroidal magnetic field $B_\phi = B_{\rm jet} \sin^4(2\pi r/r_{\rm jet})$. As shown in Tab. 5.1, Models A, B, and C have different values of gas plasma $\beta_{\rm gas}$ equal to 1, 5, 100, respectively. That's plasma $\beta_{\rm gas}$ values are respectively corresponded to $B_{\rm jet} = 138, 62, 14$ μG for models A, B, and C. Our models are matter-dominated jets, thus in all models, the kinetic energy of jets exceeds the Poynting flux energy.

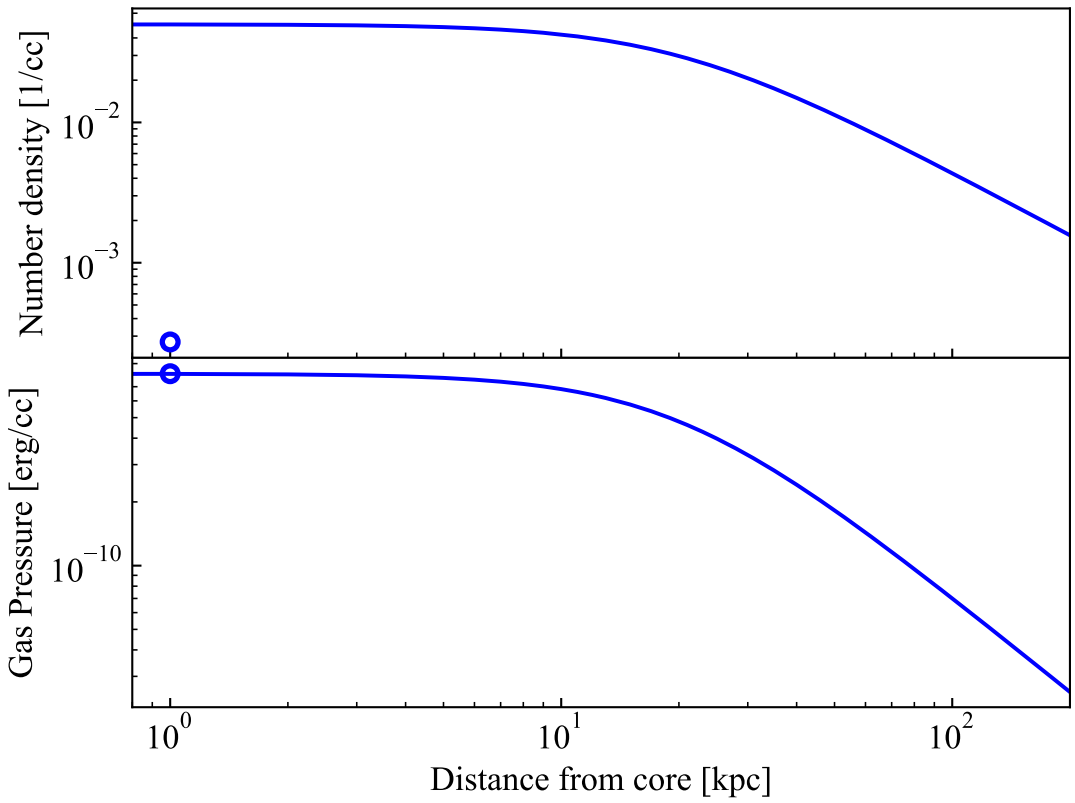

Fig. 5.1: **Top**: Number density profile of initial ICM as a function of radius. The blue dot represents the jets number density. **Bottom**: Same as the top panel, but for gas pressure. The initial gas temperature of the ICM is 5 KeV over the entire simulation domain.

5.4 Results

We have conducted simulations with the different magnetic energy to investigate the effect of jet dynamics and electron heating. We focus on the effect of the magnetic field strength on the dynamics of jets. The strength of the magnetic field affects the development of instability such as kink, Kelvin-Helmholtz, and Rayleigh-Taylor modes. Thus, we especially study to understand the relationship between the turbulent field in the cocoon and the development of instability in the beam. The electron heating model for turbulence is the function of plasma-$\beta_{\rm p}$, and hence magnetization strong affect the electron temperature distributions.

5.4.1 Overall morphology

We show the density slices for model A, B, and C at the end of the simulation time (t = 9.52, 9.94, and 13.02 Myr) in Fig. 5.2. The basic structures of jets for three-dimensional simulations are the same as that of asymmetric simulations (see Chap. 4). The shocked-ICM, which is compressed by the bowshock, and the low-density cavity (cocoon) are formed. We can see that the number density of the cocoons is $\sim 10^{-4}$ cm^{-3} ($0.001n_0$). The jet beam reaches a tip of jet in spite of suffering MHD instabilities (see red contours in Fig. 5.2), and a terminate shock is formed at the end of jet for all models. The shapes of bowshock are affected by the bending motion of the jets for model A and B. Strong pressure waves are generated at the termination of the beam, and thus these waves push up the bowshock. We clearly find that although the bowshock of model A is non-axisymmetric although that of model C is axisymmetric, that of model A is non-axisymmetric.

Figure 5.3 shows slice (in the $x - z$ plane) of the distribution of the gas pressure for model B at t = 9.94 Myr. The Kelvin-Helmholtz instability is developed at the contact discontinuity between the cocoon and the shocked-ICM. Supersonic turbulent motions developed this Kelvin-Helmholtz instability drive sound waves into shocked-ICM. These powerful sound waves carry jet energy from the cocoon into shocked-ICM (Bambic & Reynolds, 2019). Higher-magnetized model form longer-wavelength mode of Kelvin-Helmholtz instability and hence drive powerful, long-wavelength sound waves into shocked-ICM.

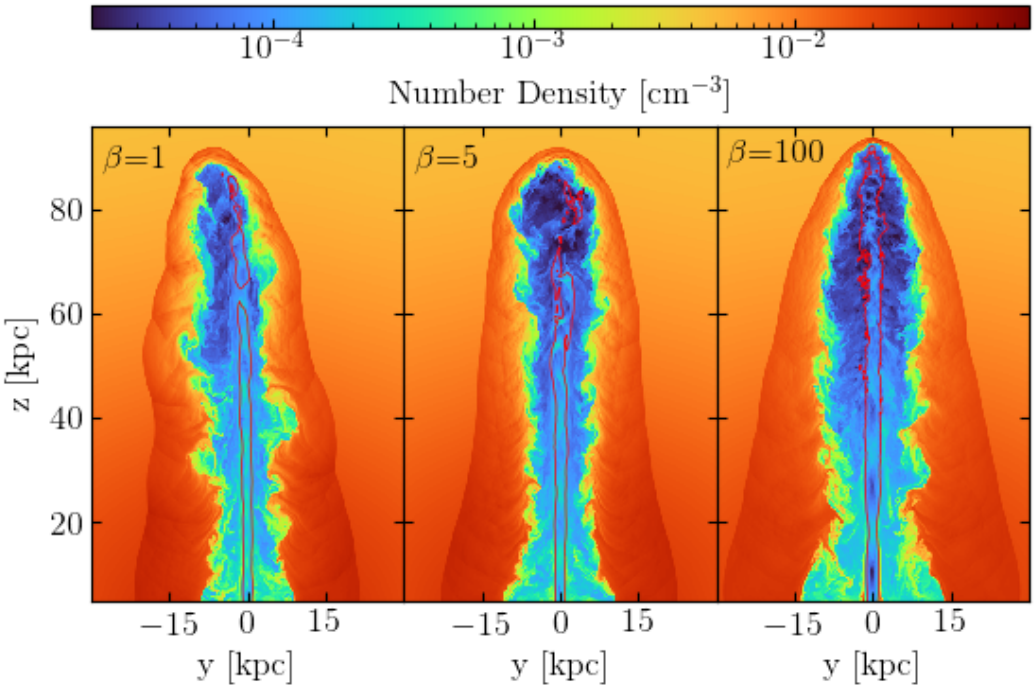

Fig. 5.2: Slices (in the $y-z$ plane) of the distribution of the number density for model A, B, and C at $t = 9.52$, 9.94, and 13.02 Myr, respectively. The red lines represent contours of the z-component of velocity $v_z = 0.5v_{\rm jet}$ $(0.15c)$.

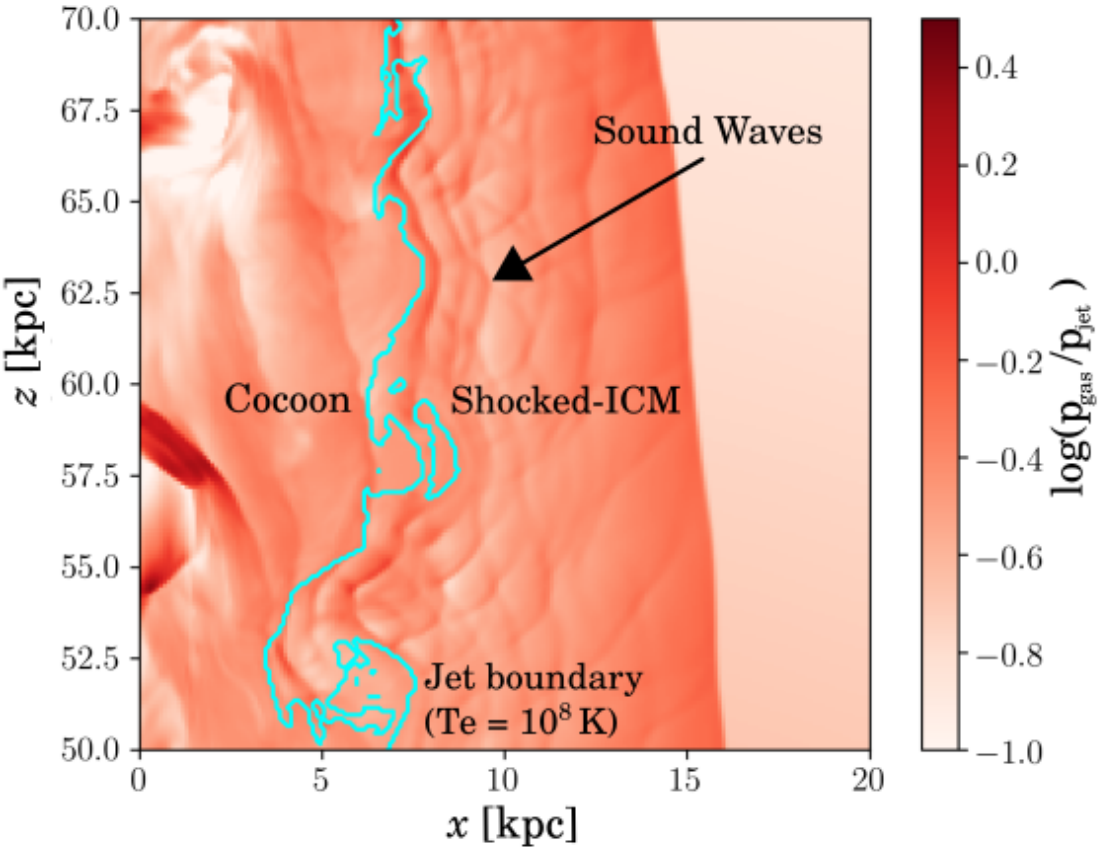

Fig. 5.3: Slice (in the $x-z$ plane) of the distribution of the gas pressure for model B at $t = 9.94$ Myr. The solid cyan contour denotes the jet boundary where $T_{\rm e} = 10^8$ K. Supersonic turbulent motions of the cocoon (jet gas) drive sound waves into shocked-ICM.

5.4.2 Beam stability

In the top and middle panels of in Fig. 5.4, we plot the time evolution of the bowshock tip position and the propagation speed of bowshock for model A, B, and C. The propagation speed given by one-dimensional analysis is obtained by Eq. (2.22). Here, we extend this equation to adopt for the case of the ICM of $\beta-$model case,

$$v_{\rm head}(z) = \frac{\sqrt{An_{\rm jet}/n_{\rm ICM}(z)}}{1+\sqrt{An_{\rm jet}/n_{\rm ICM}(z)}} v_{\rm jet}, \tag{5.35}$$

where A is the cross section ratio between beam and jet head. We obtain analytic solution by solving above equation while $A = 1$ and $v_{\rm jet} = 0.3c$. We plot analytic solutions in the top and middle panels of Fig. 5.4 (gray solid). The propagation velocity for analytic solutions have a constant value while jets propagate within the core ($r < r_{\rm c}$). After the jet passes through the core, the decreasing of ICM density triggers the acceleration of the jet because the ram pressure drops rapidly. We can see that the propagation velocity of all models has a similar tendency to the analytic solution, i.e., the jets accelerate after passing through the core. Meanwhile, the jets are slowing down while it propagates over long distances. In particular, the jet of model B is suffered strong deceleration after 7.5 Myr.

The propagation speed is related to the head size A because the large cross section of the head is exposed to a large amount of ram pressure. Thus, we investigated the time evolution of the head size (see the bottom panel of Fig. 5.4). The head size are defined as $\pi {r_{\rm head}}^2$ where $r_{\rm head} = 0.5(\Delta x_{\rm bow} + \Delta y_{\rm bow})$ is the bowshock radius. We measure $\Delta y_{\rm bow}$ and $\Delta x_{\rm bow}$ at 1 kpc below the tip of the jet. There is an anti-correlation between the propagation speeds and the head size. A high-magnetized jet has a small head because the magnetic hoop stress, B_ϕ^2/r, suppress the radial expansion motion of the backflow. The jet of model B are suffered strong deceleration after $t = 7.5$ Myr, and we clearly find that the head size drastically increases at the same time. The trigger that increases the head size is the development of non-axisymmetric, kink mode.

The characteristic timescale of development of external kink mode is corresponded to the Alfvén crossing time in the beam (Moll et al., 2008; Mizuno et al., 2009),

$$\tau_{\rm kink} \sim \frac{2\pi r_{\rm jet}}{v_{{\rm A},\phi}}, \tag{5.36}$$

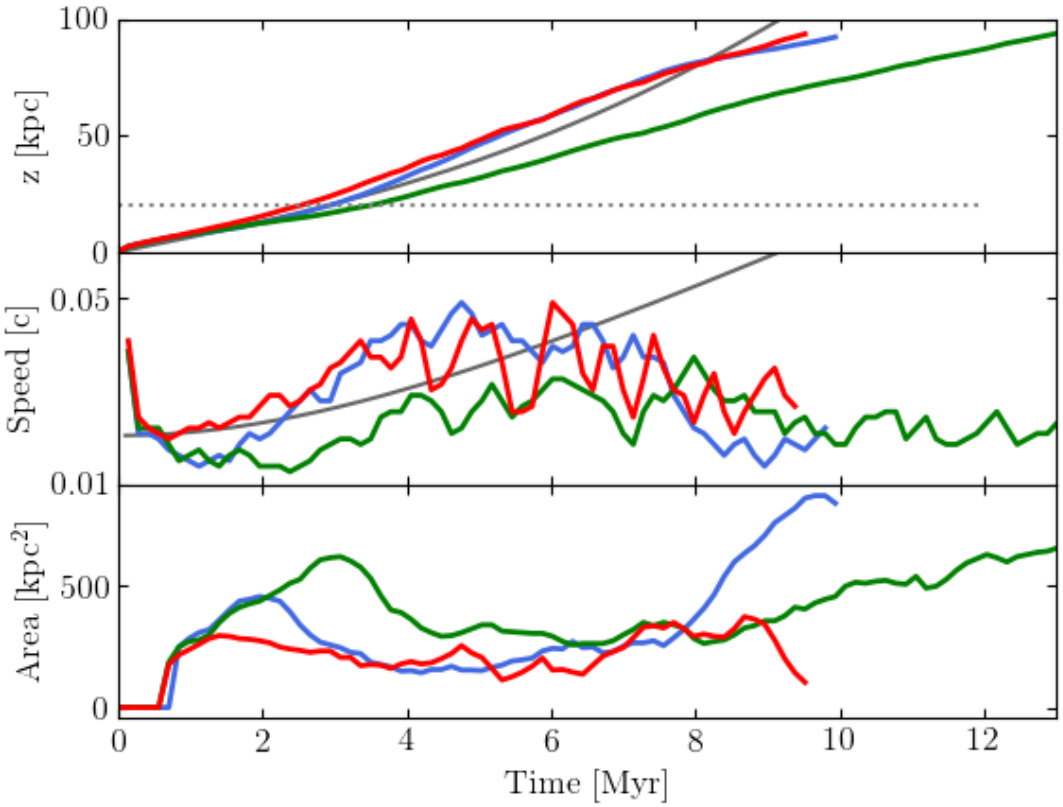

Fig. 5.4: Time evolution of the bowshock tip position (**top**), the propagation speed of bowshock (**middle**), and the jet head area (**bottom**). Red lines, blue lines, and green lines are respectively for model A, B, and C. The gray solid lines are analytic solution of Eq. (5.35). The gray dotted line of top panel indicates core radius ($r_c = 20$ kpc).

where $v_{A,\phi}$ is the azimuthal Alfvén velocity. A fluid element in the beam has roughly a constant velocity, $v_{\rm jet}$. We verify that the bulk beam velocity slightly changes but roughly keep an injection velocity. Therefore, the kink mode develop after the jets propagate to the distance $l_{\rm kink} \sim v_{\rm jet}\tau_{\rm kink}$. For model A and B, the distance $l_{\rm kink} \sim 40,\ 70$ kpc are respectively within the simulation domain. In particular, the jet of model A has precession after $t \sim 5$ Myr. Meanwhile, $l_{\rm kink}$ is larger than the length of the simulation domain and hence the model C jet is not expected to develop kink mode in simulation time.

Fig. 5.5 shows two-dimensional distribution maps of the beam barycenter $R_{\rm G}$, which is described as distance from origin, as function of time for each model. We compute the beam barycenter as follows:

$$R_{\rm G}(t,z) = \frac{\int_x \int_y r v_{\rm z}(x,y,z,t) dxdydz}{\int_x \int_y v_{\rm z}(x,y,z,t) dxdydz} \quad \text{for} \quad v_{\rm z} > 0.8 v_{\rm jet}. \tag{5.37}$$

The large value of the barycenter indicates development of non-axisymmetric mode. We can see that $l_{\rm kink}$ is a good indicator of kink instability for both model A and B. After the jet propagates to the distance $l_{\rm kink}$, the barycenter is larger than 3 kpc for model A and B. For model B, the time at which the jet propagates to the distance $l_{\rm kink}$ is 7.5 Myr. This time corresponds to the time when the jet begins to decelerate. Thus, the non-axisymmetric mode developed by kink instability induces deceleration by increasing the size of the jet head. Meanwhile, since the jet does not suffer the kink mode the barycenter for model C is within 1 kpc in simulation time, i.e., the jet propagates straight.

Magnetic fields also play an important role in the suppression of Rayleigh-Taylor instability. In Fig. 5.6, we present the cross-section of the z-component velocity in the x-y plane at 70 kpc for model A, B, and C. We can see that kink instability for model A and B bend the jet away from its initial launch axis ($x = y = 0$). Also, for model A and B, the jets clearly separate between beam flow and cocoon gas (backflow), i.e., the low mixing ratio between the beam and cocoon gas. Meanwhile, the low-magnetized jet of model C is not in the development of kink instability but also is in the development of Rayleigh-Taylor instability and Kelvin-Helmholtz instability. The onset condition of the Rayleigh-Taylor instability is given analytically by $\rho_{\rm jet} > \rho_{\rm cocoon}$ in hydrodynamic case. Note that Komissarov et al. (2019) found analytically that jets are stable for the Rayleigh-Taylor instability instability mode when $\mathcal{M}_A < 40$. Thus, the jet is in unstable mode of the Rayleigh-Taylor instability for model C (see Fig. 5.2 and Tab. 5.1). The

Rayleigh-Taylor mode forms a large cross-section, ~ 10 kpc, of positive velocity field and finger-like structures. Owing to the high-mixing ratio between the beam and cocoon gas, the jet of model C is decelerated.

5.4.3 Magnetic fields in the cocoon

Figure 5.7 shows the slices of the x-direction component of the magnetic field for model A, B, and C, respectively. Since we inject purely toroidal fields in the beam, the toroidal fields are distributed in the cocoons. But, one can see that reversing fields exist in the cocoons. Also, reversing fields are dissipated in the cocoons of models A and B at $z < 40$ kpc. We will describe that the field structures in the beams in Sect. 5.5.1.

Since the magnetic tension suppresses the turbulence motions, the filaments in the cocoon of model A at $z > 40$ kpc, whose length is several kpc, are more stretched than that of model B. Due to shock compression, filaments are formed around the jet head, which have stronger magnetic fields than the injected magnetic fields. On the other hand, for the cocoon of model C, the small-scale turbulence is excited, and the typical size of the vortex is ~ 1 kpc.

To provide quantitative analysis, we show the probability distribution functions (PDFs) of an individual component of the field in Fig. 5.8. For model A, $|B_z|$ give large contributions for magnetic energy because the higher-magnetized filaments flow back to the downstream. Meanwhile, the PDF of model C shows a nearly isotropic distribution. This result seems to reflect the development of small-scale turbulence in the cocoon. We also can see that $|B_r|$ is energetically sub-dominant.

When individual components of field have a Gaussian distribution with zero mean, the field strength obey a Maxwell-Boltzmann function (MB) (Hardcastle, 2013):

$$P_{\rm MB}(B) = \sqrt{\frac{54}{\pi}} \frac{B^2}{{B_{\rm Maxwell}}^3} \exp\left[-\left(\frac{3}{2}\right)\left(\frac{B}{B_{\rm Maxwell}}\right)^2 \right]. \tag{5.38}$$

Here ${B^2}_{\rm Maxwell}/8\pi$ is a parameter meaning the mean magnetic field energy density. To compare with our results, ${B^2}_{\rm Maxwell}/8\pi$ is calculated by

$${B^2}_{\rm Maxwell} = \int_0^\infty B^2 P(B) dB, \tag{5.39}$$

where $P(B)$ is the PDFs of our simulation results. $B_{\rm Maxwell}$ are calculated as 21.59, 13.92, and 6.48 μG for model A, B, and C, respectively. Three plots of PDFs is border than their

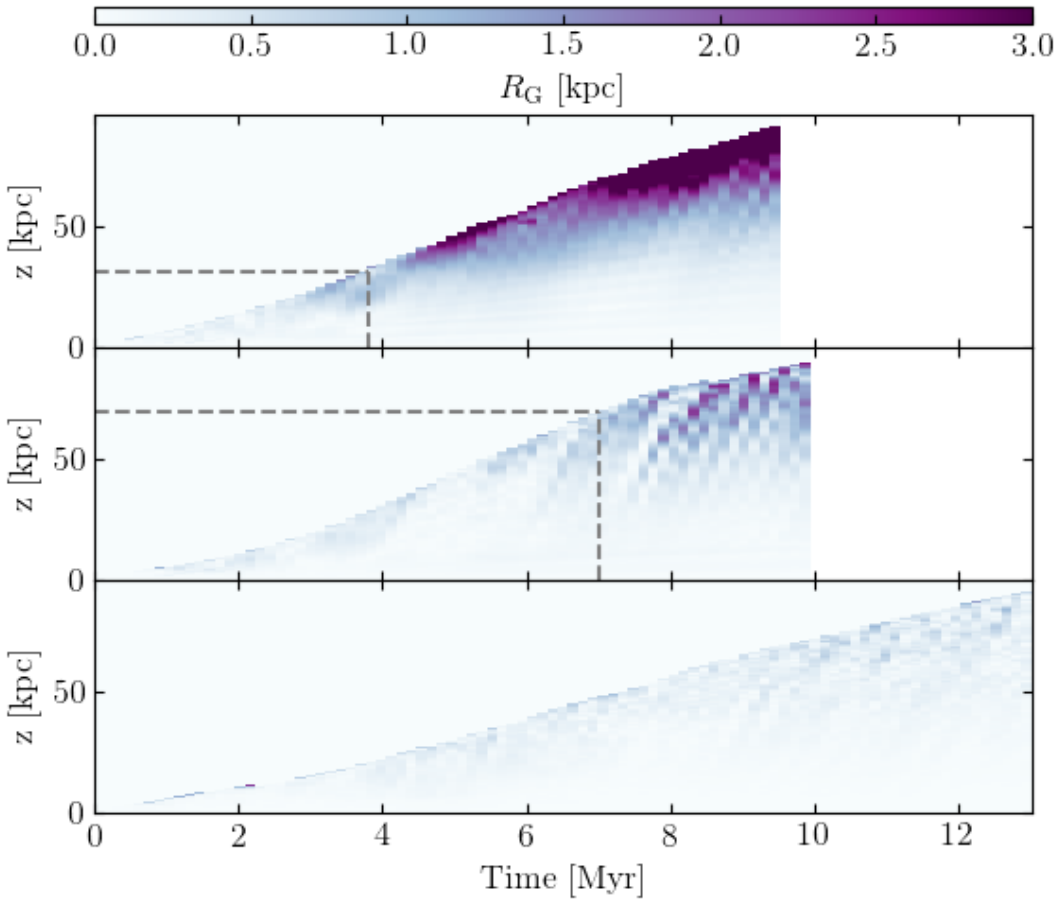

Fig. 5.5: Two-dimensional distribution maps of the beam barycenter R_G as a function of time for model A (**top**), B (**middle**), and C (**bottom**), respectively. The horizontal gray dashed lines are the distance l_{kink} for the development of the external kink model, and the vertical gray dashed lines are the time at which the jets propagate to the distance l_{kink}.

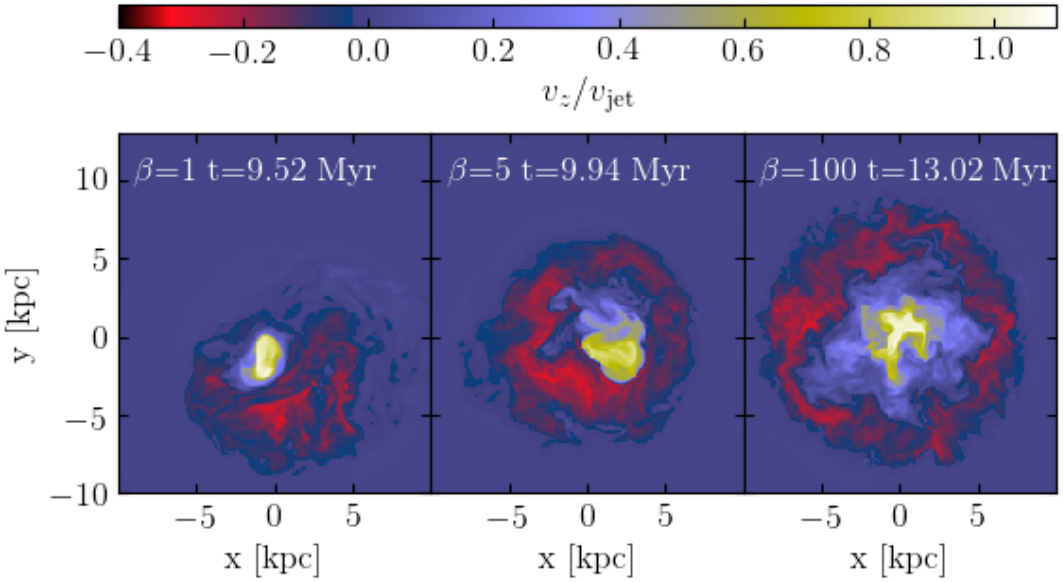

Fig. 5.6: Slices (in the $x-y$ plane at $z = 80$ kpc) of the distribution of the z-direction component of velocity for model A, B, and C, respectively.

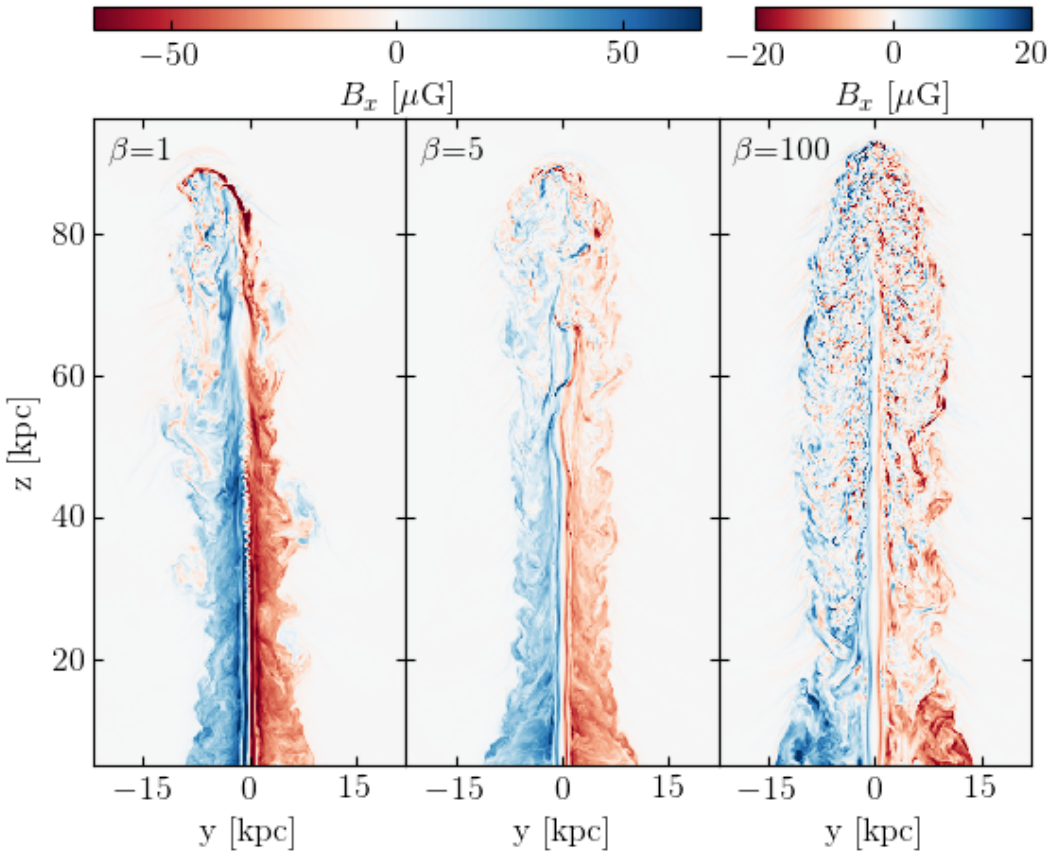

Fig. 5.7: Slices (in the $y-z$ plane) of the distribution of the x-direction component of magnetic field for model A, B, and C, respectively.

MBs. Notice that the strength of injected fields is 138, 62, and 14 μG for models A, B, and C, respectively. For all models, $B_{\rm maxwell}$ is lower than the injected fields because the fields value decrease with the adiabatic expansion and magnetic dissipation. In particular, a large amount of magnetic energy is dissipated for model A in the beam.

5.4.4 Temperature distribution

Figure 5.9 and Fig. 5.10 show the distributions of electron entropy and that of ratio between proton temperature and electron temperature, respectively. The electron heating fraction for turbulence is proportional to inverse plasma beta ${\beta_{\rm p}}^{-1}$. Therefore, a jet with a strong magnetic field has a higher electron temperature i.e., the ratio between proton

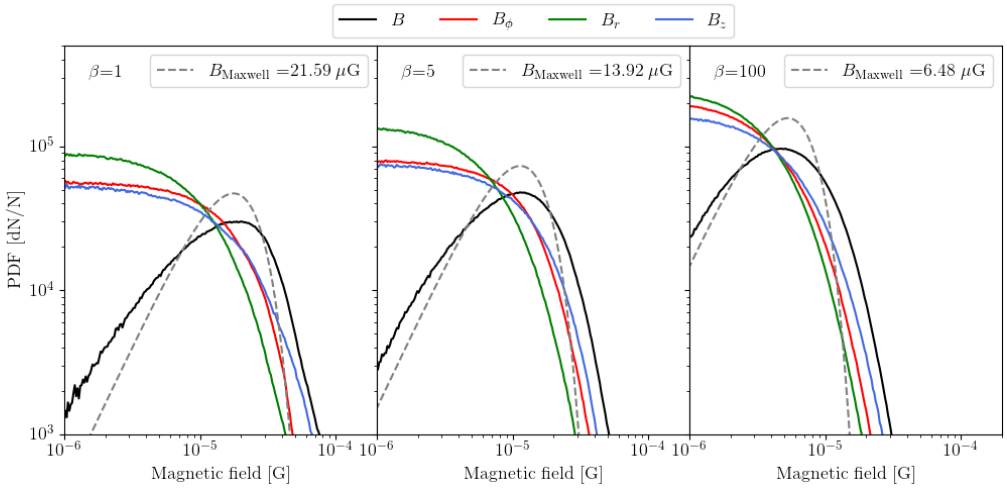

Fig. 5.8: Probability distribution functions of magnetic field strength in the cocoon for model A, B, and C at the end of the simulations. Red, green, blue, and black lines plot respectively $|B_\phi|$, $|B_r|$, $|B_z|$, and $|B|$. Gray lines plot the Maxwell-Boltzmann function for mean field strength $B_{\rm Maxwell}$ given in Eq. (5.38).

temperature and electron temperature is small.

Thermal electrons propagating the beam cannot the heating energy of the internal shocks, but electrons heat up at the jet termination region (Fig. 5.9). Hot electrons, therefore, are stored in the cocoon. Although this physical picture is similar to the result of the two-dimensional case (see chap Sect. 4.4.2), the difference between them is that dissipation of the magnetic energy play role of electron heating source as that of the bulk kinetic energy of jets. In particular, the electrons are significantly heated locally in the beam for models A and B.

In contrary to electrons, protons receive most of the shock heating because we set $f_{\rm e} = 0.05$. Thus, proton temperatures are several ten times higher than electron temperatures in the cocoons for all models (Fig. 5.10). Electrons are in relativistic temperature in range of $T_{\rm e} \sim 10^9 - 10^{10}$ K. Hotter electrons are located along magnetized filamentary structures formed by shock compression for models A and B. In particular, electron temperatures are higher than protons temperature in some filaments of model A. Meanwhile, for model C, the distribution of ratio between proton temperature to electron temperature are monochromatic, $kT_{\rm p}/kT_{\rm e} \sim 40$, in the cocoon.

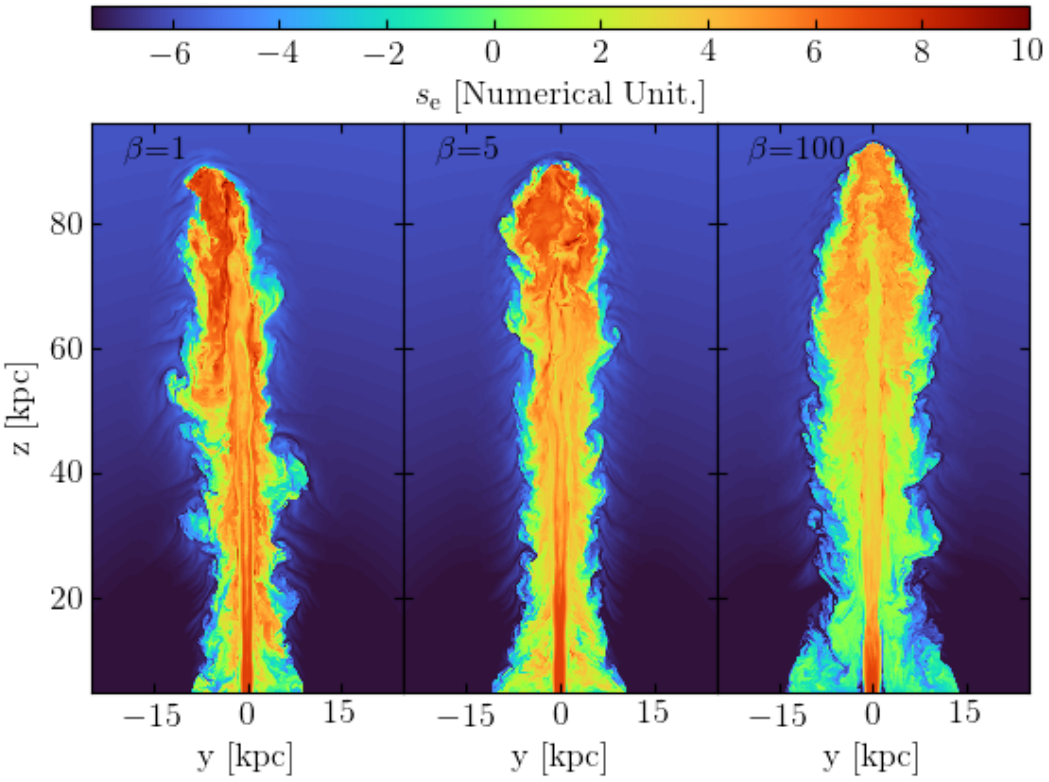

Fig. 5.9: Slices (in the $y-z$ plane) of the distribution of the electron specific entropy for model A, B, and C, respectively.

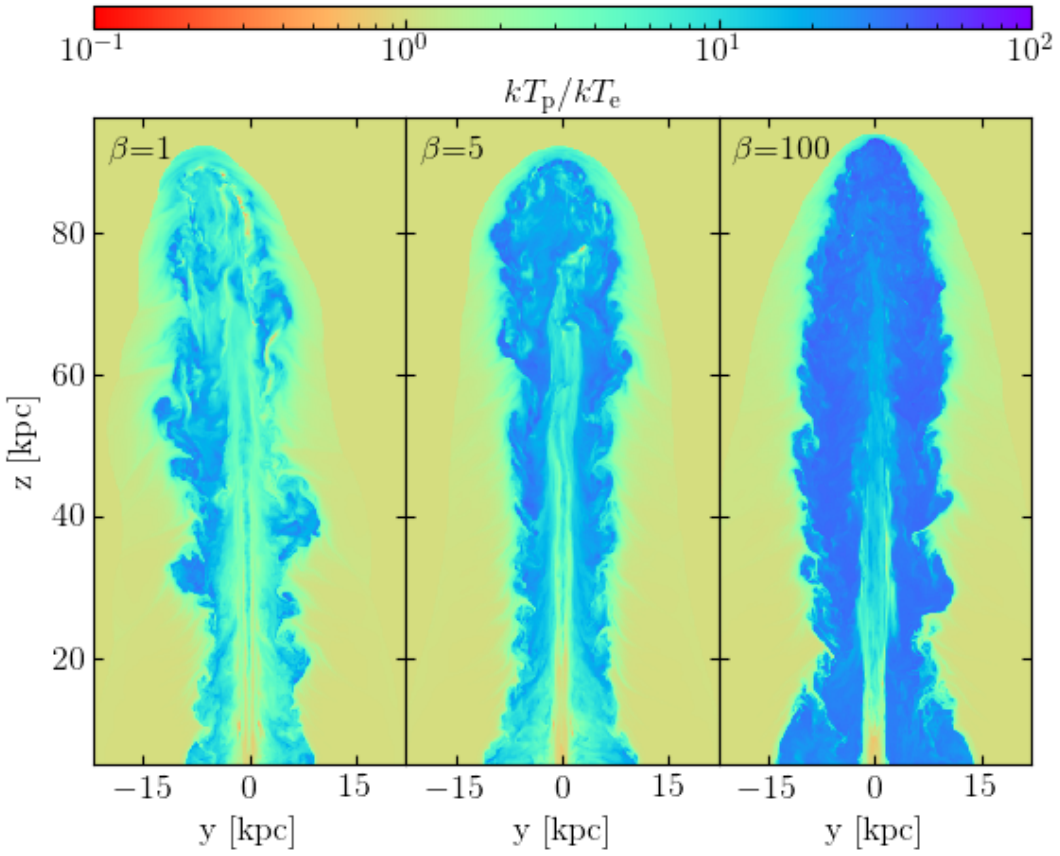

Fig. 5.10: Slices (in the $y-z$ plane) of the distribution of the ratio between proton temperature to electron temperature for model A, B, and C, respectively.

5.4.5 Thermodynamics of intracluster medium

In this subsection, we clarify the time evolution of the ICM, especially thermodynamics balance. Electrons and protons are heated by bowshocks. Note that protons are hotter than electrons in the shocked-ICM because the shocks primarily heats protons in our simulations. Shocked-ICM of all models still have a different temperature between electron and proton in the region of $z > 40$ kpc when jets reached $z \sim 90$ kpc (see Fig. 5.10). To analyze more details for ICM thermodynamics, we define shocked-ICM as the grids where $T_{\rm e} < 10^8$ K and $n(t = t') - n(t = 0) > 0.05 n_0$, where t' is the current time. In the first criterion, we divide the cocoon or not, and the second criterion divide the shocked-ICM or non-perturbed ICM. Figure 5.11 shows the averaged density of shocked-ICM (top) and the averaged ratio of proton to electron temperature of shocked-ICM (bottom) along z-axis for model B at $t = 2.8,\ 4.2,\ 5.6,\ 8.4$,and 9.8 Myr, respectively. Here, the averaged quantities q of shocked-ICM along the z-axis is calculated in the form,

$$< q(z) >= \frac{\int\int q dx dy}{\int\int dx dy} \quad \text{for} \quad T_{\rm e} < 10^8 \text{ K} \quad \text{and} \quad n(t = t') - n(t = 0) > 0.05 n_0. \tag{5.40}$$

The initial density profile is β-model, and thus the averaged density profiles of shocked-ICM along with z-axis have a lower value as it is father from the core (see in the top panel of Fig. 5.11). One can see that the density has the highest value at the tips of the bowshock. In particular, shock compression is effective in early time. The averaged density of shocked-ICM is also decreased in time because of adiabatic expansion. Electrons and protons are decoupled in shocked-ICM during simulation time (see the bottom panel of Fig. 5.11). Around the tips of the bowshock, the temperature ratios between protons and electrons are about 6 for all plots. In contrast, electrons and protons reached thermal equilibrium in the area close to the core because Coulomb coupling is effective due to high density and shocked plasma has passed for a long time.

Since the shocked-ICM is high plasma-$\beta_{\rm p}$ value $\beta_{\rm p} > 100$, the electron cannot receive heating energy by turbulence, i.e. $f_{\rm e} \to 0$ (see Eq. (5.28)). Thus, the electron thermodynamics is simply described by sum of energy gain process by Coulomb interaction and energy loss process by radiation. In the case of single-temperature plasma, electrons lose energy by radiation. Meanwhile, for two-temperature plasma, we verify that firstly electrons are heated by Coulomb coupling i.e., the heating ratio through Coulomb collisions is higher than cooling ratio through bremsstrahlung radiation. Then, electrons lose energy

through radiation after that protons and electrons are in thermal equilibrium.

In contrast to electrons, the sound wave is another important heating source of protons for shocked-ICM. The origin of sound wave production is the supersonic turbulence motion of cocoon plasma (see Fig. 5.3). Sound waves selectively heat protons because $f_{\rm e} \to 0$ in shocked-ICM. In Fig. 5.12, we plot radial profile for electron (blue) and proton (red) temperature for model B at t = 8.4, (top) 9.1 (middle) 9.8 (bottom) Myr, respectively. All panels plot along x-axis at $z = 60$ kpc and $y = 0$ kpc. One can see that a strong sound wave propagates in shocked-ICM from the cocoon to the bowshock in the top panel of Fig. 5.12 at z =4, 5, and 6 kpc. Thus, proton temperature at shocked-ICM decreases with radial direction. Meanwhile, electrons could not receive heating energy through the sound wave. Electron temperature increase with r direction because of adiabatic expansion, i.e., electron temperature of shocked-ICM is maximum at the shock front. Since the post-shock electron temperatures of the shocked-ICM are less than the temperatures estimated by the shock jump condition from X-ray observation of Cygnus A, the two-temperature plasma may play role to give a physical explanation of this phenomena (Snios et al., 2018).

5.4.6 Lobe energetics

The left panel of Fig. 5.13 displays the time evolution of different energy components of the cocoon for all the models. Proton thermal energy is the dominant energy component of the cocoon ($U_{\rm p} \gg U_{\rm e}$), i.e., cocoons are supported by the proton pressure (see red lines and blue lines in the left panel of Fig. 5.13). We confirm that the kinetic energy is comparable to the proton thermal energy and that 20 percent of total injected energy is converted to the ICM at $t = 10$ Myr. Since the electron heating fraction of turbulence is an increasing function of ${\beta_{\rm p}}^{-1}$, there is a positive correlation between electron thermal energy and field strength. (see dashed lines, solid lines, and dotted lines for magnetic energy and electron thermal energy in the left panel of Fig. 5.13).

In the right of Fig. 5.13, we plot the time evolution of the ratio between the magnetic field and the electron thermal energy in the cocoon. The energy ratio for model A and B saturates at ~ 0.7. The electron pressure is described by $p_{\rm e} = (\gamma_{\rm e} - 1)u_{\rm e} = 2/3u_{\rm e}$ for $\gamma_{\rm e} = 5/3$, and hence it is in pressure equilibrium with the magnetic field. Meanwhile, in the case of model C, the electron pressure is slightly larger than the magnetic pressure.

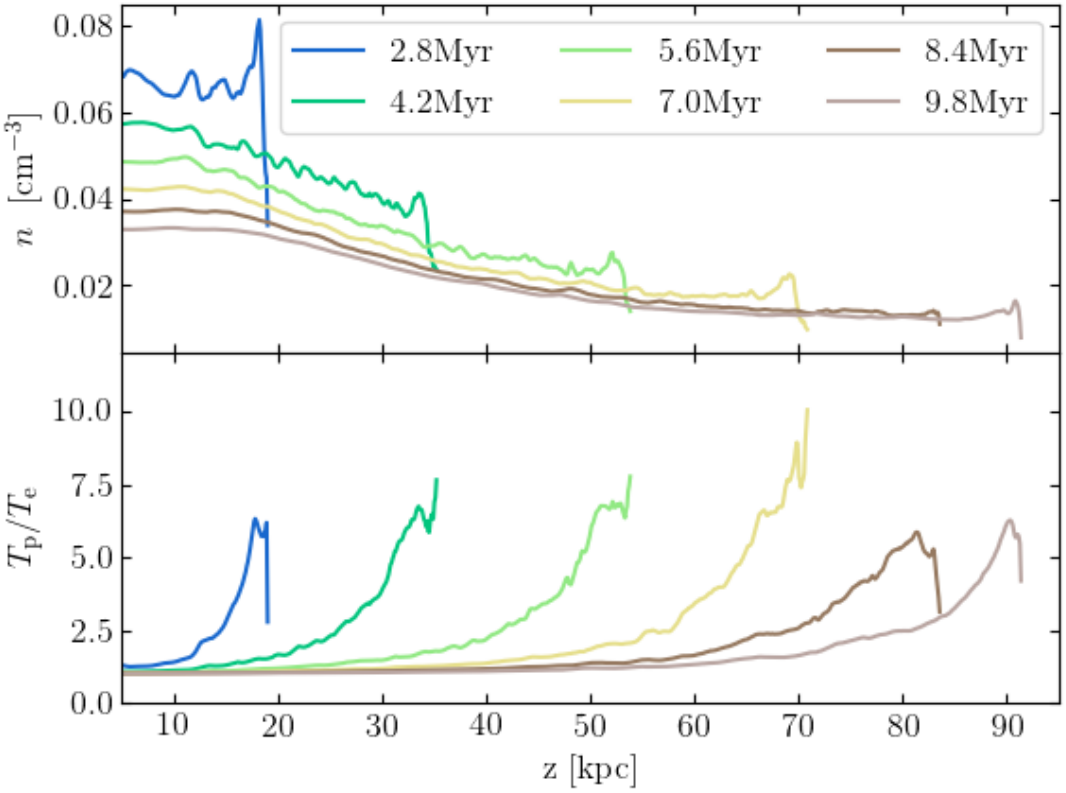

Fig. 5.11: **top**: The averaged density profile of shocked-ICM along z-axis for model B at t = 2.8, 4.2, 5.6, 8.4,and 9.8 Myr. **bottom**: Same as top panel, but plot the averaged ratio of proton to electron temperature.

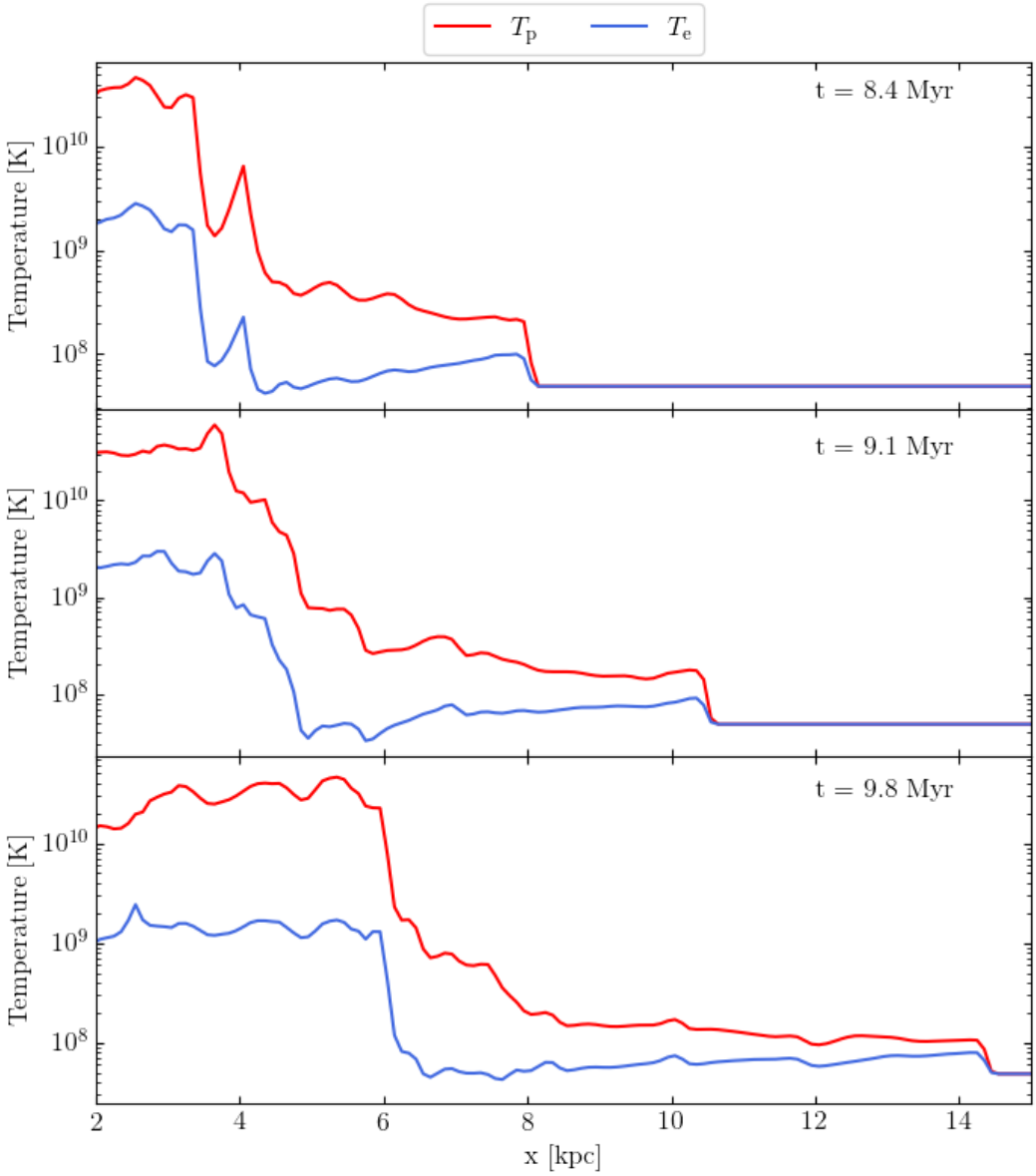

Fig. 5.12: Radial profile for electron (blue) and proton (red) temperature for model B at t = 8.4 (**top**), 9.1 (**middle**), and 9.8 (**bottom**) Myr, respectively. All panels plot along x-axis at $z = 60$ kpc and $y = 0$ kpc.

Thermal electrons evolve while being received a large amount of dissipation energy via shocks and turbulence. If the gas is reached in an turbulence equilibrium discussed in Sadowski et al. (2017), the final temperature ratio is determined by the electron heating model, and is given by

$$\left.\frac{T_{\rm p}}{T_{\rm e}}\right|_{\rm eq} = f_{\rm e,turb}(T_{\rm e}, T_{\rm p}, \beta_{\rm p}), \tag{5.41}$$

where we adopt $\gamma_{\rm p} = \gamma_{\rm e} = 5/3$. A quasi steady state of MHD turbulence can be seen in the $T_{\rm e}/T_{\rm p} - \beta_{\rm p}$ histogram of the left panel of Fig. 5.14. This histogram plots the gas stored in the cocoons for model B at $t = 9.94$ Myr. We can see that the gas distribution along with the dashed line, which is plotted as Eq. (5.41). This means that energy components ($U_{\rm p}$, $U_{\rm e}$, and $U_{\rm mag}$) evolve following to the electron heating model of MHD turbulence. Therefore, the electron heating model of turbulence plays a significant role in the determination of the gas thermal evolution in our models. Heating ratio of protons to electrons, $Q_{\rm p}/Q_{\rm e}$ in the turbulence heating model saturates at ~ 30 for $\beta_{\rm p} > 10$, and therefore the minimum temperature ratio is located at $(T_{\rm e}/T_{\rm p}) = 1/30$ (see Eq. (5.28)). Another view on an turbulence equilibrium is the relationship between $U_{\rm e}$ and $U_{\rm mag}$, shown in the right panel of Fig. 5.14. One can see that the gas distributes along the line, shown $U_{\rm e} = U_{\rm mag}$, in this histogram. Thus, we find that the electrons evolve toward energy equipartition (pressure equilibrium) with the magnetic energy when $\beta_{\rm p} < 10$ in the cocoon for model A and B.

For model C, proton plasma-$\beta_{\rm p}$ is higher than 10 in the whole region of the cocoon. Therefore, the electron are received heating energy as a constant fraction at turbulence, $f_{\rm e} \sim 1/30$. We verify that $U_{\rm e}/U_{\rm p} \sim 1/30$ in the cocoon for model C after 5 Myr. The gas does not distribute along the line that $U_{\rm e} = U_{\rm mag}$ in a $U_{\rm e} - U_{\rm mag}$ histogram. Also, the magnetic energy is subdominant compared with the electron thermal energy. One may see that $U_{\rm e}/U_{\rm mag}$ saturates at ~ 0.4 for model C in the right panel of Fig. 5.14. However, there is no relationship between $U_{\rm e}$ and $U_{\rm mag}$ when $\beta_{\rm p} \gg 10$ in a cocoon.

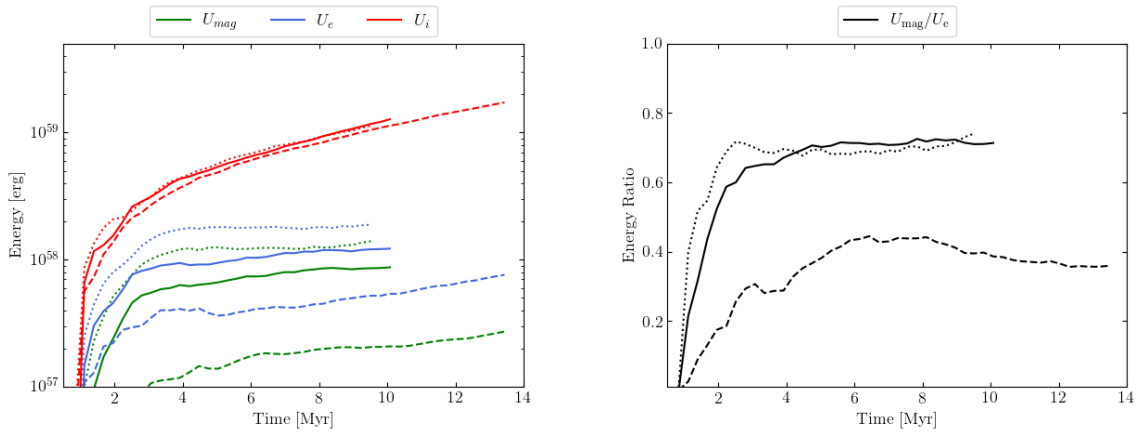

Fig. 5.13: **Left**: Time evolution of different energy components of the cocoon for model A (Dotted lines), B (Solid lines), and C (Dashed lines), respectively. We define the cocoon as the grids that have a electron temperature higher than 10^8 K. **Right**: Time evolution of the ratio between the magnetic field and the electron energy (Black) for model A (Dotted lines), B (Solid lines), and C (Dashed lines) respectively.

5.5 Discussion

5.5.1 Small-scale dissipation in jet beam

As we reported in Sect. 5.4.2, beams suffer MHD instabilities. The growth of instabilities leads to the formation of current sheets, where magnetic reconnection takes place. Magnetic reconnection is a dissipation mechanism and able to energize non-thermal particles. Notice that although we do not explicitly deal with resistivity, magnetic reconnection arises due to the numerical dissipation. The magnetic energy dissipation rate is given by ηj^2, where η is the resistivity and j is the current density. However, it is difficult to measure the numerical resistivity in ideal MHD simulations. Thus, following Zhang et al. (2017), we quantify dissipation to be proportional to the strength of $\boldsymbol{j} \cdot \boldsymbol{E}$, where $\boldsymbol{E} = -\boldsymbol{v} \times \boldsymbol{B}$ is the electric field.

Fig. 5.15 display the volume-renders of a physical quantity $\boldsymbol{j} \cdot \boldsymbol{E}$ at times that jets reach 60 kpc. Note that the color bar scale of the panel (c) is 0.2 times narrower than that of the panel (a) and (b). Peaks of dissipation take place around the jet head for all models because of the shock compression at the termination shocks. This feature can be

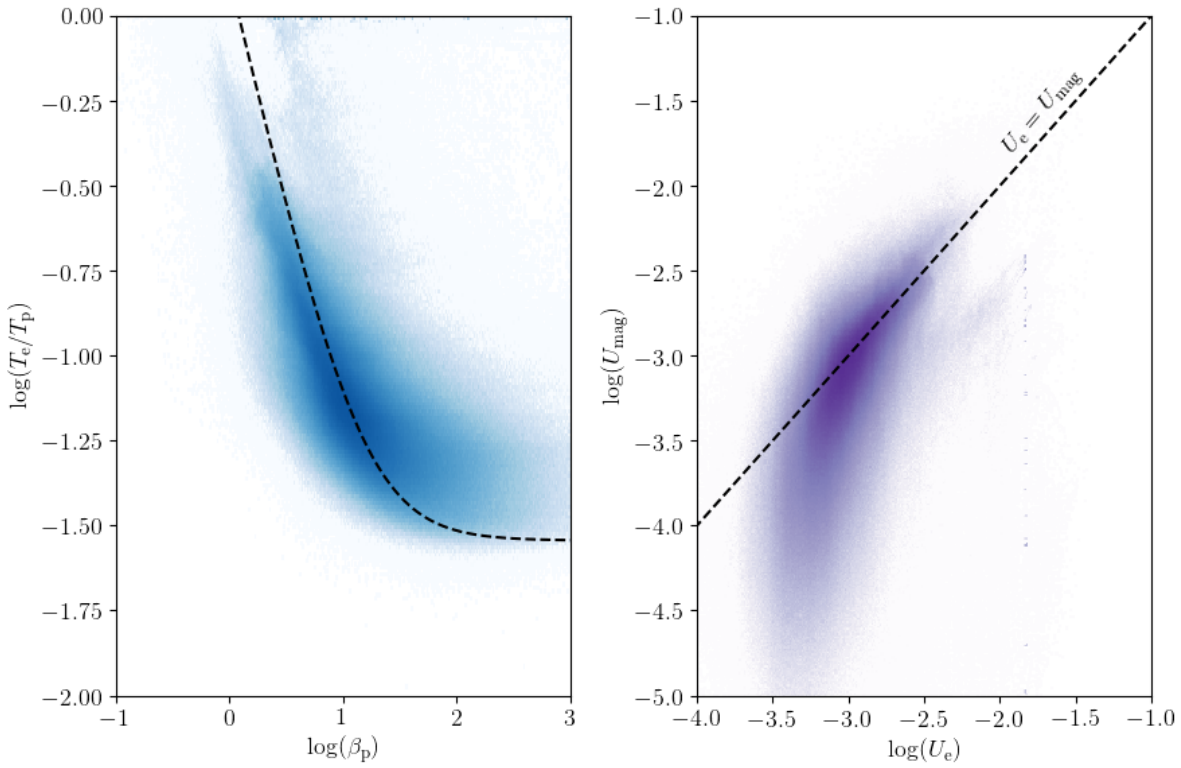

Fig. 5.14: **Left**: $T_e/T_p - \beta_p$ histogram for regions in the cocoon for model B at $t = 9.94$ Myr. The dashed line show electron to proton temperature ratio corresponding to the equilibrium state for give plasma β_p as implied by the turbulence heating in Eq. (5.41). **Right**: Same as left panel, but display $U_e - U_{mag}$ histogram. The dashed line plots $U_e = U_{mag}$.

seen as a typical powerful FR-II type jets. For model A entered the non-linear phase for the kink mode, the beam core is fragmented, which are shown in the beam at $30 < z < 50$ kpc in the left panel of Fig. 5.7. This fragmented structure identifies as a dissipation region, which shows a small-scale periodic structure at $30 < z < 50$ kpc for model A. Meanwhile, the value of $\boldsymbol{j} \cdot \boldsymbol{E}$ is high at the shear layer between beam and cocoon for model B. The growth of Rayleigh-Taylor mode drive gas mixing between the beam and the cocoon and magnetic fields accumulate in the shear layer. Therefore, the beam radius of model C in Fig. 5.15 looks larger than that of model A and B.

After jets propagate at 95 kpc, the dissipative structures of the three models are significantly different (Fig. 5.15). We can see the fragmentation structures at $30 < z < 60$ kpc for model A at this time. Magnetic energy is dissipated in this region, and hence the flow is laminar downstream of this region ($60 < z < 70$ kpc). Dissipative spots are formed by shock, in particular, the shock is induced by magnetic pinching at $z = 70$ kpc. For model B, we can see the abrupt change of flow direction by the development of a beam kink at $z = 60$, 70, 80 kpc. Hence these localized spots, where the flow is shocked and bent, could be reconnection layers, efficient particle acceleration would take place. Such beam disruption can explain the formation mechanism of the double hotspots in the western lobe of Cygnus A (Carilli & Barthel, 1996) and of the multiple knots observed 3C273 (Uchiyama et al., 2006). Meanwhile, the model C jet cannot expect the formation of multiple hotspots. Although the model C jet has the dissipative spot at the jet head, the dissipative ratio for magnetic energy is distributed with uniformity. Therefore, the jet at the later phase of model C has a feature of FR-I type jets such as M84, having an extended diffusive radio lobe without hotspot (Laing et al., 2011). Jet deceleration by the development of Rayleigh-Taylor instabilities would be a possible explanation of FR dichotomy, being consistent with previous simulations (Massaglia et al., 2016; Rossi et al., 2020).

5.5.2 Comparison with post-processing method

Our works derive the electron temperature with self-consistent electron heating. Meanwhile, in the previous work for two-temperature MHD simulations for the context of hot accretion flows, the electron temperature is calculated by the post process from the simple

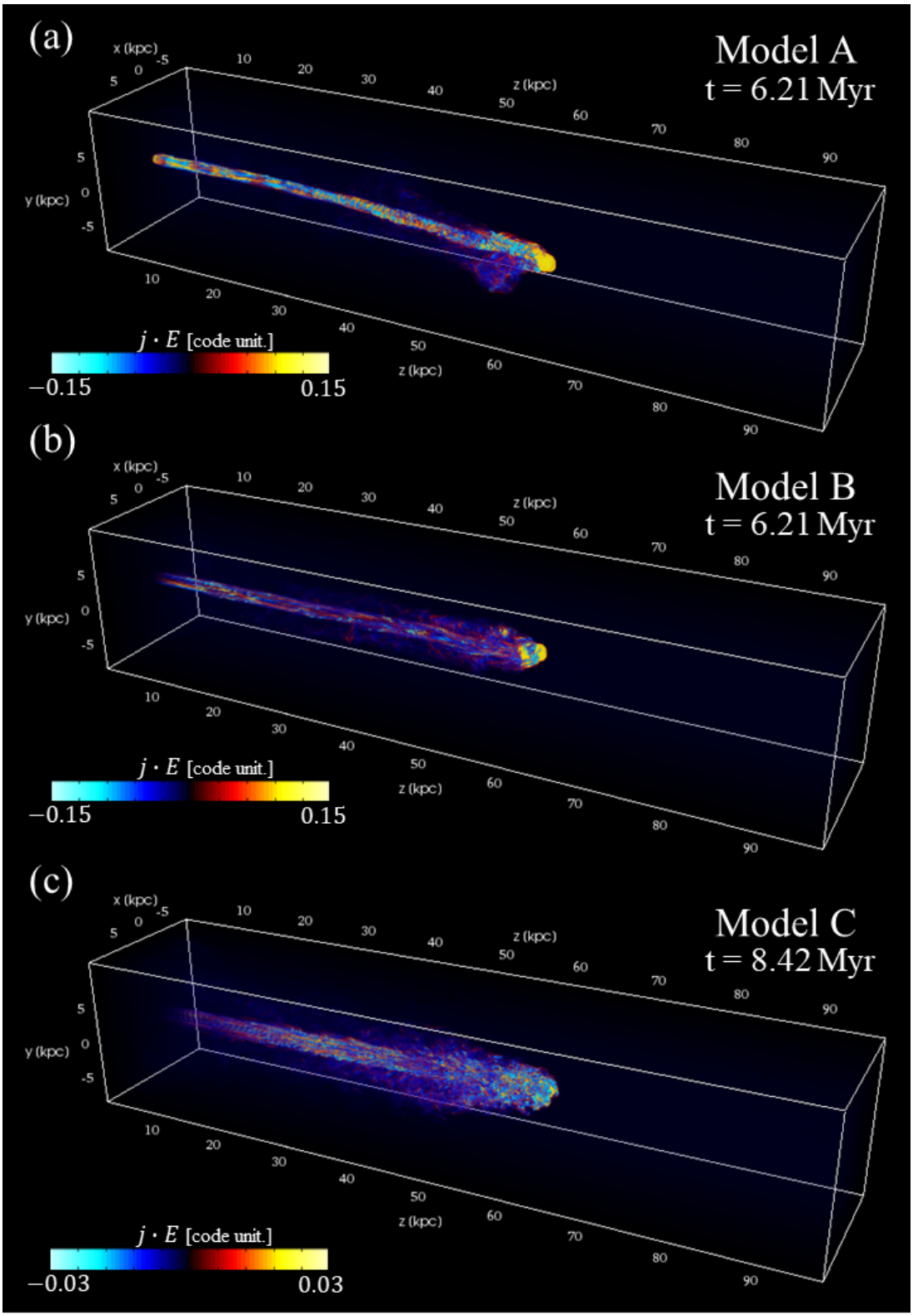

Fig. 5.15: The three panels represent the magnetic dissipative structures at early stages fol all models. In each panel we show volume-renders of the strength of $\boldsymbol{J} \cdot \boldsymbol{E}$.

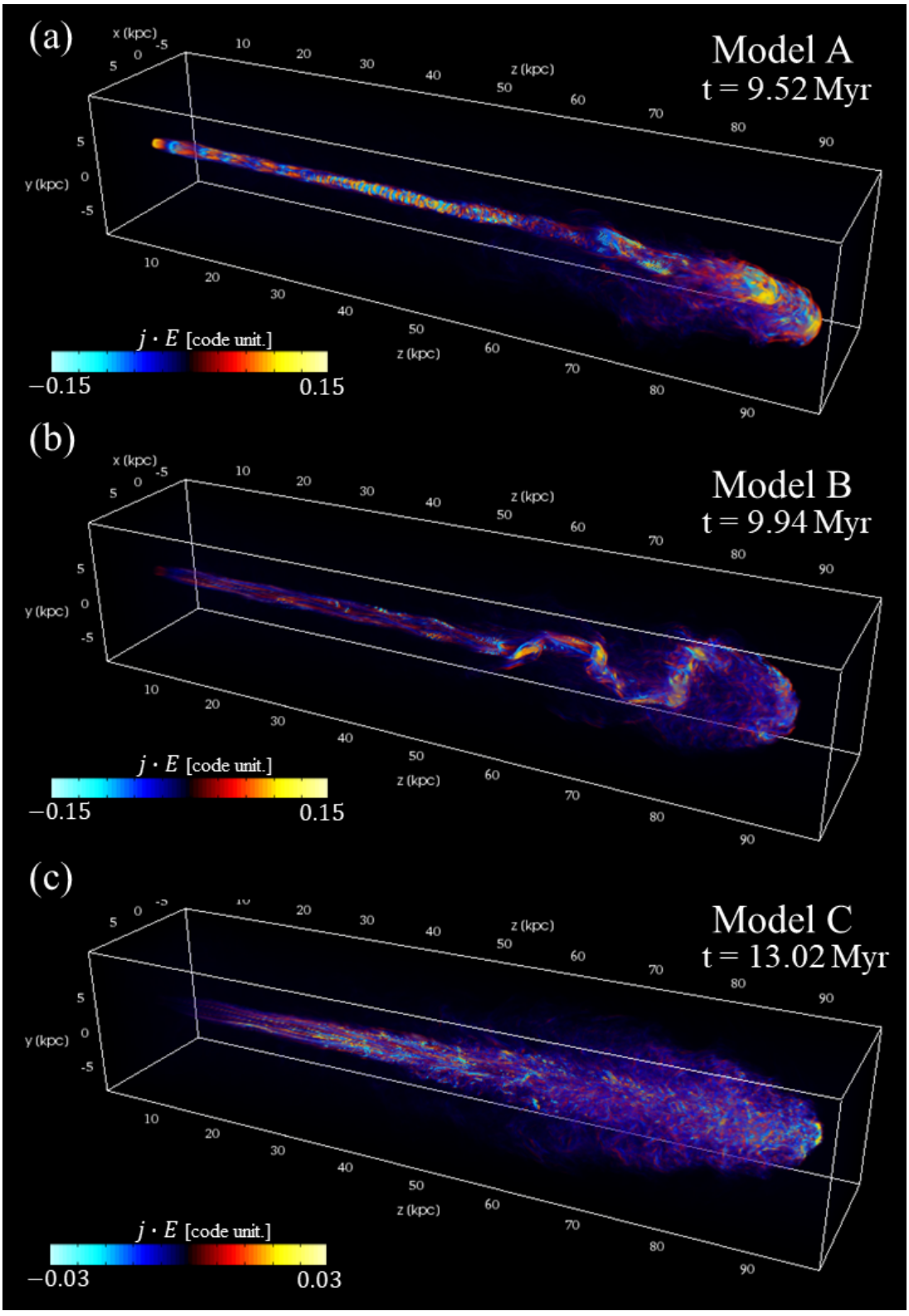

Fig. 5.16: Same as Figure 5.15 but at later phase.

formula using snapshot MHD quantities because of low-computational costs (e.g., Drappeau et al., 2013; Mościbrodzka et al., 2016). Also, as we reported in Sect. 5.4.6, our result suggests that electrons and protons are almost reached in turbulence equilibrium states. Therefore, we compare the electron distribution of our model with that obtained by post-processing methods and turbulence equilibrium conditions.

The formulation of temperature relation between ion and electron (Mościbrodzka et al., 2016), which is widely accepted, gives us the ion-electron temperature ratio in the form,

$$R \equiv T_{\rm p}/T_{\rm e} = \frac{R_{\rm low} + R_{\rm high}\beta^2{}_{\rm p}}{1+\beta^2{}_{\rm p}}, \tag{5.42}$$

where $R_{\rm low}$ and $R_{\rm high}$ are parameters for minimum and maximum temperature ratio. In this work, we adopt $R_{\rm low} = 1$ and $R_{\rm high} = 15$ to normalize electron temperature in the cocoon. Then, the electron temperature (hereafter $T_{\rm e,M16}$) is calculated using gas temperature as:

$$T_{\rm e,M16} = T_{\rm gas}/R. \tag{5.43}$$

Note that this formulation assumes that proton temperature and gas temperature are equal ($T_{\rm gas} = T_{\rm p}$), but this assumption is broken when the electron temperature is much higher than the proton temperature. Therefore, $R_{\rm low} \geq 1$ necessarily. Another way to calculate electron temperature by post process is to use the electron heating model in turbulence given in Eq. (5.28). Thus, we estimate the electron temperature (hereafter $T_{\rm e,K18}$) using gas temperature as:

$$T_{\rm e,K18} = T_{\rm gas}/f_{\rm e,turb}. \tag{5.44}$$

We compare the three electron temperature for model B: $T_{\rm e,B}$ which is obtained by the two-temperature MHD simulation, $T_{\rm e,K18}$, and $T_{\rm e,M16}$. As one can see in Fig. 5.17, the distribution of $T_{\rm e,K18}/T_{\rm e,B}$ shows large fluctuations. Note that the electron heating model in turbulence only gives the fraction of heating going into electrons and ions. Hence the heating is not spatially uniform, and it takes some time to reach turbulence equilibrium, $T_{\rm e,B}$ need not to $T_{\rm e,K18}$. Meanwhile, the distribution of $T_{\rm e,R16}/T_{\rm e,B}$ shows smaller fluctuations than that of $T_{\rm e,K18}/T_{\rm e,B}$ (see the right panel of Fig. 5.17). We mentioned again that we determine the value of $R_{\rm high}$ to satisfy $T_{\rm e,R16}/T_{\rm e,B} \sim 1$ in the cocoons. $T_{\rm e,R16}$ is lower than $T_{\rm e,B}$ in magnetized filaments. Also, post processing method

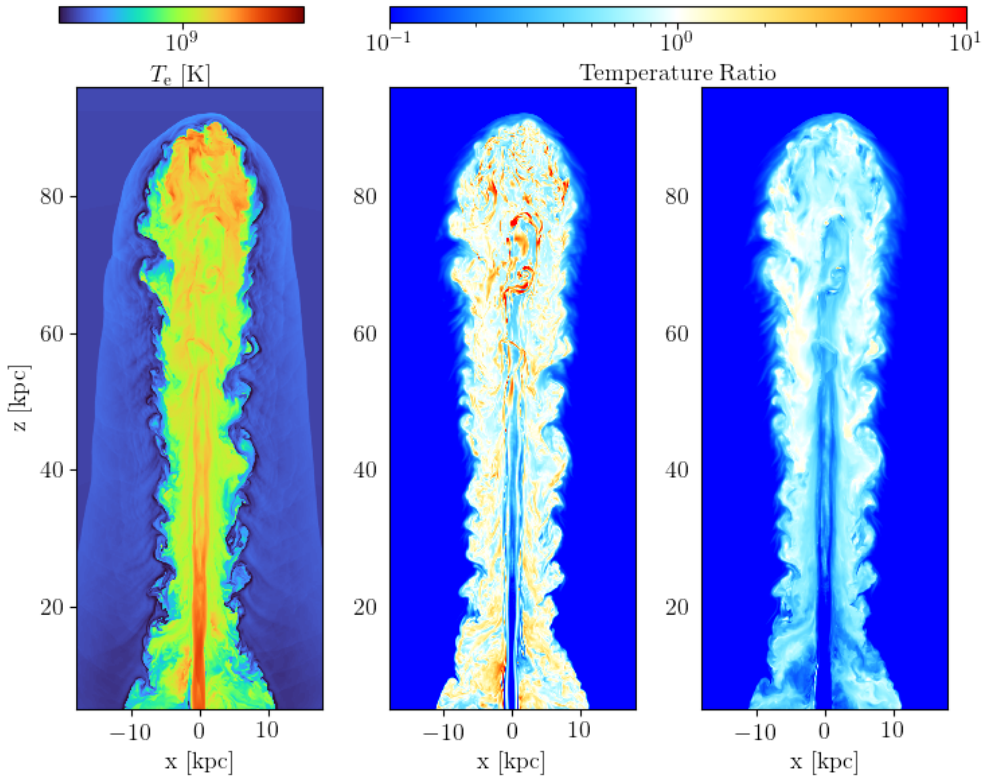

Fig. 5.17: **Left**: The slices ($x-z$ plane) of electron temperature distribution $T_{\rm e,B}$ for model B at $t = 9.94$ Myr. **Middle**: The slices ($x-z$ plane) of $T_{\rm e,K18}/T_{\rm e,B}$ for model B at $t = 9.94$ Myr, where $T_{\rm e,K18}$ is the electron temperature assumed in turbulence equilibrium. **Right**: Same of the middle panel, but display $T_{\rm e,M16}/T_{\rm e,B}$, where $T_{\rm e,M16}$ is the electron temperature calculated by post-processing method using Eq. (5.43)

of Mościbrodzka et al. (2016) may under estimates the electron temperature near the core, $z < 30$ kpc. Dissipation energy is, in fact, converted into electron thermal energy but also non-thermal electron energy. The low-frequency radio emission, which traces low-energy non-thermal electrons, extends around a core (McKean et al., 2016), and hence the turbulence heating around the core might play a significant energy source for low-energy non-thermal electrons. For both post-processing method, $T_{\rm e,B}$ is higher than those electron temperatures. Note that the artificial effect of the injection temperature condition includes the beams. The effect of the injection condition is discussed in Sect. 4.4.3.

5.5.3 Comparison with observations

We discuss that our two-temperature MHD models connect to observational result. In particular, we focus on the relationship between jet mechanical power and radio power. Observational data sets of X-ray and radio properties are taken from Laura Bîrzan's PhD thesis (Rafferty, 2007) and Rafferty et al. (2006).

Radio synchrotron emission

The radio maps are obtained by solving the radiative transport equations for the synchrotron emission. The details for this equations see Sect. A.3. To calculate the synchrotron emissivity, the population of non-thermal electrons, which are injected and/or accelerated in microscopic physics such as collisionless shocks and magnetic reconnection, is needed. Meanwhile, the two-temperature MHD simulations account only for the evolution of the thermal electrons. Following previous works, non-thermal electron energy is propositional to thermal gas energy or magnetic energy as a first-order approximation (e.g., Gomez et al., 1995). This work follows this approximation. We adopt the two-type model for approximation of non-thermal electrons as case 1T and case 2T. Case 1T is $N_0 = C_0 u_\mathrm{p}$, and case 2T is $N_0 = C_0 u_\mathrm{e}$. Here $C_0 = \eta(p-2)(m_\mathrm{e}c^2)^{p-1}/(m_\mathrm{e}c^2)$ and $\eta = 0.2$ is a parameter, which is a ratio of the non-thermal electron energy density to the electron thermal energy density. This would underestimate the value of η since PIC simulations have revealed that $\eta \sim 0.7$ in turbulence (Zhdankin et al., 2019). Case 1T is corresponded to the single-temperature model, i.e., $T_\mathrm{e} = T_\mathrm{p}$. We assume that an electron energy index, $p = 2$. For all calculations, the viewing angle, which is respect to the $z-$axis, is 80 degrees, and the observed frequency is 144 MHz. Note that the observed frequency affects the polarization signature, but the discussion of radio morphology and polarization signature is out of scope in this thesis.

The radio power is calculated by the sum of the radio intensity of all grids. We list the calculated radio powers in Tab. 5.3 (see also Fig. 5.19). The radio power of model A-1T, which is most prominent model, is two order of magnitude higher than that of model C-2T. The 1T models have same order of non-thermal electron energy because the proton temperatures have the roughly same value in lobes (see the left panel of Fig. 5.13). Note that 1T models assume that non-thermal electron energy is proportional to proton

Table 5.3: Radio power and the amount of PdV-work for the simulation results

Model	$P_{\rm radio}$	pV
	$[10^{42}$ erg s$^{-1}]$	$[10^{58}$ erg$]$
A-1T	63.2	5.95
A-2T	7.23	-
B-1T	52.2	6.58
B-2T	2.83	-
C-1T	24.0	9.22
C-2T	0.62	-

temperature. Meanwhile, electron temperatures are varying for three simulation models, and they are proportional to inverse injection fields. Thus, there are a large scatter in the radio powers of 2T models, than that of 1T models. This means that the radio power of two-temperature models is sensitive to fields energy.

X-ray cavity and the jet mechanical power

Our model injects constant jet energy during simulation time, i.e., jets are in an active phase, and hence true mechanical power in units erg s^{-1} are known. Meanwhile, we can obtain snapshots quantities and the gas pressure of surrounding ICM through the actual observations. A similar manner for observations, therefore, is adopted in this work. In X-ray observation, the method for measurement of the mechanical power is using PdV work as follows:

$$P_{\rm cav} = 4 p_{\rm gas} V {t_{\rm age}}^{-1}, \tag{5.45}$$

where $t_{\rm age}$ is the outburst age of jets. Lobes and ICM are approximately in the pressure equilibrium state. Thus, we use the initial ICM pressure around middle of lobe $p_{\rm gas} \sim \ 2.0 \times 10^{-10}$erg cm^{-3} to calculate cavity power (see Fig. 5.1). Three estimations are commonly used for the outburst age: the buoyancy time $t_{\rm buoy}$, the refill time $t_{\rm r}$, and the sound crossing time $t_{\rm c}$, generally $t_{\rm c} < t_{\rm buoy} < t_{\rm r}$. It is appropriate to use the sound crossing time in our model because jets are in an active phase. The cavity volume V is

calculated by integrating the numerical grids with an electron temperature exceeding 10^8 K. We confirm that the region whose electron temperature exceeding 10^8 K have a lower density than ICM.

We first mention the morphological properties of the X-ray cavity. In Fig. 5.18, we compare our simulation of model B with observations about the relationship between the projected distance from the core to the cavity center R and the projected semi-minor axis of the cavity b. Note that since R and b for model A and model C have the similar value of that for model B, we only show the result of model B in Fig. 5.18. The cavity of model B is narrow compared with observed radio-fill cavities. This long and narrow structure is characteristic of powerful (kinetic-dominated) jet seen in many previous studies (e.g., Massaglia et al., 2016; Perucho et al., 2019; Mukherjee et al., 2020). To create a broad cavity, the jet should propagate slowly to have enough time to expand. Thus, a simple solution forming a broad cavity is to model a low-density jet. Or, long-periodic precession may play an important role in forming observed broadening cavities (Horton et al., 2020). We reported that jets for model B decelerate and have precession due to the development of large-scale kink modes (see Fig. 5.4). Thus, if we enable longer-time and larger-scale simulation of model B, the cavity tends to be the spherical shape.

Next, we discuss energy and age by the observational method. The cavity energies are calculated as $E_{\rm cav} = 4pV = 2.4 \times 10^{59}$, 2.6×10^{59}, and 3.7×10^{59} erg for model A, B, and C, respectively. Also, the sound crossing time $t_{\rm c} = R/c_{\rm s,ICM}$ is 51.6 Myr, where we adopt that $R = 45$ kpc and $c_{\rm s} = 830$ km/s (corresponding to ICM temperature $T = 5$ KeV). We, therefore, estimate the mechanical power $P_{\rm cav} = 1.5 \times 10^{44}$, 1.6×10^{44}, and 2.3×10^{44} erg s^{-1} for model A, B, and C, respectively. Hence actual age from our simulations is ~ 10 Myr for all models, the sound crossing time underestimates the mechanical power by a factor ~ 5. Even if we estimate the mechanical power using the simulation time, the injection energy of the jet is ~ 5 times higher than it. This reason is that the jet energy is converted to the thermal energy of ICM through shocks and sound waves. Furthermore, although the cocoon pressure, including the turbulence pressure, is higher than ICM pressure, we know only the information of ICM pressure through observations.

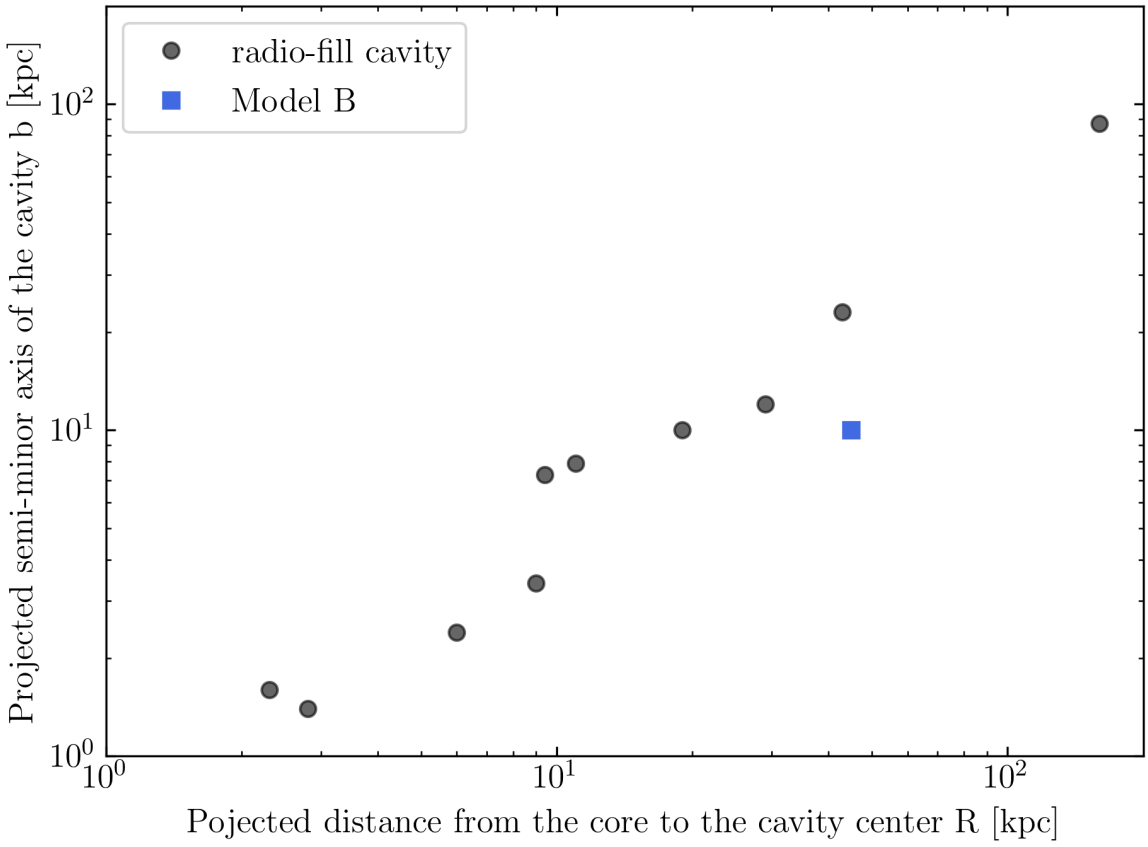

Fig. 5.18: The projected distance from the core to the cavity center R vs. Projected semi-minor axis of the cavity b. The black circles show the radio-filled cavities taken from Rafferty et al. (2006). The blue square show our result for model B at $t = 9.94$ Myr. Since R and b for model A and model C have similar value of that for model B, we do not show them.

Relationship between radio power and mechanical power

The plot of jet mechanical power $P_{\rm cav}$ versus synchrotron radio power $P_{\rm radio}$ is shown in Fig. 5.19. This plot provides us the physical insights for jet energetics, including non-radiating proton thermal energy. At a native notion, protons can be energetically dominant over in radiative inefficient lobes ($P_{\rm cav} \gg P_{\rm radio}$) because the pressure of non-radio emitting protons supports the expansion of cocoon. Our jets are active during simulation time. Therefore, we compare our results with radio-filled cavities, except for radio-ghost cavities. Although we plot the radio-filled cavities including the intermediate cases in Fig. 5.19, the samples have large scatter in the relationship, $P_{\rm cav}/P_{\rm radio} \sim 1 - 1000$.

We find that our two-temperatures model naturally explains the radiative inefficient lobes. In case 2T of all models, the lobes tend to be the radiative inefficient than that of case 1T. Since the electrons lack thermal energy compared with case 1T, radio powers are weak. Meanwhile, protons have a large contribution for cavity power $P_{\rm cav}$. Thus, radiative efficiencies, $P_{\rm cav}/P_{\rm radio}$, for case 2T are 10-30 higher than that for 1T case. One can see that the ratio of radio power between model A and model C for 2T case is higher than that for 1T case. The reason for this difference is that electron heating is coupled with the strength of magnetic fields (see Sect. 5.4.6).

This result indicates that pure protons-electrons jet is difficult to form the radiative efficient lobes, such as Cygnus A which is located at $P_{\rm cav}/P_{\rm radio} = 1$ in Fig. 5.19, without exotic processes. One of the exotic processes, herein, is ultimately efficient acceleration for electrons. To produce the radiative efficient lobes, we need the acceleration mechanism that non-thermal electron energy is more than order of magnitude than thermal electron energy, $\eta \gg 10$. Or, thermal electrons are dominant than protons due to the occurrence of an efficient electron heating process at shocks and turbulence. However, these processes do not support theoretically (e.g., Bell, 1978; Crumley et al., 2019; Zhdankin et al., 2020). Another possibility to form radiative efficient lobes is that jets have a strong magnetic field, $\beta_{\rm p} \ll 0.1$. But, this possibility is not favored for some observations (Croston et al., 2005; Isobe & Koyama, 2015).

The existence of a large number of positrons could explain the radiative efficient lobes. Recall that our simulations model the pure electron-proton jet. To achieve $P_{\rm cav}/P_{\rm radio} = 1$ in our simulations of model A and B (case 2T), the number density of leptons is, at least,

a hundred times larger than that of protons because $P_{\rm radio}$ is proportional to the number density of leptons. Note that the plasma momentum would be represent by protons under this assumption because the protons mass is a thousand magnitude greater than lepton mass. Thus, it is expected that there is no difference in the electron heating process. Meanwhile, in the case of model C, significant population of pair-plasma is need because $P_{\rm cav}/P_{\rm rad} \sim 1000$. In this condition, the electron (and positron) heating process would be change. Furthermore, the MHD approximation would not be guaranteed. Finally, we mention that analytical models of electron-positron-proton mixture jets also achieve consistent results with observed FR-II radio lobes by Kawakatu et al. (2016) and Kino et al. (2012). However, these models do not consider the electron heating process at turbulence and shocks. Therefore, the construction of the new model for the mixture jet based on two-temperature simulations are necessary.

5.6 Summary

We carried out simulations for the three models whose jet have different values of the magnetic field. To list some key results:

1. Strongly magnetized jet suffered from a developing of non-axisymmetric, current-driven kink mode. Meanwhile, weakly magnetized jets were decelerated by the high-mixing ratio between the jet beam and cocoon gas, which were induced by Rayleigh-Taylor and Kelvin-Helmholtz instability.

2. Electrons heat up at jet termination region, and hot electrons are stored in the cocoon. The electron heating fraction for turbulence is proportional to inverse plasma beta ${\beta_{\rm p}}^{-1}$. Therefore, a jet with a strong magnetic field has a higher electron temperature in the cocoon.

3. The small-scale turbulence is developed in the weakly magnetized jets. In contrary to this, the strongly magnetized jets have magnetized filaments since the magnetic tension suppresses the turbulence motion.

4. The magnetic field distribution in the cocoon is nearly isotropic for the weakly magnetized case. Meanwhile, strongly magnetized jets show a strong deviation

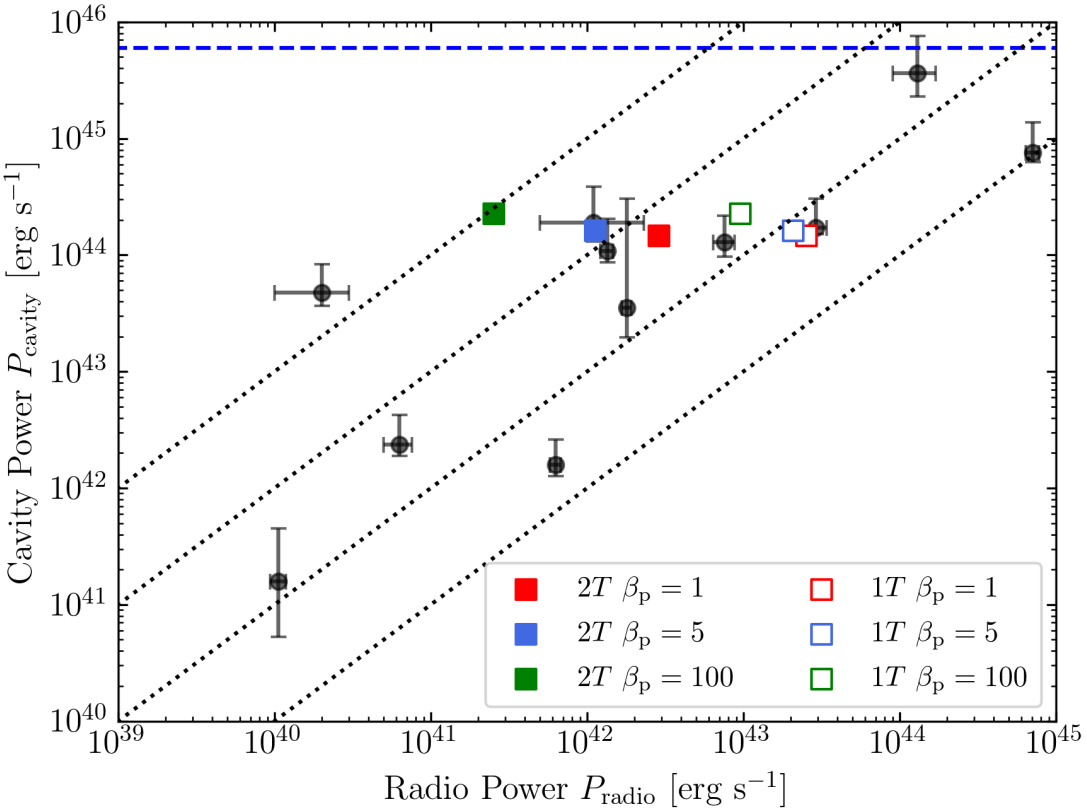

Fig. 5.19: radio synchrotron power $P_{\rm radio}$ vs. jet mechanical power estimated from X-ray cavity system $P_{\rm cav} = 4pVt_{\rm c}^{-1}$ (adopted from Laura Bîrzan's PhD thesis Rafferty, 2007). Filled black symbols show radio-filled cavities (which including the intermediate cases). The symbols and wide error bars denote the values of the mechanical power calculated using the the sound speed. Open squares and filled squares show our results of case 1T and case 2T for model A (red), model B (blue), and model C (green), respectively. The diagonal dotted lines (dashed lines) represent ratios of constant mechanical power to radio luminosity. Blue dashed lines is total injection energy of our jet model given by Eq. (5.34).

from a Maxwell-Boltzmann function.

5. In the shocked-ICM, electron temperature is still lower than proton temperature near the tip of the jets. Electrons and protons are exchange energy by Coulomb collisions. Only electrons look like cool down by adiabatic expansion due to expansion of bowshock because ions can be received heating energy through MHD waves driven by the turbulence motion of the cocoon.

6. The dominant heating source for protons is shock waves in jets. In contrast, electron evolved towards energy equilibrium to magnetic fields in turbulence developed at the cocoon.

7. The strong current is induced by the kink instability. Therefore, the high-temperature and high-magnetization hotspots are formed in the beam.

8. The electron thermal energy is much lower than the proton temperature in our model. Therefore, radio powers estimated from electron thermal energy are ten times lower than that from proton thermal energy, which is corresponded to the one-temperature approximation. our models quantitatively explained the radiative inefficient lobes.

6 Conclusion and future prospects

6.1 Conclusion

Since the first discovery of an extra-galactic jet (Curtis, 1918), a vast body of theoretical and observational studies have been done to explore its physical nature. Nowadays, thanks to the development of high-quality numerical technique and increasing computer power, magnetohydrodynamical (MHD) simulation has become one of the major tools for the dynamical modeling of the large-scale structure of jets. In this thesis, we developed dynamical models of the jet by conducting a series of MHD simulations.

Through the studies in this thesis, we succeeded for the first time in developing a two-temperature jet model that evolves the entropy equations of electrons and protons in a self-consistent manner. Our main result is that the protons are energetically dominant over the electrons in the cocoon. Firstly, most of the bulk kinetic energy of the jet is converted into thermal energy of proton through shocks. Secondly, while magnetic fields are relatively strong, shocked-electrons stored in the cocoon evolve toward energy equipartition with magnetic energy through turbulent dissipation. As a result, we find that $U_{\rm p} \gg U_{\rm e} \sim U_{\rm mag}$ in the cocoon. We mentioned that our results are model-dependent for electron heating. This physical feature, however, has been verified by the parameter study. Also, we have discussed the interpretation of our results in comparison with observations. Previous works have not studied the contribution of electron pressure and proton pressure for the cocoon expansion. Contrary to this, we have revealed that the thermal proton pressure plays the dominant role in the cocoon expansion, compared with the thermal electron pressure. This feature is one of the quantitative and physical explanations of the radiative inefficient lobes, which are frequently observed at the cluster center.

6.2 Future prospects

In this thesis, we ignore some physics, such as relativistic effect, plasma composition, heat conduction, viscosity, and resistivity. These physics might play a vital role in jet dynamics and electron heating. Another key issue is that we do not consider non-thermal particles in the jet. Observed radiations come from non-thermal particles, and we need for the distribution of non-thermal particles to calculate the radio to γ-ray emission. Thus, we have to deal with them to develop a more precise dynamical model. However, there are some issues modeling for non-thermal particle transport. The transport and acceleration processes for non-thermal particles are still unknown. In particular, there is an open question of how and where the particles are accelerated in jets. Furthermore, the physical scales of the particle acceleration are many orders of magnitude than that of the fluid. To capture small-scale kinetic physics in MHD simulations, various approaches are developed. One famous approach is a hybrid MHD-PIC method (Bai et al., 2015; Mignone et al., 2018). While non-thermal protons are treated as tracer particles, the thermal plasma is treated as a fluid. They consider feedback from non-thermal particles to the thermal plasma. Although this method can study on length scales typically of the order of a few thousand proton gyro-scales in reasonable computational cost, it is difficult to extend the physical domain to observable scales. Another approach is following the evolution of non-thermal electrons in the fluid scale with thermal plasma (e.g., Jones et al., 1999; Mimica et al., 2009; Vaidya et al., 2018; Winner et al., 2019). In this approach, diffusion approximation is applied to construct the dynamical model of non-thermal electrons. Further, the small-scale acceleration process is treated in a sub-grid model. Therefore, we can get the population of non-thermal electrons in kpc-scale jets. However, the population of non-thermal electrons is highly model-dependent. In addition, two-temperature plasma is ignored in these studies. A non-thermal component and a thermal component should have been deeply connected, and we find that the electron temperature is usually much lower than the ion temperature in jets. Therefore, it is necessary employing two-temperature MHD to follow the population of non-thermal electrons.

A Appendix

A.1 One-dimensional jet simulations

Numerical setup

We assume two separate zones in simulating the propagation of jets. The left side is a jet beam having a low number density ($n = 0.005$ cm^{-3}), high temperature ($T_{\rm i} = T_{\rm e} = 10^9$ K), and bulk velocity of 0.2c. The right side is assumed to be an ICM having high density ($n = 0.5$ cm^{-3}) and low temperature ($T_{\rm i} = T_{\rm e} = 10^6$ K). We make calculations for four models with different fractions of electron heating $f_{\rm e} = 0, 0.05, 0.2, 0.5$. In the one-dimensional simulation, we neglect the magnetic field and energy exchange through Coulomb coupling. The computational domain is $x/r_{\rm jet} \in [0, 10]$ and the number of grid points is 1024.

Results of one-dimensional simulations

Figure A.1 shows the density (black) and velocity (red) profiles at $t = 0.1$ Myr. The forward shock (bow shock), contact discontinuity, and reverse shock (terminal shock) are easily identified. Because the bow shock compresses the ICM, a high-density shocked ICM forms between the contact discontinuity and bow shock. Figure A.2 shows the temperature distribution at the same time as for the results in Fig. A.1. Solid and dashed lines respectively denote ion and electron temperatures. Colors represent fractions of electron heating of $f_{\rm e} = 0.0$ (red), 0.05 (green), 0.2 (blue), and 0.5 (black). Because most kinetic energy of the jet dissipates around the reverse shock, a high-temperature region called a hotspot forms between the contact discontinuity and reverse shock. The gas temperature of the hotspot is obtained by applying the Rankine–Hugoniot jump

condition at the reverse shock:

$$\frac{T_{\rm post}}{T_{\rm pre}} = 1 + \frac{2(\gamma_{\rm gas}-1)(\gamma_{\rm gas}M_{\rm pre}^2+1)(M_{\rm pre}^2-1)}{(\gamma_{\rm gas}+1)^2 M_{\rm pre}^2}, \tag{A.1}$$

where $T_{\rm pre} = 10^9$ K is the pre-shock temperature, $T_{\rm post}$ is the post-shock temperature, and $M = 14$ is the Mach number. We thus derive the hotspot temperature $T_{\rm post} = 6.2 \times 10^{10}$ K. In the case that $f_{\rm e} = 0.5$, the dissipative energy is divided to electrons and ions equally. The post-shock temperatures of the gas, electron, and ion are thus equal ($T_{\rm gas,pos} = T_{\rm e,pos} = T_{\rm i,pos}$) because of the same initial temperatures. Numerical values of the post-shock temperatures of ions and electrons are 6.14×10^9 K and are in good agreement with the theoretical values.

In the case that $f_{\rm e} = 0$, electrons purely evolve adiabatically; i.e., the entropy of electrons is conserved through shocks. The post-shock electron temperature is thus expressed as

$$\frac{T_{\rm e,post}}{T_{\rm e,pre}} = \eta^{\gamma-1} = 4^{2/3} \sim 2.5 T_{\rm e,post} = 2.5 \times 10^9 \text{ K}. \tag{A.2}$$

Here, η is the shock compression ratio, whose value is 4 at a strong shock when the specific heat ratio is 5/3. Meanwhile, when $f_{\rm e}$ does not equal zero, electrons receive dissipative energy from the shock. We therefore obtain the post-shock electron temperature as

$$T_{\rm e,post} = \eta^{\gamma-1} T_{\rm e,pre} + 2.0 f_{\rm e}(T_{\rm gas,post} - \eta^{\gamma-1} T_{\rm gas,pre}). \tag{A.3}$$

The post-shock temperature ratio of the electron to ion predicted using Eq. (A.3) is 0.073 and 0.269 at $f_{\rm e}$ =0.05 and 0.2, respectively. The post-shock temperature ratio of the electron to ion is actually 0.0735 and 0.269 at $f_{\rm e}$ =0.05 and 0.2, respectively, in our simulation.

A.2 Shock-finding algorithm

To identify that the MHD gird inside the shock zone or not, we implement shock-finder in MHD code CANS+, and we adopt an approach similar to that followed by Ryu et al. (2003) and Schaal & Springel (2015). Although our method is based on the theory for hydrodynamic shock, the influence of ignoring magnetic field is small for shock finding. Note that The inclusions of magnetic field complicates the system to add two types of

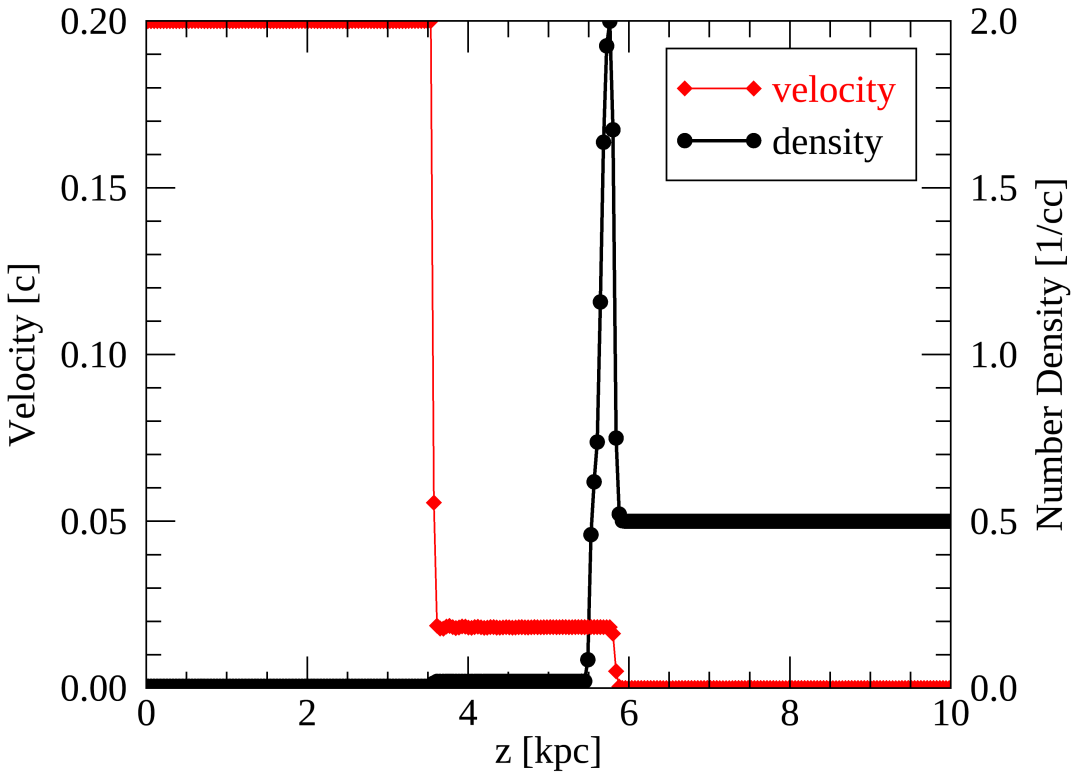

Fig. A.1: Velocity (red) and density (black) profiles for one-dimensional simulation of the propagation of a supersonic jet at $t = 0.1$ Myr. We capture the reverse shock (i.e., terminal shock), contact discontinuity, and forward shock (i.e., bow shock).

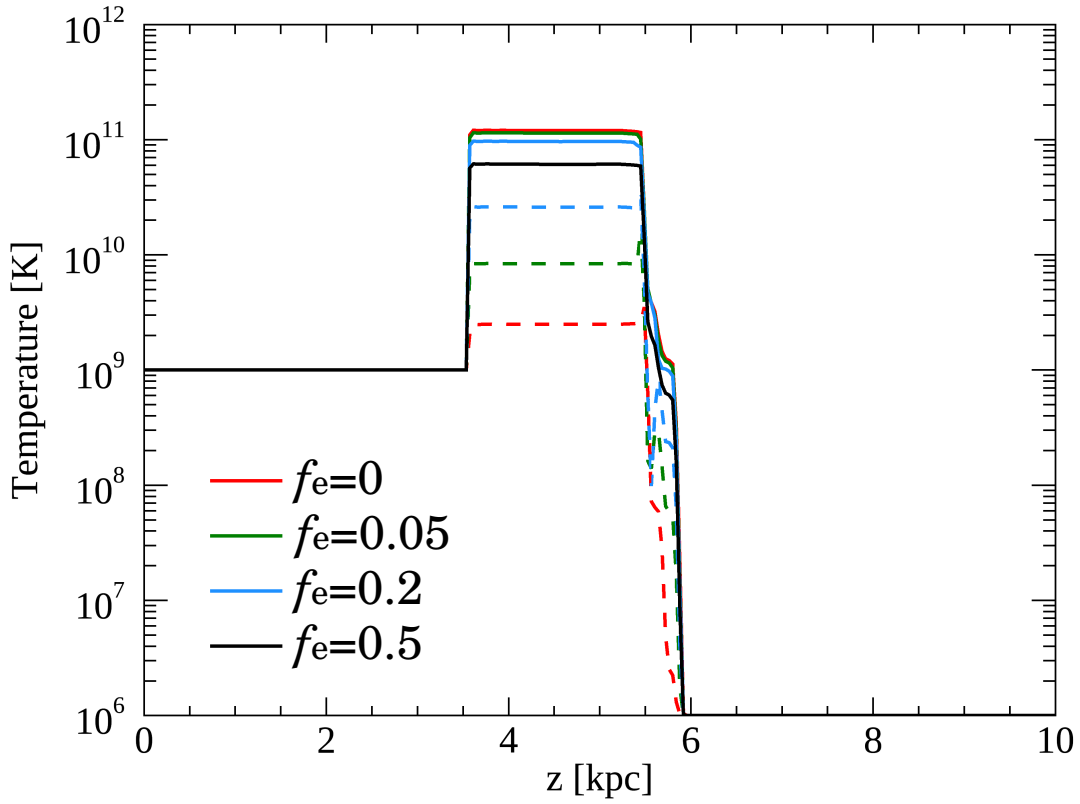

Fig. A.2: Same as Fig. A.1 but showing ion (solid) and electron (dashed) temperatures. The line colors represent the fraction of electron heating (red: $f_e = 0$, green: $f_e = 0.05$, blue: $f_e = 0.2$, black: $f_e = 0.5$). Ions and electrons heat up at both shocks, and the fraction of electron heating affects the electron temperature appreciably.

compressible shocks, and the measurement of Mach number for a MHD shock is hard task.

Here, we use the Cartesian coordinate (x, y, z), and subscript $i \in (x, y, z)$ denotes the directions of each coordinates. We divide each gird into the shock zone or not to use the following criteria

$$\nabla \cdot \boldsymbol{v} < 0, \tag{A.4}$$

$$\nabla T_{\rm gas} \cdot \nabla \rho > 0, \tag{A.5}$$

$$\mathcal{M} > \mathcal{M}_{\rm min}, \tag{A.6}$$

where, $\mathcal{M} \equiv \sqrt{\mathcal{M}_x^2 + \mathcal{M}_y^2 + \mathcal{M}_z^2}$ and $\mathcal{M}_{\rm min}$ are estimated Mach number and a minimum Mach number. In the simulations, the divergence operator replace central differences, and we adopt $\mathcal{M}_{\rm min} = 1.3$. The Mach number of each grid is estimated from the Rankine-Hugoniot condition across shocks, which is given by (Pfrommer et al., 2017)

$$\mathcal{M}_{\rm i} = \frac{1}{\gamma_{\rm gas,1}} \frac{(y-1)\mathcal{C}}{\mathcal{C} - [(\gamma_{\rm gas,1}+1) + (\gamma_{\rm gas,1}-1)y](\gamma_{\rm gas,2}-1)}, \tag{A.7}$$

where $y \equiv p_{\rm gas,2}/p_{\rm gas,1}$ and $\mathcal{C} = [(\gamma_{\rm gas,2}+1)y + \gamma_{\rm gas,2} - 1]$. Up and downstream quantities are denoted by subscripts 1 and 2, respectively. We determine the direction of shock propagation, $d_{\rm s}$, in each girds using the temperature gradient:

$$d_{\rm s} = -\frac{\nabla T_{\rm gas}}{|\nabla T_{\rm gas}|}. \tag{A.8}$$

A.3 Synchrotron polarized radiation

Relativistic charged particles such as non-thermal electrons are emitting polarized synchrotron radiation when they are acclerated radially by a magnetic fields, and the characteristic radio emission of radio lobes is synchrotron emission. The signature of polarized emission is written by the Stokes parameters (I, Q, U, V) or the parameters of linear polarization (I^a, I^b, U, V) These parameters are related as $I = I^a + I^b$ and $Q = I^a + I^b$. Here, (a,b) corresponds to the observer's frame, and $\chi_{\rm e}$ is the angle between the magnetic fields direction in plane of the sky and (a). We assume $V = 0$ because the circular polarization in radio lobe is weak in the context of this study. The transport equations in the

observer's frame is (Pacholczyk, 1970)

$$\frac{d}{dl}\begin{pmatrix} I^a \\ I^b \\ U \end{pmatrix} = \begin{pmatrix} A_{11} & 0 & A_{13} \\ 0 & A_{22} & A_{23} \\ 2A_{23} & 2A_{13} & A_{33} \end{pmatrix}\begin{pmatrix} I^a \\ I^b \\ U \end{pmatrix} + \begin{pmatrix} \epsilon^1\cos^2\chi_\mathrm{e} + \epsilon^2\sin^2\chi_\mathrm{e} \\ \epsilon^1\sin^2\chi_\mathrm{e} + \epsilon^2\cos^2\chi_\mathrm{e} \\ -(\epsilon^1-\epsilon^2)\sin 2\chi_\mathrm{e} \end{pmatrix}, \tag{A.9}$$

$$A_{11} = -\kappa^1\cos^4\chi_\mathrm{e} - \frac{1}{2}\kappa\sin^2 2\chi_\mathrm{e} \tag{A.10}$$

$$A_{13} = \frac{1}{4}(\kappa^1-\kappa^2)\sin 2\chi_\mathrm{e} + \frac{d\chi_\mathrm{F}}{dl} \tag{A.11}$$

$$A_{22} = -\kappa^1\sin^4\chi_\mathrm{e} - \frac{1}{2}\kappa\cos^2 2\chi_\mathrm{e} \tag{A.12}$$

$$A_{23} = \frac{1}{4}(\kappa^1-\kappa^2)\sin 2\chi_\mathrm{e} - \frac{d\chi_\mathrm{F}}{dl} \tag{A.13}$$

$$A_{33} = -\kappa, \tag{A.14}$$

where l is the length along the line of sight, $\kappa = 0.5(\kappa^1+\kappa^2)$ is the absorption coefficient, $\epsilon = 0.5(\epsilon^1+\epsilon^2)$ is the emission coefficient, and χ_F is Faraday rotation measure.

Assuming a single power-law distribution for relativistic electrons $N(\gamma)dE = N_0\gamma^{-p}dE$, the emission and absorption coefficients are given by

$$\epsilon^{(1,2)} = \frac{1}{2}c_5(p)N_0(B\sin\theta_\mathrm{B})^{(p+1)/2}\cdot\left(\frac{\nu}{2c_1}\right)^{(1-p)/2}\left[(-1)^{(1,2)+1}\frac{p+1}{p+3/7}+1\right], \tag{A.15}$$

$$\kappa^{(1,2)} = c_6(p)N_0(B\sin\theta_\mathrm{B})^{(p+2)/2}\cdot\left(\frac{\nu}{2c_1}\right)^{-(p+4)/2}\left[(-1)^{(1,2)+1}\frac{p+2}{p+10/3}+1\right], \tag{A.16}$$

where θ_B, ν are the angle between the magnetic field and the line of sight and observing frequency, respectively. Other physical coefficients are

$$c_1 = \frac{3e}{4\pi {m_\mathrm{e}}^3 c^5}, \tag{A.17}$$

$$c_5(p) = \frac{\sqrt{3}}{16\pi}\frac{e^3}{m_\mathrm{e}c^2}\frac{p+7/3}{p+1}\Gamma\left(\frac{p+7}{12}\right)\Gamma\left(\frac{3p+7}{12}\right), \tag{A.18}$$

$$c_6(p) = \frac{\sqrt{3}}{32}e{m_\mathrm{e}}^5c^{10}\left(p+\frac{10}{3}\right)\Gamma\left(\frac{3p+2}{12}\right)\Gamma\left(\frac{3p+10}{12}\right), \tag{A.19}$$

where Γ denotes the Gamma-function. The polarization angle of the magnetic vectors χ_B and the polarization degree p are given by

$$\chi_\mathrm{B} = \frac{1}{2}\arctan\left(\frac{U}{Q}\right)+\frac{\pi}{2}, \quad p = \frac{\sqrt{U^2+Q^2}}{I}. \tag{A.20}$$

A.4 Lobe and Cavity properties

Table A.1 lists radio and X-ray properties of radio galaxies taken from Laura Bîrzan's PhD thesis (Rafferty, 2007) and Rafferty et al. (2006).

Table A.1: Lobe and Cavity Properties

Name	$L_{\rm radio}$	pV	$t_{\rm c}$	a	b	R
	[10^{42} erg s^{-1}]	[10^{58} erg]	[10 Myr]	[kpc]	[kpc]	[kpc]
A133	7.6 ± 1.2	24^{+11}_{-1}	3.8	41	21	32
Perseus	$1.1^{+1.2}_{-0.6}$	$3.7^{+4.7}_{-1.7}$	1.0	9.1	7.3	9.4
		$1.6^{+1.0}_{-0.1}$	0.7	8.2	4.7	6.5
A478	0.02 ± 0.01	$0.74^{+0.57}_{-0.18}$	1.0	5.5	3.4	9.0
		$0.76^{+0.55}_{-0.17}$	1.0	5.6	3.4	9.0
MS 0735.6+7421	130 ± 40	770^{+960}_{-360}	13	110	87	160
		830^{+770}_{-220}	15	130	89	180
Hydra A	29 ± 5	$8.1^{+7}_{-1.6}$	3.0	18	12	29
		$8.6^{+6}_{-0.3}$	3.2	20	12	31
M84	0.0106 ± 0.0012	$0.002^{+0.004}_{-0.0015}$	0.5	1.6	1.6	2.3
		$0.001^{+0.0015}_{-0.0005}$	0.6	2.1	1.2	2.5
M87	0.63 ± 0.05	$0.016^{+0.012}_{-0.003}$	0.4	2.3	1.4	2.8
		$0.004^{+0.001}_{-0.001}$	0.4	1.6	0.8	2.2
Centaurus	0.063 ± 0.013	$0.038^{+0.039}_{-0.012}$	1.0	3.3	2.4	6.0
		$0.022^{+0.012}_{-0.002}$	0.6	3.3	1.6	3.5
A2052	1.80 ± 0.13	$1.2^{+14}_{-0.4}$	1.8	11	7.9	11
		$0.53^{+0.88}_{-0.32}$	1.2	6.5	6.2	6.7
A2199	1.34 ± 0.12	$3.7^{+3.7}_{-1.1}$	2.1	15	10	19
		$3.8^{+2.9}_{-0.4}$	2.3	16	10	21
Cyguns A	710 ± 70	28^{+18}_{-1}	3.4	29	17	43
		56^{+52}_{-13}	3.6	34	23	45

References

Akahori, T., & Yoshikawa, K. 2008, PASJ, 60, L19, doi: 10.1093/pasj/60.4.L19

—. 2010, PASJ, 62, 335, doi: 10.1093/pasj/62.2.335

—. 2012, PASJ, 64, 12, doi: 10.1093/pasj/64.1.12

Appl, S., Lery, T., & Baty, H. 2000, A&A, 355, 818

Asada, K., Kameno, S., Shen, Z. Q., et al. 2009, in Astronomical Society of the Pacific Conference Series, Vol. 402, Approaching Micro-Arcsecond Resolution with VSOP-2: Astrophysics and Technologies, ed. Y. Hagiwara, E. Fomalont, M. Tsuboi, & M. Yasuhiro, 91

Bai, X.-N., Caprioli, D., Sironi, L., & Spitkovsky, A. 2015, ApJ, 809, 55, doi: 10.1088/0004-637X/809/1/55

Balbus, S. A., & Hawley, J. F. 1998, Reviews of Modern Physics, 70, 1, doi: 10.1103/RevModPhys.70.1

Bambic, C. J., & Reynolds, C. S. 2019, ApJ, 886, 78, doi: 10.3847/1538-4357/ab4daf

Beck, R., & Krause, M. 2005, Astronomische Nachrichten, 326, 414, doi: 10.1002/asna.200510366

Begelman, M. C., & Cioffi, D. F. 1989, ApJ, 345, L21, doi: 10.1086/185542

Bell, A. R. 1978, MNRAS, 182, 147, doi: 10.1093/mnras/182.2.147

Belsole, E., Worrall, D. M., Hardcastle, M. J., & Croston, J. H. 2007, MNRAS, 381, 1109, doi: 10.1111/j.1365-2966.2007.12298.x

Bîrzan, L., McNamara, B. R., Nulsen, P. E. J., Carilli, C. L., & Wise, M. W. 2008, ApJ, 686, 859, doi: 10.1086/591416

Bîrzan, L., Rafferty, D. A., McNamara, B. R., Wise, M. W., & Nulsen, P. E. J. 2004, ApJ, 607, 800, doi: 10.1086/383519

Bîrzan, L., Rafferty, D. A., Brüggen, M., et al. 2020, MNRAS, 496, 2613, doi: 10.1093/mnras/staa1594

Blandford, R. D., & Rees, M. J. 1974, MNRAS, 169, 395, doi: 10.1093/mnras/169.3.395

Blandford, R. D., & Znajek, R. L. 1977, MNRAS, 179, 433, doi: 10.1093/mnras/179.3.433

Bodo, G., Massaglia, S., Ferrari, A., & Trussoni, E. 1994, A&A, 283, 655

Bosch-Ramon, V. 2018, A&A, 617, L3, doi: 10.1051/0004-6361/201833952

Bourne, M. A., & Sijacki, D. 2017, MNRAS, 472, 4707, doi: 10.1093/mnras/stx2269

Braginskii, S. I. 1965, Reviews of Plasma Physics, 1, 205

Carilli, C. L., & Barthel, P. D. 1996, A&ARv, 7, 1, doi: 10.1007/s001590050001

Cavagnolo, K. W., McNamara, B. R., Nulsen, P. E. J., et al. 2010, ApJ, 720, 1066, doi: 10.1088/0004-637X/720/2/1066

Celotti, A., & Fabian, A. C. 1993, MNRAS, 264, 228, doi: 10.1093/mnras/264.1.228

Chael, A., Narayan, R., & Johnson, M. D. 2019, MNRAS, 486, 2873, doi: 10.1093/mnras/stz988

Chael, A., Rowan, M., Narayan, R., Johnson, M., & Sironi, L. 2018, MNRAS, 478, 5209, doi: 10.1093/mnras/sty1261

Chandrasekhar, S. 1939, An introduction to the study of stellar structure

Croston, J. H., Hardcastle, M. J., Harris, D. E., et al. 2005, ApJ, 626, 733, doi: 10.1086/430170

Croston, J. H., Hardcastle, M. J., Mingo, B., et al. 2019, A&A, 622, A10, doi: 10.1051/0004-6361/201834019

Crumley, P., Caprioli, D., Markoff, S., & Spitkovsky, A. 2019, MNRAS, 485, 5105, doi: 10.1093/mnras/stz232

Curtis, H. D. 1918, Publications of Lick Observatory, 13, 9

de Gasperin, F., Orrú, E., Murgia, M., et al. 2012, A&A, 547, A56, doi: 10.1051/0004-6361/201220209

De Young, D. S. 2006, ApJ, 648, 200, doi: 10.1086/505861

Dedner, A., Kemm, F., Kröner, D., et al. 2002, Journal of Computational Physics, 175, 645, doi: 10.1006/jcph.2001.6961

Dermer, C. D., Liang, E. P., & Canfield, E. 1991, ApJ, 369, 410, doi: 10.1086/169770

Drappeau, S., Dibi, S., Dexter, J., Markoff, S., & Fragile, P. C. 2013, MNRAS, 431, 2872, doi: 10.1093/mnras/stt388

Eilek, J. A., & Arendt, P. N. 1996, ApJ, 457, 150, doi: 10.1086/176719

English, W., Hardcastle, M. J., & Krause, M. G. H. 2016, MNRAS, 461, 2025, doi: 10.1093/mnras/stw1407

Fabian, A. C. 1994, ARA&A, 32, 277, doi: 10.1146/annurev.aa.32.090194.001425

—. 2012, ARA&A, 50, 455, doi: 10.1146/annurev-astro-081811-125521

Fabian, A. C., Sanders, J. S., Allen, S. W., et al. 2003, MNRAS, 344, L43, doi: 10.1046/j.1365-8711.2003.06902.x

Fanaroff, B. L., & Riley, J. M. 1974, MNRAS, 167, 31P, doi: 10.1093/mnras/167.1.31P

Fujita, Y., Kawakatu, N., & Shlosman, I. 2016, PASJ, 68, 26, doi: 10.1093/pasj/psw012

Gaibler, V., Krause, M., & Camenzind, M. 2009, MNRAS, 400, 1785, doi: 10.1111/j.1365-2966.2009.15625.x

Ghavamian, P., Laming, J. M., & Rakowski, C. E. 2007, ApJ, 654, L69, doi: 10.1086/510740

Ghavamian, P., Schwartz, S. J., Mitchell, J., Masters, A., & Laming, J. M. 2013, Space Sci. Rev., 178, 633, doi: 10.1007/s11214-013-9999-0

Gomez, J. L., Marti, J. M. A., Marscher, A. P., Ibanez, J. M. A., & Marcaide, J. M. 1995, ApJ, 449, L19, doi: 10.1086/309623

Gopal-Krishna, & Wiita, P. J. 2000, A&A, 363, 507. https://arxiv.org/abs/astro-ph/0009441

Gu, L., Kaastra, J., & Raassen, A. J. J. 2016, A&A, 588, A52, doi: 10.1051/0004-6361/201527615

Guo, F. 2015, ApJ, 803, 48, doi: 10.1088/0004-637X/803/1/48

Guo, X., Sironi, L., & Narayan, R. 2018, ApJ, 858, 95, doi: 10.3847/1538-4357/aab6ad

Hardcastle, M. J. 2013, MNRAS, 433, 3364, doi: 10.1093/mnras/stt1024

Hardcastle, M. J., & Croston, J. H. 2010, MNRAS, 404, 2018, doi: 10.1111/j.1365-2966.2010.16420.x

—. 2020, New Astron. Rev., 88, 101539, doi: 10.1016/j.newar.2020.101539

Hardcastle, M. J., Harris, D. E., Worrall, D. M., & Birkinshaw, M. 2004, ApJ, 612, 729, doi: 10.1086/422808

Hardcastle, M. J., & Krause, M. G. H. 2013, MNRAS, 430, 174, doi: 10.1093/mnras/sts564

—. 2014, MNRAS, 443, 1482, doi: 10.1093/mnras/stu1229

Hardcastle, M. J., & Worrall, D. M. 2000, MNRAS, 319, 562, doi: 10.1046/j.1365-8711.2000.03883.x

Harris, D. E., & Grindlay, J. E. 1979, MNRAS, 188, 25, doi: 10.1093/mnras/188.1.25

Harwood, J. J., Hardcastle, M. J., Croston, J. H., & Goodger, J. L. 2013, MNRAS, 435, 3353, doi: 10.1093/mnras/stt1526

Harwood, J. J., Croston, J. H., Intema, H. T., et al. 2016, MNRAS, 458, 4443, doi: 10.1093/mnras/stw638

Hillas, A. M. 1984, ARA&A, 22, 425, doi: 10.1146/annurev.aa.22.090184.002233

Horton, M. A., Krause, M. G. H., & Hardcastle, M. J. 2020, MNRAS, 499, 5765, doi: 10.1093/mnras/staa3020

Hoshino, M. 2018, ApJ, 868, L18, doi: 10.3847/2041-8213/aaef3a

Howes, G. G. 2010, MNRAS, 409, L104, doi: 10.1111/j.1745-3933.2010.00958.x

Ineson, J., Croston, J. H., Hardcastle, M. J., & Mingo, B. 2017, MNRAS, 467, 1586, doi: 10.1093/mnras/stx189

Isobe, N., & Koyama, S. 2015, PASJ, 67, 77, doi: 10.1093/pasj/psv046

Jones, T. W., Ryu, D., & Engel, A. 1999, ApJ, 512, 105, doi: 10.1086/306772

Kawakatu, N., Kino, M., & Takahara, F. 2016, MNRAS, 457, 1124, doi: 10.1093/mnras/stw010

Kawazura, Y., Barnes, M., & Schekochihin, A. A. 2019, Proceedings of the National Academy of Science, 116, 771, doi: 10.1073/pnas.1812491116

Kawazura, Y., Schekochihin, A. A., Barnes, M., et al. 2020, arXiv e-prints, arXiv:2004.04922. https://arxiv.org/abs/2004.04922

Kimball, A. E., & Ivezić, Ž. 2008, AJ, 136, 684, doi: 10.1088/0004-6256/136/2/684

King, I. 1962, AJ, 67, 471, doi: 10.1086/108756

Kino, M., Ito, H., Kawakatu, N., & Nagai, H. 2009, MNRAS, 395, L43, doi: 10.1111/j.1745-3933.2009.00638.x

Kino, M., & Kawakatu, N. 2005, MNRAS, 364, 659, doi: 10.1111/j.1365-2966.2005.09580.x

Kino, M., Kawakatu, N., & Ito, H. 2007, MNRAS, 376, 1630, doi: 10.1111/j.1365-2966.2007.11354.x

Kino, M., Kawakatu, N., & Takahara, F. 2012, ApJ, 751, 101, doi: 10.1088/0004-637X/751/2/101

Koide, S., Shibata, K., Kudoh, T., & Meier, D. L. 2002, Science, 295, 1688, doi: 10.1126/science.1068240

Komarov, S., Reynolds, C., & Churazov, E. 2020, MNRAS, 497, 1434, doi: 10.1093/mnras/staa1986

Komissarov, S. S., Gourgouliatos, K. N., & Matsumoto, J. 2019, MNRAS, 488, 4061, doi: 10.1093/mnras/stz1973

Kormendy, J., & Richstone, D. 1995, ARA&A, 33, 581, doi: 10.1146/annurev.aa.33.090195.003053

Krause, M. 2003, A&A, 398, 113, doi: 10.1051/0004-6361:20021649

Laing, R. A., Guidetti, D., Bridle, A. H., Parma, P., & Bondi, M. 2011, MNRAS, 417, 2789, doi: 10.1111/j.1365-2966.2011.19436.x

Mahatma, V. H., Hardcastle, M. J., Croston, J. H., et al. 2020, MNRAS, 491, 5015, doi: 10.1093/mnras/stz3396

Manmoto, T., Mineshige, S., & Kusunose, M. 1997, ApJ, 489, 791, doi: 10.1086/304817

Markevitch, M. 2006, in ESA Special Publication, Vol. 604, The X-ray Universe 2005, ed. A. Wilson, 723. https://arxiv.org/abs/astro-ph/0511345

Massaglia, S., Bodo, G., Rossi, P., Capetti, S., & Mignone, A. 2016, A&A, 596, A12, doi: 10.1051/0004-6361/201629375

—. 2019, A&A, 621, A132, doi: 10.1051/0004-6361/201834512

Masters, A., Schwartz, S. J., Henley, E. M., et al. 2011, Journal of Geophysical Research (Space Physics), 116, A10107, doi: 10.1029/2011JA016941

Matsukiyo, S. 2010, Physics of Plasmas, 17, 042901, doi: 10.1063/1.3372137

Matsumoto, J., Aloy, M. A., & Perucho, M. 2017, MNRAS, 472, 1421, doi: 10.1093/mnras/stx2012

Matsumoto, J., & Masada, Y. 2013, ApJ, 772, L1, doi: 10.1088/2041-8205/772/1/L1

—. 2019, MNRAS, 490, 4271, doi: 10.1093/mnras/stz2821

Matsumoto, Y., Asahina, Y., Kudoh, Y., et al. 2019, PASJ, 71, 83, doi: 10.1093/pasj/psz064

Matthews, J. H., Bell, A. R., & Blundell, K. M. 2020, New Astron. Rev., 89, 101543, doi: 10.1016/j.newar.2020.101543

McKean, J. P., Godfrey, L. E. H., Vegetti, S., et al. 2016, MNRAS, 463, 3143, doi: 10.1093/mnras/stw2105

McNamara, B. R., & Nulsen, P. E. J. 2007, ARA&A, 45, 117, doi: 10.1146/annurev.astro.45.051806.110625

McNamara, B. R., Wise, M. W., Nulsen, P. E. J., et al. 2001, ApJ, 562, L149, doi: 10.1086/338326

Mendygral, P. J., Jones, T. W., & Dolag, K. 2012, ApJ, 750, 166, doi: 10.1088/0004-637X/750/2/166

Mignone, A., Bodo, G., Vaidya, B., & Mattia, G. 2018, ApJ, 859, 13, doi: 10.3847/1538-4357/aabccd

Mignone, A., & McKinney, J. C. 2007, MNRAS, 378, 1118, doi: 10.1111/j.1365-2966.2007.11849.x

Mignone, A., Striani, E., Tavani, M., & Ferrari, A. 2013, MNRAS, 436, 1102, doi: 10.1093/mnras/stt1632

Mimica, P., Aloy, M. A., Agudo, I., et al. 2009, ApJ, 696, 1142, doi: 10.1088/0004-637X/696/2/1142

Mingo, B., Croston, J. H., Hardcastle, M. J., et al. 2019, MNRAS, 488, 2701, doi: 10.1093/mnras/stz1901

Miyoshi, T., & Kusano, K. 2005, Journal of Computational Physics, 208, 315, doi: 10.1016/j.jcp.2005.02.017

Mizuno, Y., Lyubarsky, Y., Nishikawa, K.-I., & Hardee, P. E. 2009, ApJ, 700, 684, doi: 10.1088/0004-637X/700/1/684

Mizuta, A., Kino, M., & Nagakura, H. 2010, ApJ, 709, L83, doi: 10.1088/2041-8205/709/1/L83

Mizuta, A., Yamada, S., & Takabe, H. 2004, ApJ, 606, 804, doi: 10.1086/382779

Moll, R., Spruit, H. C., & Obergaulinger, M. 2008, A&A, 492, 621, doi: 10.1051/0004-6361:200810523

Mościbrodzka, M., Falcke, H., & Shiokawa, H. 2016, A&A, 586, A38, doi: 10.1051/0004-6361/201526630

Mukherjee, D., Bodo, G., Mignone, A., Rossi, P., & Vaidya, B. 2020, MNRAS, 499, 681, doi: 10.1093/mnras/staa2934

Myers, S. T., & Spangler, S. R. 1985, ApJ, 291, 52, doi: 10.1086/163040

Nakahara, S., Doi, A., Murata, Y., et al. 2019, ApJ, 878, 61, doi: 10.3847/1538-4357/ab1b0e

Nakamura, K. E., Matsumoto, R., Kusunose, M., & Kato, S. 1996, PASJ, 48, 761, doi: 10.1093/pasj/48.5.761

Narayan, R., & Yi, I. 1995, ApJ, 452, 710, doi: 10.1086/176343

Norman, M. L., Winkler, K. H. A., Smarr, L., & Smith, M. D. 1982, A&A, 113, 285

Oda, H., Machida, M., Nakamura, K. E., & Matsumoto, R. 2010, ApJ, 712, 639, doi: 10.1088/0004-637X/712/1/639

Ohmura, T., Machida, M., Nakamura, K., et al. 2019, Galaxies, 7, 14, doi: 10.3390/galaxies7010014

Omma, H., Binney, J., Bryan, G., & Slyz, A. 2004, MNRAS, 348, 1105, doi: 10.1111/j.1365-2966.2004.07382.x

Pacholczyk, A. G. 1970, Radio astrophysics. Nonthermal processes in galactic and extragalactic sources

Perucho, M. 2020, MNRAS, 494, L22, doi: 10.1093/mnrasl/slaa031

Perucho, M., Martí, J. M., & Hanasz, M. 2005, A&A, 443, 863, doi: 10.1051/0004-6361:20053115

Perucho, M., Martí, J.-M., & Quilis, V. 2019, MNRAS, 482, 3718, doi: 10.1093/mnras/sty2912

Pfrommer, C., Pakmor, R., Schaal, K., Simpson, C. M., & Springel, V. 2017, MNRAS, 465, 4500, doi: 10.1093/mnras/stw2941

Porth, O., & Komissarov, S. S. 2015, MNRAS, 452, 1089, doi: 10.1093/mnras/stv1295

Rafferty, D. A., McNamara, B. R., Nulsen, P. E. J., & Wise, M. W. 2006, ApJ, 652, 216, doi: 10.1086/507672

Rafferty, F. 2007, PhD thesis, Ohio University

Ressler, S. M., Tchekhovskoy, A., Quataert, E., Chand ra, M., & Gammie, C. F. 2015, MNRAS, 454, 1848, doi: 10.1093/mnras/stv2084

Reynolds, C. S., Heinz, S., & Begelman, M. C. 2001, ApJ, 549, L179, doi: 10.1086/319159

Rossi, P., Bodo, G., Massaglia, S., & Capetti, A. 2020, A&A, 642, A69, doi: 10.1051/0004-6361/202038725

Rowan, M. E., Sironi, L., & Narayan, R. 2017, ApJ, 850, 29, doi: 10.3847/1538-4357/aa9380

—. 2019, ApJ, 873, 2, doi: 10.3847/1538-4357/ab03d7

Russell, H. R., McNamara, B. R., Sanders, J. S., et al. 2012, MNRAS, 423, 236, doi: 10.1111/j.1365-2966.2012.20808.x

Ryan, B. R., Ressler, S. M., Dolence, J. C., Gammie, C., & Quataert, E. 2018, ApJ, 864, 126, doi: 10.3847/1538-4357/aad73a

Rybicki, G. B., & Lightman, A. P. 1986, Radiative Processes in Astrophysics, 400

Ryu, D., Kang, H., Hallman, E., & Jones, T. W. 2003, ApJ, 593, 599, doi: 10.1086/376723

Sadowski, A., Wielgus, M., Narayan, R., et al. 2017, MNRAS, 466, 705, doi: 10.1093/mnras/stw3116

Schaal, K., & Springel, V. 2015, MNRAS, 446, 3992, doi: 10.1093/mnras/stu2386

Scheuer, P. A. G. 1974, MNRAS, 166, 513, doi: 10.1093/mnras/166.3.513

Schwartz, S. J., Thomsen, M. F., Bame, S. J., & Stansberry, J. 1988, J. Geophys. Res., 93, 12923, doi: 10.1029/JA093iA11p12923

Schwartz, S. J., Thomsen, M. F., Bame, S. J., & Stansberry, J. 1988, Journal of Geophysical Research: Space Physics, 93, 12923, doi: 10.1029/JA093iA11p12923

Seta, H., Tashiro, M. S., & Inoue, S. 2013, PASJ, 65, 106, doi: 10.1093/pasj/65.5.106

Shapiro, S. L., Lightman, A. P., & Eardley, D. M. 1976, ApJ, 204, 187, doi: 10.1086/154162

Sharma, P., Quataert, E., Hammett, G. W., & Stone, J. M. 2007, ApJ, 667, 714, doi: 10.1086/520800

Shibata, K., & Uchida, Y. 1986, PASJ, 38, 631

Shimwell, T. W., Röttgering, H. J. A., Best, P. N., et al. 2017, A&A, 598, A104, doi: 10.1051/0004-6361/201629313

Sironi, L., & Spitkovsky, A. 2011, ApJ, 726, 75, doi: 10.1088/0004-637X/726/2/75

Snios, B., Nulsen, P. E. J., Wise, M. W., et al. 2018, ApJ, 855, 71, doi: 10.3847/1538-4357/aaaf1a

Spitzer, L. 1962, Physics of Fully Ionized Gases

Stawarz, Ł., Tanaka, Y. T., Madejski, G., et al. 2013, ApJ, 766, 48, doi: 10.1088/0004-637X/766/1/48

Stepney, S., & Guilbert, P. W. 1983, MNRAS, 204, 1269, doi: 10.1093/mnras/204.4.1269

Suresh, A., & Huynh, H. T. 1997, Journal of Computational Physics, 136, 83, doi: 10.1006/jcph.1997.5745

Suzuki, K., Ogawa, T., Matsumoto, Y., & Matsumoto, R. 2013, ApJ, 768, 175, doi: 10.1088/0004-637X/768/2/175

Svensson, R. 1982, ApJ, 258, 335, doi: 10.1086/160082

Takizawa, M. 1998, ApJ, 509, 579, doi: 10.1086/306530

—. 1999, ApJ, 520, 514, doi: 10.1086/307497

Tchekhovskoy, A., & Bromberg, O. 2016, MNRAS, 461, L46, doi: 10.1093/mnrasl/slw064

Toma, K., Komissarov, S. S., & Porth, O. 2017, MNRAS, 472, 1253, doi: 10.1093/mnras/stx1770

Tran, A., & Sironi, L. 2020, ApJ, 900, L36, doi: 10.3847/2041-8213/abb19c

Uchiyama, Y., Urry, C. M., Cheung, C. C., et al. 2006, ApJ, 648, 910, doi: 10.1086/505964

Vaidya, B., Mignone, A., Bodo, G., Rossi, P., & Massaglia, S. 2018, ApJ, 865, 144, doi: 10.3847/1538-4357/aadd17

van Adelsberg, M., Heng, K., McCray, R., & Raymond, J. C. 2008, ApJ, 689, 1089, doi: 10.1086/592680

Vink, J., Broersen, S., Bykov, A., & Gabici, S. 2015, A&A, 579, A13, doi: 10.1051/0004-6361/201424612

Wilson, A. S., Smith, D. A., & Young, A. J. 2006, ApJ, 644, L9, doi: 10.1086/504108

Winner, G., Pfrommer, C., Girichidis, P., & Pakmor, R. 2019, MNRAS, 488, 2235, doi: 10.1093/mnras/stz1792

Yoshida, N., Furlanetto, S. R., & Hernquist, L. 2005, ApJ, 618, L91, doi: 10.1086/427874

Zhang, H., Li, H., Guo, F., & Taylor, G. 2017, ApJ, 835, 125, doi: 10.3847/1538-4357/835/2/125

Zhdankin, V., Uzdensky, D. A., & Kunz, M. W. 2020, arXiv e-prints, arXiv:2007.12050. https://arxiv.org/abs/2007.12050

Zhdankin, V., Uzdensky, D. A., Werner, G. R., & Begelman, M. C. 2019, Phys. Rev. Lett., 122, 055101, doi: 10.1103/PhysRevLett.122.055101